UNIVERSITY OF CALIFORNIA SAN DIEGO

Cellular Adhesion Strength as a Potential Biophysical Marker of Metastatic Behavior

A dissertation submitted in partial satisfaction of the requirements for the degree
Doctor of Philosophy

in

Bioengineering

by

Pranjali Beri

Committee in charge:

Professor Adam Engler, Chair
Professor Stephanie Fraley
Professor Christian Metallo
Professor Anne Wallace
Professor Jing Yang

2020

The Dissertation of Pranjali Beri is approved, and it is acceptable in quality and form for publication on microfilm and electronically:

_____

_____

_____

_____

_____
Chair

University of California San Diego

2020

DEDICATION

To my parents, who have always supported my endeavors.

TABLE OF CONTENTS

Signature Page iii

Dedication iv

Table of Contents v

List of Figures and Tables x

Acknowledgements xii

Vita xiv

Abstract of the Dissertation xv

Chapter 1. Utilizing cell-ECM dynamics to model and measure epithelial cancers 1

1.1 Abstract 1

1.2 Introduction 1

1.3 Engineering the tumor microenvironment 4

1.3.1 Modulating matrix stiffness 4

1.3.2 Fiber architecture, topography, and porosity 6

1.3.3 Model requirements beyond materials 7

1.4 Capturing cells in blood and stroma 9

1.4.1 Ex vivo detection using nano-topographies 10

1.4.2 In vivo cell detection using implantable materials 12

1.4.3 Ex vivo cell detection using physical properties 14

1.4.4 Non-invasive surveillance of tumor-adjacent stroma 17

1.5 Perspectives and conclusion 18

1.6 Acknowledgements 20

Chapter 2. Metastatic state of cancer cells may be indicated by adhesion strength 22

2.1 Abstract 22

2.2 Introduction 23

2.3 Results 25

2.3.1 Mg^{2+} and Ca^{2+} concentrations influence the adhesion heterogeneity of metastatic cells 25

2.3.2 Adhesion heterogeneity correlates with a migratory phenotype 29

2.3.3 Labile FAs reduce adhesion strength and enhance migration in metastatic cells. 33

2.4 Discussion 34

2.5 Conclusions 38

2.6 Methods 38

2.6.1 Cell culture 38

2.6.2 Cell adhesion-strength assay 38

2.6.3 Quantification of adhesion strength 39

2.6.4 Migration assays 40

2.6.5 Immunofluorescence staining and focal adhesion analysis 41

2.6.6 Western blotting 42

2.6.7 Fluorescence-activated cell sorting analysis 42

2.6.8 Statistical analysis 43

2.7 Supplementary Figures 44

2.8 Acknowledgements 49

Chapter 3. Cell adhesiveness serves as a biophysical marker for metastatic potential 50

3.1 Abstract 50

3.2 Introduction 51

3.3 Results 53

3.3.1 Strongly and weakly adherent phenotypes are maintained post sort. 54

3.3.2 Parallel plate flow chamber can distinguish between weakly adherent and strongly adherent cell lines. 56

3.3.3 Weakly adherent cells display greater migratory propensity than strongly adherent cells. 58

3.3.4 Weakly adherent cells have more labile focal adhesions and are more contractile. 60

3.3.5 Intrinsic transcriptional variation in microtubule proteins contributes to increased migration of weakly adherent cells. 62

3.4 Discussion 64

3.5 Methods 67

3.5.1 Cell Culture 67

3.5.2 Parallel plate shear assay 68

3.5.3 Isolating weakly (WA) and strongly (SA) adherent cells 68

3.5.4 Co-culture assay 69

3.5.5 Measuring percent detachment versus metastatic capability 69

3.5.6 Immunofluorescence staining and focal adhesion (FA) analysis 70

3.5.7 Traction Force Microscopy (TFM) 70

3.5.8 Western blotting 71

3.5.9 2D migration assays on collagen gels 72

3.5.10 2D migration assays on polyacrylamide gels of varying stiffness 72

3.5.11 Preparing spheroids of MDA-MB231 cells 73

3.5.12 3D migration assay in collagen gels 73

3.5.13 RNA Sequencing 74

3.5.14 Quantitative PCR 74

3.5.15 TCGA Dataset Analysis 75

3.5.16 Statistics 76

3.5.17 Data availability 76

3.6 Supplementary Figures 77

3.7 Acknowledgements 87

Chapter 4. An *in vivo* demonstration of adhesion strength as a predictive marker of metastatic potential 88

4.1 Abstract 88

4.2 Introduction 88

4.3 Results 90

4.3.1 MDA-MB 231 cellular adhesion strength and migratory differences were maintained post-viral transduction 90

4.3.2 Invaded cells have decreased adhesion strength compared to cells in the tumor bolus 90

4.4 Future Directions 92

4.5 Methods 93

4.5.1 Cell Culture 93

4.5.2 Creating GFP and Luciferase-Expressing MDA-MB 231 cells and validating adhesion heterogeneity 93

4.5.3 Isolation of MDA-MB 231 cells in tumor and surrounding stroma 94

4.5.4 Quantification of cellular adhesion strength 95

4.6 Acknowledgements 95

4.7 Supplementary Figures 96

Chapter 5. Conclusions 98

5.1 Introduction 98

5.2 Metastatic cancer cell populations display decreased adhesion strength and more labile focal adhesions compared to non-metastatic counterparts 98

5.3 Weakly adherent cells within a heterogeneous population represent the most migratory and aggressive fraction 100

5.4 Locally invaded cancer cells demonstrate decreased adhesion compare to cells within the tumor 101

5.5 Future directions 102

References 104

LIST OF FIGURES AND TABLES

Figure 1.1. Cancer and Metastasis. 3

Figure 1.2. Modelling the tumor microenvironment. 5

Figure 1.3 Next-generation material-based cancer technologies. 11

Figure 2.1. Adhesion strength is heterogeneous for metastatic mammary epithelial cells in a stromal-like niche. 27

Figure 2.2. Adhesion strength can be titrated but is independent of the matrix ligand type. 29

Figure 2.3. The weakly adherent subpopulation of MDAMB231 cells is highly migratory. 31

Figure 2.4. FAs are more Mg^{2+} and Ca^{2+} sensitive in MDAMB231 cells than in MCF10A cells. 32

Figure 2.5. Integrin blocking reduces cation-dependent adhesion strength in nonmalignant cells. 34

Supplementary Figure 2.1. Spinning Disc Assay Creates a Radially-dependent Shear Profile. 44

Supplementary Figure 2.2. Cell Morphology and Distribution are Independent of Mammary Epithelial Cell Line. 45

Supplementary Figure 2.3. MCF10A Cells Exhibit Cation-Sensitive Change in Attachment Strength. 46

Supplementary Figure 2.4. Attachment Strength is Heterogeneous for Additional Mammary Epithelial Cells and Prostate Cancer Cells in Stromal-like Niche. 47

Supplementary Figure 2.5. Migration for SUM1315 and PC-3. 48

Supplementary Table 2.6. Media formulations for the indicated cell lines. 48

Figure 3.1. Low Cation PPFC Accurately and Precisely Sorts Cancer Cell Populations that are Stable Long-term. 53

Figure 3.2. Sorted Populations of Single cells and Spheroids Exhibit and Sustain Different Migration Patterns. 55

Figure 3.3. Adherent Phenotypes within a Cancer Line Result from Intrinsic Adhesion Stability and Contractility Differences. 57

Figure 3.4. RNA-seq Identifies Intrinsic Patterns that Indicate Structural rather than Expression Changes in Adhesion. 61

Figure 3.5. Expression of microtubule-associated genes resembling weakly adherent fraction predicts poor outcome in breast cancer patients. 64

Supplementary Figure 3.1. PPFC Assembly and Use. 77

Supplementary Figure 3.2. Rose Plots of Post-Sort Cells. 78

Supplementary Figure 3.3. Migratory Differences in Isogenic MCF10A and MCF10AT Cells. 79

Supplementary Figure 3.4. Sorted Populations of MDA-MB231 Cells Display Migratory Differences Under Different Substrate Stiffnesses. 80

Supplementary Figure 3.5. Determining Spheroid Invasive Front 81

Supplementary Figure 3.6. Other Epithelial Cells Populations Exhibit Migration Differences Post-Sort. 82

Supplementary Figure 3.7. Focal Adhesion Disassembly in Stromal Cation Conditions. 83

Supplementary Figure 3.8. Proliferation of Post-Sort Cells is not Different. 84

Supplementary Table 3.9. qPCR Primers. 85

Supplementary Table 3.10. Genes linked to highlighted GO terms that were used for TCGA analysis. 86

Figure 4.1. MDA-MB231 cells that have invaded into the stroma display decreased adhesion strength compared to cells in the stiff tumor. 91

Supplementary Figure 4.1. GFP-Luciferase lentiviral transduction does not alter inherent heterogeneity of MDA-MB231 cells 96

Supplementary Figure 4.2. Tumor growth was monitored using IVIS and GFP+ cells can be sorted from tumor and stroma. 97

ACKNOWLEDGEMENTS

I would like to thank Professor Adam Engler for providing me with the opportunity to pursue my scientific interests. I am extremely grateful for the guidance and support you have given me throughout my time in your lab. I would also like to thank the rest of my committee—Professors Stephanie Fraley, Christian Metallo, Anne Wallace, and Jing Yang—for their guidance through this process. In addition, I would like to thank the National Science Foundation Graduate Research Fellowship Program as this work would not be possible without it.

I would like to thank the members of the Engler lab for making my graduate school experience truly memorable and exciting and for providing me with valuable input throughout this process. In particular, I am thankful for Aditya Kumar for always being there when I needed to brainstorm and for always reassuring me of my own abilities. Lastly, I am incredibly grateful to all of my undergraduate students who have contributed so significantly to the work I have done here: Anna Popravko, Alyssa Chiang, Enio Hodzic, and Sarah Klein. Thank you so much for putting your faith in me and for always coming to lab with enthusiasm and strong work ethic. I have no doubt that you will all go on to do great things in the future, and I hope you will always remain in touch.

Lastly, I would like to thank my family and friends for supporting me throughout my time in graduate school. I especially want to thank my Mom and Dad; without them, I would not have been able to accomplish everything I have. Your sacrifices and support have been the driving force behind everything I have done and will strive to do. I hope you know how much every phone call has meant to me, and I feel stronger knowing I always have the two of you behind me.

Chapter 1, in full, is a modification of the material as it appears in Beri, P., Matte, B.F, Fattet, L., Kim, D., Yang, J., and Engler, A.J. "Biomaterials to model and measure epithelial cancers" *Nature Rev Materials*, 2018. 3, 418-430. The dissertation author was the primary author of this paper.

Chapter 2, in full, is a reprint of the material as it appears in Fuhrmann, A., Banisadr, A., Beri, P., Tlsty, T.D., and Engler, A.J. "Metastatic State of Cancer Cells may be indicated by Adhesion Strength." *Biophys J*, 2017. 112(4): 736-745. The dissertation author was a corresponding author of this paper.

Chapter 3, in full, is a reprint of the material as it appears in Beri, P., Popravko, A., Yeoman, B., Kumar, A., Chen, K., Hodzic, E., Chiang, A., Banisadr, A., Placone, J.K., Carter, H., Fraley, S., Katira, P., and Engler, A.J. "Cell adhesiveness serves as a biophysical marker for metastatic potential" *Cancer Research*, 2020. 80(4): 901-911. The dissertation author was the primary author of this paper.

Chapter 4 contains unpublished material from the ongoing project Beri, P., Tuler, J., and Engler, A.J. Chapter 4, "An in vivo demonstration of adhesion strength as a predictive marker of metastatic potential." The dissertation author will be the primary author on any resulting publication.

VITA

2015 Bachelor of Science, University of California Berkeley

2020 Doctor of Philosophy, University of California San Diego

PUBLICATIONS

Mayner, J., Kumar, A., **Beri, P.**, Lo Sardo, V., Torkamani, A., Baldwin, K., Engler, A.J., "Vascular Smooth Muscle Cell Phenotype is Regulated by Heterogeneous Expression of lncRNA." *In preparation for submission*.

Yeoman, B., Shatkin, G., **Beri, P.**, Engler, A.J., Katira, P. "Cell Mechanotype Dictates Rigidity-Sensing and Enables Metastatic Cells to Become Adurotactic." *In preparation for submission.*

Banisadr, A., Eick, M., **Beri, P.**, Parisian, A. D., Yeoman, B., Placone, J., Engler, A.J., Furnari, F. "EGFRvIII contributes to glioblastoma migration by cell intrinsic and cooperative mechanisms that reduce cell-matrix adhesion." *In preparation for submission.*

Beri, P., Popravko, A., Yeoman, B., Kumar, A., Chen, K., Hodzic, E., Chiang, A., Banisadr, A., Placone, J.K., Carter, H., Fraley, S., Katira, P., and Engler, A.J. "Cell adhesiveness serves as a biophysical marker for metastatic potential" *Cancer Research*, 80(4), 901-911.

Beri, P., Matte, B. F., Fattet, L., Kim, D., Yang, J., & Engler, A. J. (2018). "Biomaterials to model and measure epithelial cancers." *Nature Reviews Materials*, 3, 418-430.

Fuhrmann, A., Banisadr, A., **Beri, P.**, Tlsty, T. D., & Engler, A. J. (2017). "Metastatic State of Cancer Cells May Be Indicated by Adhesion Strength." *Biophysical Journal*, 112(4), 736-745.

ABSTRACT OF THE DISSERTATION

Cellular Adhesion Strength as a Potential Biophysical Marker of Metastatic Behavior

by

Pranjali Beri

Doctor of Philosophy in Bioengineering

University of California San Diego, 2020

Professor Adam J. Engler, Chair

While metastasis of cells from the primary tumor is what leads to mortality in cancer patients, the likelihood of metastasis varies from patient-to-patient as well as for cells within a given tumor. However, there is no universal biological marker that can identify heterogeneity in aggressiveness. Cell-ECM dynamics play a profound role in the dissemination of tumor cells from the primary tumor and variations in cell-ECM dynamics in cancer cells can be exploited to distinguish more aggressive cancers from their non-aggressive counterparts. This dissertation aims to demonstrate the utility of studying cell-

ECM dynamics—specifically cellular adhesion to the ECM—in order to identify the most aggressive cancer cells.

We first examined how adhesion strength of metastatic and non-metastatic cancer cells varies in the presence of tumoral and stromal cation conditions. We built a spinning-disk shear assay to quantify population adhesion strength in the presence or absence of Mg^{2+} and Ca^{2+}. Metastatic cells displayed a decrease in cellular adhesion strength in low Mg^{2+} and Ca^{2+} conditions as well as heterogeneity in adhesion strength that was not present in the non-metastatic cells. These differences were correlated with differing rates of focal adhesion disassembly between metastatic and non-metastatic cells. When non-metastatic cells were exposed to RGD to decrease their adhesion, they recapitulated the decreased adhesion, increased focal adhesion disassembly, and increased migration associated with metastatic cells. These data suggest that decreased cellular adhesion is a marker of metastatic cell populations.

We next examined how heterogeneity in adhesion strength within a population could lead to intrapopulation heterogeneity in metastatic ability. We utilized a parallel plate flow chamber to isolate distinct fractions of cells from a heterogeneous population. Weakly adherent cells within a population displayed increased 2D and 3D migration compared to their strongly adherent counterparts. These differences were due to increased focal adhesion disassembly and contractility in the weakly adherent cells, which is consistent with previous findings comparing metastatic and non-metastatic cell lines. RNA sequencing revealed differences in transcriptomic expression of cytoskeletal proteins, particularly those corresponding to the microtubule network, between the weakly and strongly adherent cells. When we compared triple negative patient datasets to the

expression profiles of weakly and strongly adherent cells, we found that patients with gene expression profiles that matched weakly adherent cells had significantly lower disease-free intervals than the patients that matched strongly-adherent cells.

Finally, we examined how adhesion strength can correlate with invasive and metastatic potential *in vivo*. We injected MDA-MB231 cells into the mammary fat pads of NOD/SCIDγ mice, allowed the tumors to grow until localized invasion occurred, resected the fat pad and manually separated the tumor from stroma, and isolated the cancer cells from tumor and stroma respectively. We observed that cells that had invaded into the stroma had a decreased adhesion strength compared to cells within the tumor. This further suggests that the least adherent cells are the most invasive and have the greatest metastatic potential.

These studies demonstrate the universality of using cellular adhesion strength as a biophysical marker of metastatic potential. In addition, the shear separation technique can be used to study heterogeneous cell fractions in other diseases where adhesion plays a significant role.

Chapter 1.

Utilizing cell-ECM dynamics to model and measure epithelial cancers

1.1 Abstract

The use of biomaterials has substantially contributed to both our understanding of tumorigenesis and our ability to identify and capture tumor cells in vitro and in vivo. Engineered biomaterials can mimic the spatial and temporal properties of the surrounding tumor niche to investigate the specific effects of the environment on disease progression, offering an alternative to animal models for the testing of cancer cell behavior. Biomaterials can also be used to capture and detect cancer cells in vitro and in vivo to monitor tumor progression. Here we examine how biomaterials can be applied to capture circulating tumor cells in blood samples for the early detection of metastasis. We highlight biomaterial-based strategies to investigate local regions adjacent to the tumor and survey potential applications of biomaterial-based devices for diagnosis and prognosis, such as the detection of cellular deformability and the non-invasive surveillance of tumor-adjacent stroma.

1.2 Introduction

Tumors are complex and heterogeneous structures. Understanding tumor progression and cancer metastasis requires the investigation of not only the tumor itself but

also of the dynamic and reciprocal interactions between cancer cells and the adjacent tumor stroma, that is, the tumor microenvironment (or niche). This microenvironment is very heterogeneous but generally contains certain cell types (for example, cancer-associated fibroblasts (CAFs)), extracellular matrix (ECM) proteins and signaling molecules, which change as tumors grow and metastasize throughout the body (Figure 1.1). The tumor microenvironment proper ties are modulated, in part, as a result of alterations to the 3D fibrillar ECM that surrounds tumor tissue and to the 2D basement membrane that underlies epithelia. For example, the ECM can be modified by CAFs[1, 2] and tumor cells alike, causing the matrix to become stiffer(*3*), more dense(*4*), crosslinked(*5*), aligned (*3*), and less porous (*5*). In the case of larger breast tumors, patients can actually feel the stiffened tumor stroma.

Animal models are powerful systems to study the dynamic stromal properties of tumors, but it is difficult to dissect the specific contributions of individual microenvironmental cues to tumor development and progression(*6*). However, reducing the in vivo niche to its major biochemical and biophysical components offers a possibility to model the tumor microenvironment in vitro. Identifying and recreating specific aspects of the tumor stroma, for example, stiffness, topography or nutrient exchange, using biomaterials allows for the fabrication of reductionist in vitro systems to study basic mechanisms that regulate cancer cell plasticity, dissemination and repopulation of the niche.

Biomaterials have been used to study tumor biology since the early 1980s, when scientists questioned whether signals from the extracellular compartment could regulate cell behavior in a distinct and/or similar way as to how genetics can dictate cell fate. In

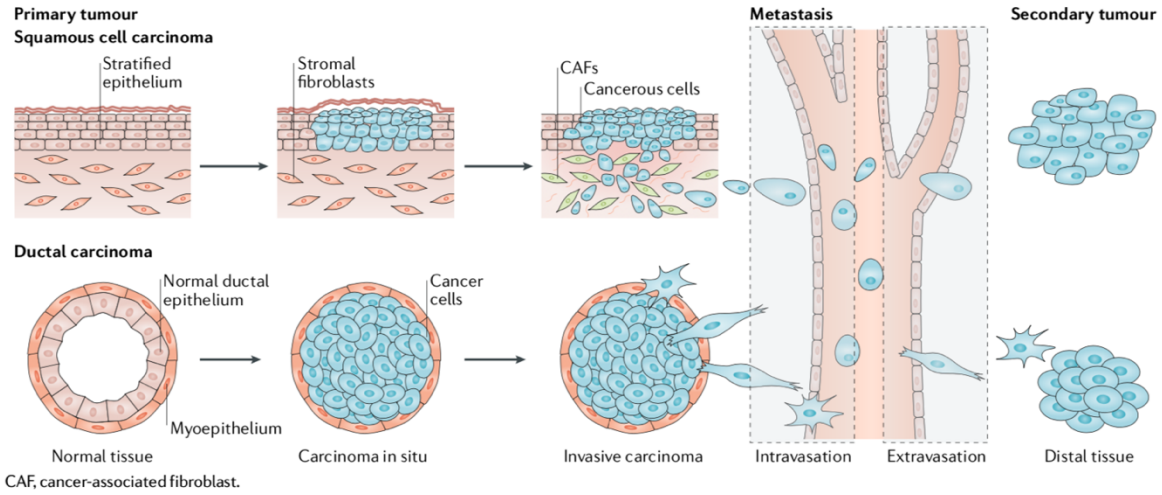

Figure 1.1. Cancer and Metastasis.

Squamous and ductal carcinoma share basic stages of cancer metastasis. These cancers originate from epithelial cells, which line surfaces and vessels of the body.

particular, seminal work demonstrating that changes to the extracellular milieu could affect gene expression in mammary glands(*7*) has triggered unprecedented interest in how the ECM regulates cell behavior in development. Pioneering work by the group of Mina Bissell established a 'dynamic reciprocity' between the cell and its microenvironment, showing that components of the ECM, such as collagen or fibronectin, associate with the plasma membrane and connect to the intracellular cytoskeleton through specific structures (later identified as focal adhesions). Signals from the ECM are then relayed to the nucleus to affect gene expression and to regulate the expression of ECM molecules or their modification through the expression of ECM-modifying enzymes. However, the detailed mechanisms of cell–ECM interactions are still under intense investigation, and much remains to be understood.

In this chapter, we discuss how biomaterials can be applied to model tumors and their microenvironments in vitro. We examine different materials that can be used to capture and measure cancer cells for diagnostics and prognostics and investigate biomaterials for their potential to be used for cancer treatment in vivo.

1.3 Engineering the tumor microenvironment

1.3.1 Modulating matrix stiffness

A breast tumor mass is routinely identified by manual palpation; the patient or doctor identifies a stiff lump relative to the compliant surrounding tissue. In epithelial tumors, a direct correlation between stiffness and metastatic potential has been reported(*3, 5, 8-11*); however, this correlation has not been observed in all animal models(*12*). To tune stiff ness in natural ECMs, matrix concentration is increased, which also affects porosity and ligand density(*3*). By contrast, in synthetic materials, changing crosslink density or bulk polymer concentration allows for the variation of stiffness by several orders of magnitude without modifying adhesion ligand density(*13*) (Figure 1.2B). Most epithelial tumor models use a combination of naturally derived or natural and synthetic matrices in 3D(*14, 15*). These approaches using materials with increasing stiffness have been applied to study the mechano-sensitivity of mammary epithelia during their transition to a mesenchymal phenotype, that is, the epithelial-to-mesenchymal transition (EMT). A stiff matrix triggers focal adhesion assembly through stress-induced elastic deformation, which in combination with cell contractility activates extracellular signal-regulated kinase (ERK) and the RHO family of GTPases, driving MECs towards EMT(*3*). Increasing matrix stiffness also triggers the release of the EMT transcription factor Twist family bHLH transcription factor 1 (TWIST1) from its cytoplasmic binding partner RAS GTPase-activating protein-binding protein 2 (G3BP2), its translocation to the nucleus and initiation of an EMT transcription program(*11*). Additional evidence suggests that hydrogel stiffness regulates not only malignant transformation but also dissemination and

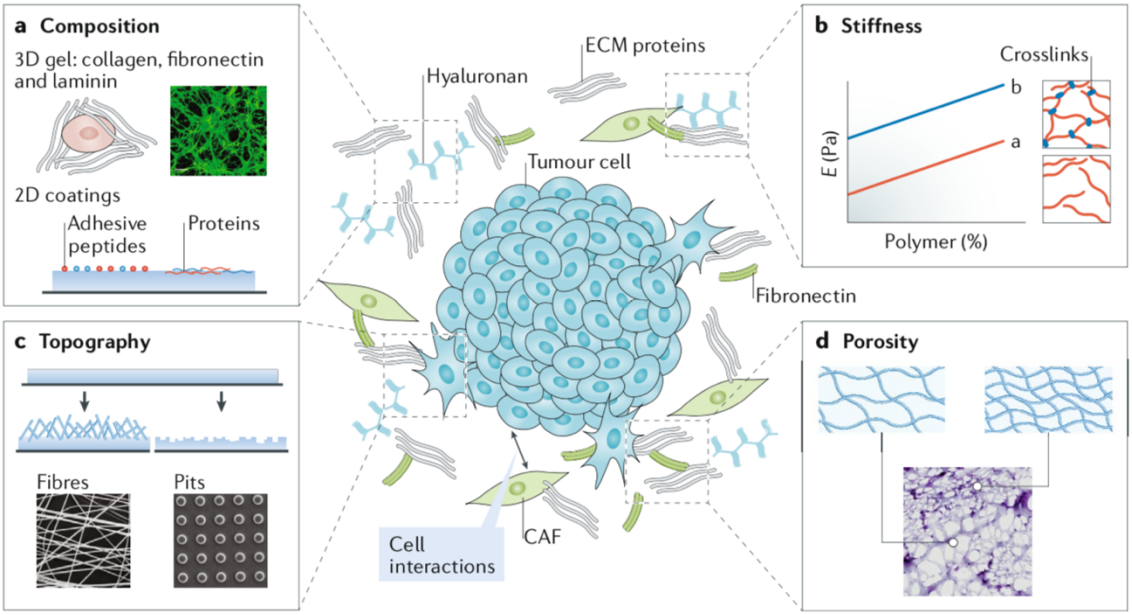

Figure 1.2. Modelling the tumor microenvironment.

The tumor microenvironment constitutes the niche that surrounds a tumor, including extracellular matrix (ECM), cells and signaling molecules. The niche is characterized by specific dynamic ECM properties. **a |** The composition of the ECM can vary in terms of both ligand type and ligand presentation. 3D hydrogels made of ECM proteins or 2D materials can be used to recreate a specific ECM composition. The ligand type(*16*) and concentration(*3*) affect cell behavior and can induce an epithelial-to-mesenchymal transition (EMT). **b |** Stiffness, that is, the Young's modulus, can also impact EMT(*3, 11*). The Young's modulus (*E*) of a material can be modified by changing chain entanglements (line a) or crosslinking (line b). The stiffness is measured as the force per cross-sectional area of the material. **c |** Topographical features of the niche can be recreated by spinning polymers into fibers and depositing them as a thin layer on a surface, to which a cell can adhere. Alternatively, a material can be etched to create specific nano-topographical or micro-topographical features, such as pits. Such topographies can be used to induce cell transformations(*17-21*) or to capture cancer cells(*22-24*) **d |** The pore size and pore connectivity of the tumor microenvironment can be modelled by modulating bulk polymer density or droplet size in emulsions. Non-malignant cells are highly sensitive to pore size(*25, 26*); materials with small pores can inhibit migration and proliferation, and large pores are felt by the cells as 2D surfaces. CAF, cancer-associated fibroblast.

migration of invading cancer cells(*27*). Metastatic cells have tumor-specific stiffness preferences; at an optimal stiffness, corresponding to the stiffness of a specific tumor type, they express markers consistent with highly migratory cells and migrate faster than at sub-optimal stiffness(*28*).

Synthetic materials can also be designed as dynamic systems, in which crosslinking can be gradually(*29, 30*) changed or modified on demand(*10, 31, 32*), thus better mimicking slow disease progression. Collective cancer cell behaviors can be substantially

different in materials that stiffen following polarization than in materials with static stiffness(*33*). Controlled degradation(*34*) can also provide a strategy to examine cell behavior in response to an environment that becomes increasingly softer and to identify mechano-transduction pathways that can slow tumorigenesis. Therefore, matrix stiffness and the timing of its presentation are important ECM properties that influence neoplastic cell behavior.

1.3.2 Fiber architecture, topography, and porosity

The architecture and topography of ECM fibers also affect the behavior of neoplastic cells. Cancer cells can sense whether the surface is atomically flat or has a roughened topography (Figure 1.2C), which can induce invasion and metastasis. For example, fibrillar matrix structures can be synthetically recreated using electro-spun fibers, such as silk, to support 3D cell migration of both malignant and nonmalignant cell lines(*17, 18*).

Alternatively, polydimethylsiloxane (PDMS) is a commonly used polymer for topographical studies. Using patterned PDMS substrates, it has been shown that neoplastic cells are less sensitive to geometrical cues than nonmalignant cells(*19, 20*). On micro-grafted surfaces, MECs enter a dormant state, whereas their neoplastic counterparts continue to proliferate through a RHO–RHO-associated protein kinase (ROCK)–myosin--dependent pathway(*21*). This principle also extends to other roughened surfaces, on which malignant cells appear less sensitive and continue to grow and migrate independent of roughness(*19, 21*).

Similarly, ECM porosity, which dictates cell spreading, can differentially affect nonmalignant and meta static cells (Figure 1.2D). For example, metastatic cells can migrate

through PDMS channels that are smaller than the diameter of their nuclei by breaking and reforming their nuclear envelope(*35*). 3D material systems containing collagen and agarose can be used to independently modulate stiffness, porosity and ligand density. If the porosity of the material is decreased independent of other properties, glioblastoma cell migration is sterically hindered(*25*). Conversely, nonmalignant cells sense porosity together with other properties, such as stiffness; for example, in channels of decreasing width, the migration speed of nonmalignant cells increases with stiffer channel walls(*26*). These data suggest complex and often coupled interactions and therefore do not yet allow an overarching conclusion or propose the ideal material for modelling the tumor microenvironment. However, individual ECM properties have already been identified that can be modulated using biomaterials to study their effects on cancer cells.

1.3.3 Model requirements beyond materials

Tumors are often described as organs that contain different cell types, including CAFs(*36*), endothelial cells, pericytes and immune inflammatory cells(*37*). The vast majority of biomaterial-based models are incomplete because they do not incorporate these important cell types that modify the microenvironment. Cancer cells secrete soluble factors that activate CAFs, leading to a change in CAF protein expression and an increase in MMP secretion and CAF contractility(*38-40*). CAF generated forces promote angiogenesis(*41*) and generate holes in the matrix to facilitate cell invasion(*40*). CAFs can also directly bind to cancer cells through heterotypic epithelial cadherin (E-cadherin; also known as CDH1) and neural cadherin (N-cadherin; also known as CDH2) junctions and pull cancer cells away from the tumor(*42*). CAF contractility further promotes the nuclear trans location of Yes-associated protein YAP65 homologue (YAP1), which in turn results in matrix

stiffening, angiogenesis and cancer cell invasion. This positive feed back loop drives tumor progression(*43*). However, most current biomaterial approaches to the niche lack these important interactions and signaling events.

Metastasis of cancer cells further depends on the ability of cancer cells to migrate through the stroma, intravasate blood vessels, survive in the circulation and extravasate into new matrix to colonize distant tissues (Figure 1.1). Although no hydrogel system to date mimics all these stages, materials-based microphysiological systems have been explored to mimic specific steps in this process, such as extravasation, in which cancer cells pass through the endothelium; for example, microphysiological systems can be fabricated using PDMS to engineer a perfusable microvascular network with hydrogel regions and media channels. Such systems are thin and composed of neo-vessels, allowing imaging analysis to study transendothelial migration(*44*). By applying this in vitro approach, it has been shown that tumor necrosis factor (TNF)α increases endothelial cell permeability, facilitates tumor cell intravasation(*45*) and modulates extravasation(*46, 47*). Microphysiological systems can also be used to investigate metastasis of certain cancer cells to specific secondary sites. For example, a microenvironment containing osteoblasts can be used to elucidate why breast cancer cells preferentially metastasize to bone. A higher number of breast cancer cells extravasate into the bone cell-conditioned microenvironment than into a collagen matrix, suggesting that bone-secreted chemokines such as CXC-chemokine ligand 5 (CXCL5) play a role in the chemotactic migration of breast cancer cells(*48*). These systems enable the investigation of the contribution of specific families of cell-secreted cytokines to cancer cell metastasis, which is difficult to dissect in animal models. Further development of microfluidic devices and incorporation of various

materials will make in vitro models increasingly relevant for cancer biologists as reductionist systems to recreate more steps of the metastatic process within one system.

1.4 Capturing cells in blood and stroma

Biomaterials can be applied for diagnostic and prognostic screening of cancer in vivo and ex vivo (Figure 1.3). The current standard of care primarily consists of regular screenings, such as mammograms for breast cancer, flexible sigmoidoscopy or fecal occult blood test for colorectal cancer(*49*) and computed tomography and chest radiography scans for lung cancer(*50*). However, by the time the disease is observable, the tumor has often already metastasized. To detect tumors in patients earlier and more accurately, biopsy samples can be taken and genetically tested for prognostic markers, for example, breast cancer markers breast cancer type 1 susceptibility protein (BRCA1) and ERBB2 by using mRNA microarrays(*51*). Such assays have dramatically reduced cancer occurrence; however, they do not directly detect disease-causing cells.

Biomaterial-based technologies have primarily focused on capturing circulating tumor cells (CTCs). CTCs are a small fraction of cells that disseminate from primary tumors and are thought to be responsible for the haematogenic spread of cancer to distant sites(*22, 52*). Increased CTC levels in the blood are correlated with negative prognosis. Therefore, CTC isolation and quantification are essential for the early detection of metastasis and subsequent treatment(*22*). However, CTCs are difficult to isolate with high efficiency and purity(*52*) and thus their unique molecular signatures remain elusive(*22*). The most commonly used CTC isolation method relies on increased epithelial cell adhesion molecule (EPCAM) expression on the surface of CTCs(*52*), which is used by the US Food

and Drug Administration (FDA)-approved CellSearch System. However, this system requires a very large sample volume, has low sensitivity and is time consuming(*52*).

1.4.1 Ex vivo detection using nano-topographies

CTC capture efficiency can be improved by increasing the local concentration of capture substrate or by coupling the substrate with surface functionalizing molecules, such as antibodies or aptamers. For example, microfluidic chip assays composed of PDMS microposts with a surface coating of anti-EPCAM antibody can concentrate CTCs in smaller sample volumes(*50*) than systems without antibody coating. Silicon nanopillars further improve CTC capture by clustering antibodies through binding to streptavidin or gold(*53*). Aptamer-functionalized gold nanopillar arrays show efficient cell release through cleavage of the sulfur–gold bonds between the aptamers and the gold nanopillars(*54*).

CTC purification and capture can also be achieved using artificial nanoscale topographies, mimicking structural features and dimensions of ECM(*52*). Cancer cells preferentially adhere to nanostructured rough substrates compared with smooth substrates, even in the absence of surface functionalization with antibodies(*22*). For

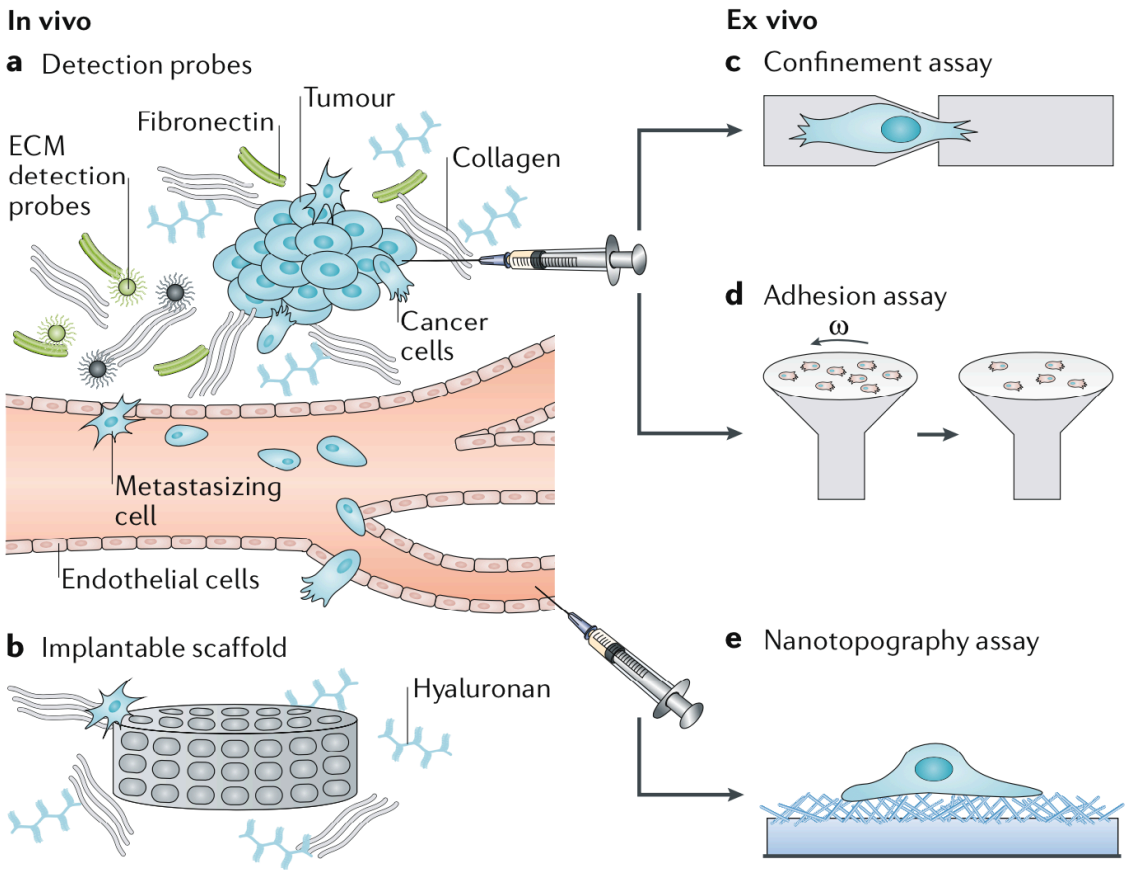

Figure 1.3 Next-generation material-based cancer technologies.

The specific interactions between cancer cells and the tumor stroma can be exploited for the detection of cancer cells. **a** | Magnetic resonance imaging (MRI) or positron emission tomography (PET) contrast agents can be conjugated with extracellular matrix (ECM)-affinity peptides to create specific probes to target the dense ECM of the tumor stroma for the detection of mature tumors in vivo. **b** | Implantable scaffolds can be used to recreate a pre-metastatic niche at the implant site, recruiting cells for capture and therapy and at the same time lowering the tumor burden in typical secondary metastasis sites. **c,d** | Confinement assays or adhesion assays can be applied to test cells obtained from tumor biopsy samples for their aggressiveness by measuring cellular deformation or adhesion to specific ECM molecules. Omega (ω) is the angular velocity that defines the shear stress applied to cells. **e** | Circulating tumor cells (CTCs) can be isolated from patient blood samples using nano-topography assays that take advantage of the affinity of CTCs for nano-roughed substrates.

example, fractal nanostructures have an uneven topography and a crystalline structure, which increase cancer cell binding to the surface(*23, 24*).

Fractal nanostructures can be generated from synthetic materials, such as TiO_2, with inverse opal photonic crystals to mimic cellular components or natural materials, such as hydroxyapatite nanostructures of seashells(*24, 55*). Alternatively, rough nanoscale

substrates can be fabricated with an antiEPCAM antibody-coated, mesh-like silicon nanowire substrate and overlaid with a PDMS-based chaotic mixer(*56, 57*). These systems show a >95% capture efficiency of EPCAM-positive MCF7 breast cancer cells, which is more than 20-fold higher than EPCAM antibody-coated smooth substrates(*58, 59*). The addition of electrospun-thermoresponsive nanofibers enables an even higher capture efficiency and allows on-demand release and single-CTC analysis, for example, for next--generation sequencing(*57*). Cell release can also be achieved by using degradable zinc--phosphate nano-substrates(*60*).

Nanostructured surfaces enable high capture efficiency but cannot provide high cell purity owing to nonspecific cell adhesion. Dual-functional lipid coating can be applied to improve the capture specificity of nanopillars owing to the higher concentration of anti-body on the surface and inhibition of nonspecific cell adhesion(*61*). Poly(carboxybetaine methacrylate) brushes also decrease nonspecific cell adhesion, and the active carboxyl groups capture CTC-specific biomolecules(*62*). These nanostructure-based methods enable ex vivo detection of CTCs, demonstrating how specific ECM properties, such as topography, can be exploited to increase capture efficiency and provide a strategy for pro active disease monitoring. It has been suggested that CTC detection probability scales with patient mortality(*50*) and, thus, technologies for the continuous detection of CTCs could provide a strategy to detect cancer cell metastasis early enough to substantially increase patient survival.

1.4.2 In vivo cell detection using implantable materials

Biomaterials can also be implanted to monitor tumor progression in vivo(*63, 64*). According to Paget's seed and soil hypothesis, secondary metastases do not occur

randomly(*65*). Specific microenvironments are primed for tumor cell colonization through the presence of tumor-supportive fibroblasts, endothelial progenitor cells, immune cell secreted factors and ECM-remodeling events(*63, 64, 66*). Current imaging techniques are limited in their ability to detect micro-metastases that form at distal sites(*63, 64, 66*), which reduces their prognostic capabilities and offers an area of opportunity for biomaterial-based solutions.

For example, microporous scaffolds such as poly(lactide-co-glycolide) acid (PLGA) can be implanted to recruit and capture metastasized cells. Breast cancer cells that have metastasized to the brain can be injected into the fat pads of mice and entrapped in an implanted PLGA scaffold. Mice with scaffolds implanted to capture circulating cells develop fewer lung tumors(*64*) than animals without any implanted material, indicating that the scaffolds reduce secondary metastases formation. Poly(ε-caprolactone) (PCL) has similar physical proper ties to PLGA but degrades more slowly(*63*). PCL scaffolds can also be used to recruit tumor and immune cells, which are implicated in establishing a premetastatic niche, and to decrease the number of detectable tumor cells in common secondary sites(*63, 67-69*). Additional modifications, such as graphene oxide (GO) functionalization, can further increase cancer cell adhesion compared with non-functionalized scaffolds(*70*). GO addition to the scaffold can also enable photothermal ablation of cancer cells within the scaffold owing to the near-infrared absorbance of GO(*70, 71*), demonstrating how implantable scaffolds can be used for both cancer cell capture and therapy. Besides chemical modifications, scaffolds can also be coated with ECM proteins, including fibronectin and type IV collagen, to improve scaffold capture efficiency. Each tumor type is characterized by specific ECM combinations and thus

scaffolds can be coated with a tumor-specific ECM that supports metastases(*16*) to improve cancer cell recruitment. For example, coating with decellularized lung or liver matrix of metastatic tumors substantially increases capture efficiency(*66*).

Matrix is not the only niche component that can be used to improve cell capture. Cancer cell-secreted exosomes or haptoglobin can also be incorporated into synthetic scaffolds to create a bioengineered niche that captures metastatic cells more effectively than tissues to which cells commonly metastasize and increases survival in animals implanted with these scaffolds(*72, 73*). Natural materials such as silk can also be functionalized with proteins, such as bone morphogenetic protein 2 (BMP2), to mimic a bone marrow microenvironment. This material can serve as a surrogate for a premetastatic niche and recruit metastasizing cancer cells that would normally home to bone marrow(*74*). In particular, BMP2 increases the adhesion of metastatic prostate and breast cancer cell lines to the scaffold(*74, 75*). Such scaffolds can be implanted to capture tumor cells, reduce the tumor burden on standard metastatic organs and prevent the local remodeling of tissue into a premetastatic niche, making them potent therapeutic tools to detect, capture and ablate metastasized cancer cells. However, these scaffolds do not have an inherent proclivity to capture specific cell types.

1.4.3 Ex vivo cell detection using physical properties

Cells migrate through the stromal ECM through con fined pores, which can be smaller than the nucleus of the cell. To achieve this, cells can either degrade adjacent matrix using MMPs(*76*) or physically deform it(*77*). Increased MMP expression and decreased nuclear size(*78, 79*) are associated with aggressive cancers and thus cell deformability is emerging as a marker for the invasive potential of cancer cells(*80*). Assays for the inves-

tigation of cellular deformability exploit the variable pore size in the ECM to shed light on the relationship between the degree of deformation and the corresponding invasive and metastatic potential. The most common strategy is to microfabricate channels — for example, in PDMS — with defined geometries and track cellular movement. Cells with low expression of nuclear lamina proteins, which contribute to nuclear stiffness, pass more quickly through narrow regions(*77*) than cells with high lamin A and/or lamin C expression and stiff nuclei. Specific deformation tolerances can be assessed using funnel-shaped constrictions in series(*81*) or in parallel to analyze cell transition effects(*82*). Metastatic cells modulate their morphology, as they are forced into confined spaces more than their nonmetastatic counterparts, resulting in faster and larger deformation events(*82*). Highly metastatic cells can even rupture and reassemble their nuclear envelops when they encounter transit constrictions(*35*). Intravasation constitutes one of the most restrictive parts of the journey of a metastasizing cell. Microfluidic devices with cell and nutrient chambers separated by microchannels of varying width can be used to determine the minimum gap that cancer cells can migrate through in confined environments. Such a device has been applied to demonstrate that the nucleus is a crucial limiting factor for a cell to be able to traverse confined environments(*83*).

Constrictive devices rely on cell-generated forces; alternatively, external hydrodynamic forces can be applied to deform cells. Opposing flows, that is, hydro dynamic stretching, can uniformly deform cells, and the degree of deformation can be controlled by simply changing the flow rate(*84*) or through pinched-flow stretching in a single inlet(*85*). The latter design forces cells to flow in the center of the channel, siphons fluid on the sides of the channel away from the cells and then compresses the cells when

the fluid is added back to the channel(*85*). These assays can be applied to analyze cell deformability of single cells or populations of cells using pressure-driven microfiltration systems. Using these systems, it has been observed that induction of EMT or drug resistance leads to an increase in cell deformability(*86*). Such microfiltration devices enable high-throughput assessment of transit time and deformability(*87*) to investigate a population of cells from a tumor. These assays, applying forces either internally or externally, measure internal features of the cytoskeleton that are found in metastatic but not in nonmetastatic cells. Therefore, microchannel assays can be useful as diagnostic tools to assess the aggressiveness of cells isolated from tumor biopsy samples and to observe the effect of cancer therapies on cell deformability and thus disease progression.

Adhesion properties and mechanisms provide another physical metric to determine the metastatic potential of cancer cells. Assays that apply negative pressure to detach cells(*88*), to assess binding efficiencies to ECMs(*89*) or to analyze adhesion turnover(*90*) have demonstrated that adhesion is modulated differentially in meta static cancer cells compared with in nonmetastatic cells. For example, metastatic cancer cells can move rapidly through tissue through increased cation sensitivity that leads to more rapid formation and disassembly of focal adhesions than in their nonmetastatic counterparts(*91*). Cell–matrix adhesions are directly modulated by magnesium, manganese and calcium cations, which increase integrin affinities for matrix proteins in proportion to their concentration. The concentration of cations is ten fold lower in the stroma than in the tumor(*92, 93*). Thus, once metastatic cells reach the stroma, only cells with labile adhesions can migrate. Indeed, cancer cell adhesion strength to fibronectin and type I collagen at low cation conditions correlates with metastatic potential; within a highly metastatic cell

population, the subset of cells with high adhesion strength is less migratory and invasive than malignant and noncancerous epithelial cells or strongly adherent metastatic cells(*91*). Analyzing the weakly adherent cell fraction enables the determination of the metastatic potential of a tumor in situ. Each of the above-discussed assays yields valuable information about the metastatic potential of cancer cells, which could make such devices useful diagnostic tools for prognostic assessment and for determining a course of treatment.

1.4.4 Non-invasive surveillance of tumor-adjacent stroma

Interaction with the surrounding matrix is an important regulator of cell dissemination, and various matrix properties can act as markers to detect and/or capture highly invasive cells that are predisposed towards tumor formation. Exploiting the similarities of tumor microenvironments across different cancer types opens up avenues for monitoring the presence and growth of primary tumors. For example, overexpression of integrins, common matrix signatures(*16*) and overexpression of specific MMPs can act as prognostic indicators of the metastatic potential of tumors in patients with primary breast tumors(*94*). Unlike most physical parameters of the ECM, the composition of the tumor--adjacent stroma can be noninvasively monitored, making it an attractive property for the assessment of tumor progression in patients.

In addition to biochemical surveillance, imaging methods are also being explored using material-based probes. For example, a combination of high-affinity fibrin peptides and tracer molecules (that is, radioisotopes) that are detectable by magnetic resonance imaging (MRI) or single photon emission computed tomography (SPECT) are being developed to assess increased fibrin deposition in tumors(*95, 96*). Antigen-binding fragment (Fab) probes can be combined with a radioisotope to image fibrin clots in the

tumor microenvironment(*97*). Such probes also demonstrate low retention times in non-target tissue in vivo(*96, 98*). Fibronectin is also over expressed during EMT, making it a prime target for early cancer detection probes(*94, 99-101*). Similar to MRI contrast agents for fibrin, gadolinium-based MRI contrast agents can be used to target fibronectin–fibrin complexes, demonstrating robust detection of the primary tumor and of >0.5 mm^3 micro-metastases(*99*). Most current strategies target major ECM components; however, probes that target more tumor-specific ECM elements, such as periostin in esophageal cancer(*102*), could improve detection specificity, decrease background signaling through rapid clearance of non-bound contrast agents(*94*) and increase tissue penetration depth owing to their small size. These approaches, which are still being developed, enable us to image tumors with increasing spatial resolution, but they do not provide information about the aggressiveness of tumors.

1.5 Perspectives and conclusion

Strategies to understand and detect tumors have greatly improved our ability to recognize and assess specific tumor pathways and cell behaviors that are indicative of disease progression. As the field matures, cancer diagnosis and treatment will most certainly involve more materials-based approaches to address shortcomings in our ability to model, detect and treat cancer. Despite the development of a variety of dynamic, synthetic biomaterials applicable for the modelling and study of cancer, Matrigel is still most commonly used by cancer biologists for 3D cell culture systems even though it is highly variable, difficult to purify and derived from a mouse tumor. Therefore, the field of

material science must continue to evolve and incorporate tunable synthetic materials to help understand the cell behaviors induced by these increasingly complex materials.

As the biomaterials community, we also aim to clinically translate lessons learned from in vitro models to diagnostic assays. The substantial progress made in our understanding of the tumor as a material and in detecting and capturing cancer cells makes this an exciting time for material based cancer research. There are great opportunities to improve our basic understanding of cancer and also our detection and treatment capabilities, for example, investigating tumor–stroma interactions in reductionist matrix systems, developing a complete tumor-in-a-dish model (including intravasation and extravasation) and understanding how ani mal models reflect clinical outcomes. Improvement of detection probes using biomaterials, whether invasive or not, is also a growing research area, which is reflected in the expanding body of literature. For example, during tumor growth, collagen, fibrin and hyaluronan concentrations increase in the surrounding ECM, and the matrix stiffens and is aligned by lysyl-oxidases(*5, 103, 104*) to facilitate invasion(*94, 105*). Potential therapeutic avenues include the use of proteases to degrade matrix proteins and decrease stiffness to improve drug penetration. Conversely, hyaluronidase, which degrades the extracellular glycosaminoglycan hyaluronan, can be inhibited to limit tumor growth and metastasis(*106, 107*). Clinical trials of hyaluronidase delivery have demonstrated its safety(*108*), and a phase III study is currently being conducted (NCT02715804). Finally, future improvements in treatment options using biomaterials will ultimately impact clinical outcomes. For example, altering ECM structure could improve nanoparticle and drug delivery, resulting in more effective, deeper--penetrating therapies and improved patient outcomes(*103, 109-112*). In addition to

enzymatic strategies, physical disruption of the matrix using high intensity ultrasound can be used to improve the penetration of nanoparticles into the tumor tissue without damaging sur rounding tissues(*109*). Thermal strategies with nanotubes(*113*) or gold nanorods(*114*) can also be applied to denature the collagen matrix and increase tumor diffusivity.

Using biomaterials for the modelling, detection and treatment of cancer is a promising strategy. Another important contribution of material science in the near future will be to help rectify the differences in disease progression and treatment between humans, animal models and patient-derived xenografts(*115*). Biomaterial-based models are reductionist in nature; thus, their application in vivo could improve the reliability of animal models, making them more predictive of patient outcomes(*116*). Animal models are considered the standard assay for tumor biology, and material-based in vivo strategies are required to understand the differences between humans and animal models. For example, recombinant, chemically defined natural(*117*) or synthetic(*11*) biomaterials could be used that can actively modify tissue properties(*5*). Such materials have already enabled the identification of cancer stem cells and mechano-transduction mechanisms and have demonstrated how material properties can drive tumorigenesis, making future applications in vivo promising.

The examples discussed in this chapter demonstrate that biomaterials can serve as powerful tools to replicate mechanisms of disease and the response to treatments in vitro. The materials-based strategies that have enabled these discoveries should be broadly applied in the future to further improve our understanding of cancer biology and to begin to impact clinical outcomes.

1.6 Acknowledgements

Funding for this work was provided by US National Institutes of Health grants R01CA206880 (A.J.E. and J.Y.) and R21CA217735 (A.J.E.), a US National Science Foundation grant 1463689 (A.J.E.) and the Graduate Research Fellowship program (P.B.). Additional fellowship support was provided by Brazilian Federal Agency for Support and Evaluation of Graduate Education award 88881.135357/2016-01 (B.F.M.).

Chapter 1, in full, is a modification of the material as it appears in: Beri, P., Matte, B.F, Fattet, L., Kim, D., Yang, J., and Engler, A.J. "Biomaterials to model and measure epithelial cancers" *Nature Rev Materials*, 2018. 3, 418-430. The dissertation author was the primary author of this paper.

Chapter 2.

Metastatic state of cancer cells may be indicated by adhesion strength

2.1 Abstract

Cancer cells within a tumor are heterogeneous and only a small fraction are able to form secondary tumors. Universal biological markers that clearly identify potentially metastatic cells are limited, which complicates isolation and further study. However, using physical rather than biological characteristics, we have identified Mg^{2+}- and Ca^{2+}-mediated differences in adhesion strength between metastatic and nonmetastatic mammary epithelial cell lines, which occur over concentration ranges similar to those found in tumor stroma. Metastatic cells exhibit remarkable heterogeneity in their adhesion strength under stromal-like conditions, unlike their nonmetastatic counterparts, which exhibit Mg^{2+}- and Ca^{2+}-insensitive adhesion. This heterogeneity is the result of increased sensitivity to Mg^{2+}- and Ca^{2+}-mediated focal adhesion disassembly in metastatic cells, rather than changes in integrin expression or focal adhesion phosphorylation. Strongly adherent metastatic cells exhibit less migratory behavior, similar to nonmetastatic cell lines but contrary to the unselected metastatic cell population. Adhesion strength heterogeneity was observed across multiple cancer cell lines as well as isogenically, suggesting that adhesion strength may serve as a general marker of metastatic cells.

2.2 Introduction

Cancer cell dissemination is a highly coordinated process in which a cell detaches and migrates away from the primary tumor to form a secondary metastatic site(*118*). However, only a small subset of cancer cells from a tumor or even from a cancer cell line are capable of causing secondary tumors in vivo(*117*). Successful dissemination requires collagen fiber deposition, alignment, and cross-linking in the adjacent stromal matrix(*3, 5*) to create tracks on which cells migrate. However, this will only occur in cells with labile adhesions(*119*). Focal adhesion (FA) turnover permits the migration required of invasive cancer cells(*120*), which tend to have more dynamic FAs than noninvasive cancer cells(*90, 121*). Due to the lack of a consistent set of biomarkers that predict metastatic potential across solid tumors(*122*), a systematic quantification of adhesion strength could result in a unique biophysical metric to identify highly metastatic cells within a broader tumor cell population. Furthermore, a quantification of tumor cell adhesion strength could serve as a predictor of the metastatic potential of a solid tumor.

Population-based adhesion assays, e.g., the spinning-disk shear assay(*123*), can monitor FAs by measuring adhesion strength. Specifically, by analyzing the magnitude of shear needed to detach 75% of the cell population (denoted by τ_{25}), we are able to quantify the adhesion strength of a cell population and correlate it with FA assembly. In addition, the spinning-disk shear assay can capture adhesion heterogeneity within a population(*124*). For example, by plotting a log shear stress versus linear cell density profile, we are able to analyze the logarithmic slope for the resulting sigmoidal curve. From these data, we are able to determine the attachment heterogeneity of a cell type in a variety of conditions. In contrast, single-cell, single-shear, and wash assays cannot quantify these values(*16, 88,*

121, 125-127). Although some studies have shown a correlation between changes in adhesion and secondary tumor development(*16, 88, 127*), substantial phenotypic heterogeneity can exist even within a single cancer cell line(*128*). Thus, understanding the adhesive heterogeneity within an invasive population may improve our ability to physically monitor cancer cells and predict invasive behavior. Population-based adhesion assays also provide a reductionist niche for determining sensitivity to culture conditions (e.g., cation concentration and matrix composition)(*124*). This is especially important because breast tumors have higher magnesium (Mg) and calcium (Ca) concentrations than healthy breast tissue(*92, 93*). Clinically, lower stromal cation concentrations have been associated with increasingly metastatic(*129*) and aggressive(*130*) tumors. As cancer cells migrate into the stroma, lower Mg^{2+} and Ca^{2+} concentrations may decrease integrin activation(*131*) and clustering(*132, 133*), thus favoring the labile adhesions required for cancer cell migration(*119*). These data appear consistent with observations that integrin activation is inversely proportional to the metastatic potential of mammary cell lines(*121*), whereas traction forces are proportional(*8*). These data collectively suggest that heterogeneity in the adhesion-strength profile in stromal conditions may act as a biophysical marker, indicating the presence of a subset of metastatic cancer cells that are capable of disseminating into the stroma with lower Mg^{2+} and Ca^{2+} concentrations. Thus, we hypothesize that strongly adherent cells within a metastatic cell line will be the least migratory, and that adhesion strength is regulated by the sensitivity of assembled FAs to stromal $Mg^{2+}$and Ca^{2+} concentrations.

To understand how Mg^{2+} and Ca^{2+} influences cancer cell adhesion, we performed a spinning-disk analysis on epithelial and invasive cancer cell lines across a spectrum of

metastatic potentials while varying the Mg^{2+} and Ca^{2+} levels. We observed a remarkable cellular heterogeneity and a decrease in cellular adhesion strength during the spinning-disk analysis. This was quantified by a decrease in logarithmic slope and a leftward shift in the τ_{25} value when shear stress was plotted versus cell density. This phenotype was only present in low Mg^{2+} and Ca^{2+} conditions for metastatic cell lines. These observations correlated with FA disassembly and were recapitulated in nonmetastatic cell lines that had been transformed to mirror their metastatic counterparts. The data further establish that metastatic cells with less labile adhesions and higher adhesion strength have reduced migration in collagen gels and transwell assays. These behaviors were independent of tumor and tissue type and were demonstrated isogenically. These results support the concept that adhesion strength may act as a universal biophysical regulator of metastasis.

2.3 Results

2.3.1 Mg^{2+} and Ca^{2+} concentrations influence the adhesion heterogeneity of metastatic cells

To disseminate from primary tumors, metastatic cancer cells must invade adjacent stroma, which requires a transition from stable to labile adhesion. Using a spinning-disk device (Fig. S2.1), we measured the adhesion strength, τ_{25}, of mammary epithelial cell lines of varying metastatic potential. At physiological (serum) cation concentrations, i.e., 0.5 mM Mg^{2+} and 1 mM Ca^{2+} (denoted as PBS + MgCa), the adhesion strengths of nontumorigenic MCF10A cells, tumorigenic but not metastatic MCF7 cells, and tumorigenic and metastatic MDAMB231 cells to fibronectin were very similar, with no dramatic differences (Figure 2.1, black). Mg^{2+} and Ca^{2+} concentrations differ between a

healthy niche and tumor niche(*92, 93*), and their removal during 5 min of shear application only slightly reduced the adhesion strength of MCF10A and MCF7 cells. However, the removal of Mg^{2+} and Ca^{2+} significantly reduced MDAMB231 cell adhesion strength (Figure 2.1, red) by more than an order of magnitude (Figure 2.1E). Notably, the cell adhesion strength of the latter metastatic cell line was very heterogeneously distributed, with a significantly lower logarithmic slope versus nonmetastatic lines (Figure 2.1F). Given the significant genetic differences between these lines, we also assessed the adhesion strength of H-Ras-transformed MCF10A cells (labeled MCF10AT cells), which give rise to invasive carcinoma in vivo(*134*). As was the case with MDAMB231 cells, the MCF10AT cells showed Mg^{2+} and Ca^{2+} sensitivity, with lower τ_{25} and slightly more heterogeneity than MCF10A cells (Figure 2.1D, open versus closed data points). In contrast to fibroblasts(*124*), shear forces in the presence of Mg^{2+} and Ca^{2+} did not induce large changes in size for any of the cell lines tested. Furthermore, in the presence of Mg^{2+} and Ca^{2+}, variation in cell size across different cell lines was within the same order of magnitude. In these analyses, we visually assessed the cells to ensure that they were sufficiently spaced apart to prevent cell-cell interactions from disrupting the shear analysis (Fig. S2.2).

Although these data were obtained over a wide range of Mg^{2+} and Ca^{2+} concentrations, concentration gradients likely exist between the tumor and adjacent

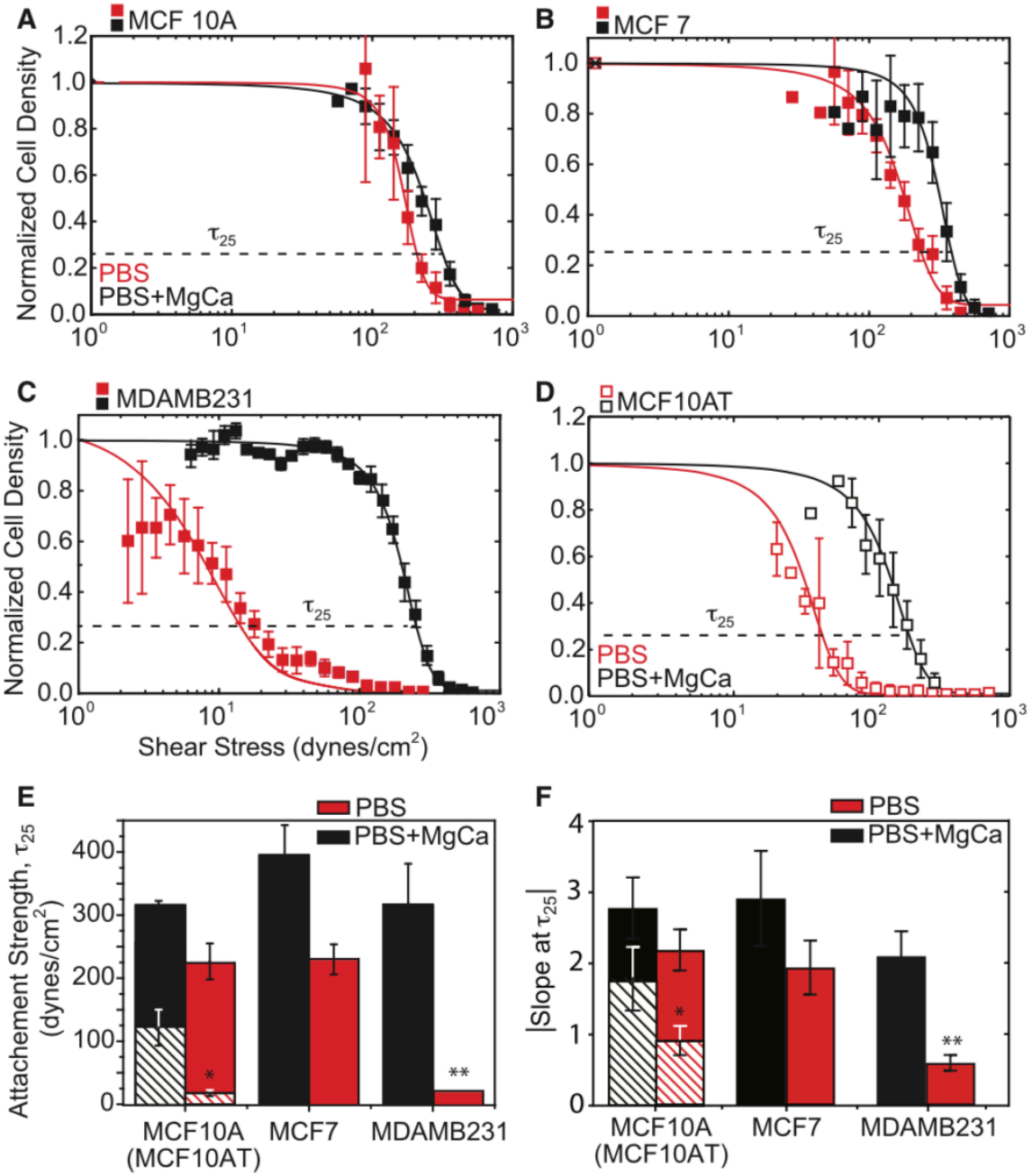

Figure 2.1. Adhesion strength is heterogeneous for metastatic mammary epithelial cells in a stromal-like niche.

(A–D) Normalized cell density is plotted versus shear stress for (A) MCF10A (closed) and MCFA10T (open), (B) MCF7, (C) MDAMB231, and (D) MCF10AT cells. Shear stress was applied in buffer with (black) and without (red) 0.5 mM Mg^{2+} and 1 mM Ca^{2+}. t25, i.e., the shear to detach 25% of cells (also referred to as adhesion strength) is indicated in each plot. (E) Plot showing the average adhesion strength for cells exposed to shear in PBS buffer with (black) and without (red) cations. Crosshatched bars indicate data from MCF10AT cells. (F) Plot of the absolute magnitude of the logarithmic fit slope for each cell line and cation condition. All shear plots represent binned averages from biological triplicate experiments performed across multiple, overlapping shear ranges. All adhesion-strength assays were performed using fibronectin-coated coverslips. All other plots have n > 3. To see this figure in color, go online.

stroma(*92, 93*). We found that homogeneous and strong adhesion strengths for metastatic cells, i.e., high τ_{25} and a logarithmic fit slope in density versus shear plots, could be gradually restored with increasing cation concentrations (Fig. 2.2 A), independently of cation type (Mg or Ca), with significant sensitivity at tumor and adjacent stroma concentrations (Fig. 2.2 B). Mg^{2+}- and Ca^{2+}-dependent adhesion heterogeneity was also observed on type I collagen and could be gradually restored with increasing Mg^{2+} and Ca^{2+} concentrations (Fig. 2.2, C and D). Conversely, adhesion strength changes were minimal for nontumorigenic cells, which always exhibited strong adhesion (Fig. S2.3). Thus, metastatic mammary epithelial cells likely adhere in a metastatic- potential-dependent manner based on a subset of FA parameters.

Adhesive heterogeneity also extends beyond MDAMB231 cells to other metastatic cells. For comparison, we analyzed metastatic MDAMB468 and SUM1315 mammary cells by spinning-disk assay to determine the heterogeneity of their adhesion strength. The cells were sufficiently spaced apart to enable measurements of only the cell- matrix adhesion strength(*135*) (Fig. S2.2). Although it was not as robust as that observed for MDAMB231 cells, their adhesion strength was also heterogeneously distributed in terms of a lower τ_{25} and logarithmic fit slope, especially in comparison with BT20, an invasive but non-metastatic mammary cell line, and BT549, a nonmalignant and nonmetastatic mammary cell line. PC-3 prostate carcinoma cells, a tumorigenic and highly metastatic cell line, also exhibited heterogeneously distributed adhesion (Fig. S2.4), indicating that common FA parameters may make adhesion strength a unique biophysical metric of cell state.

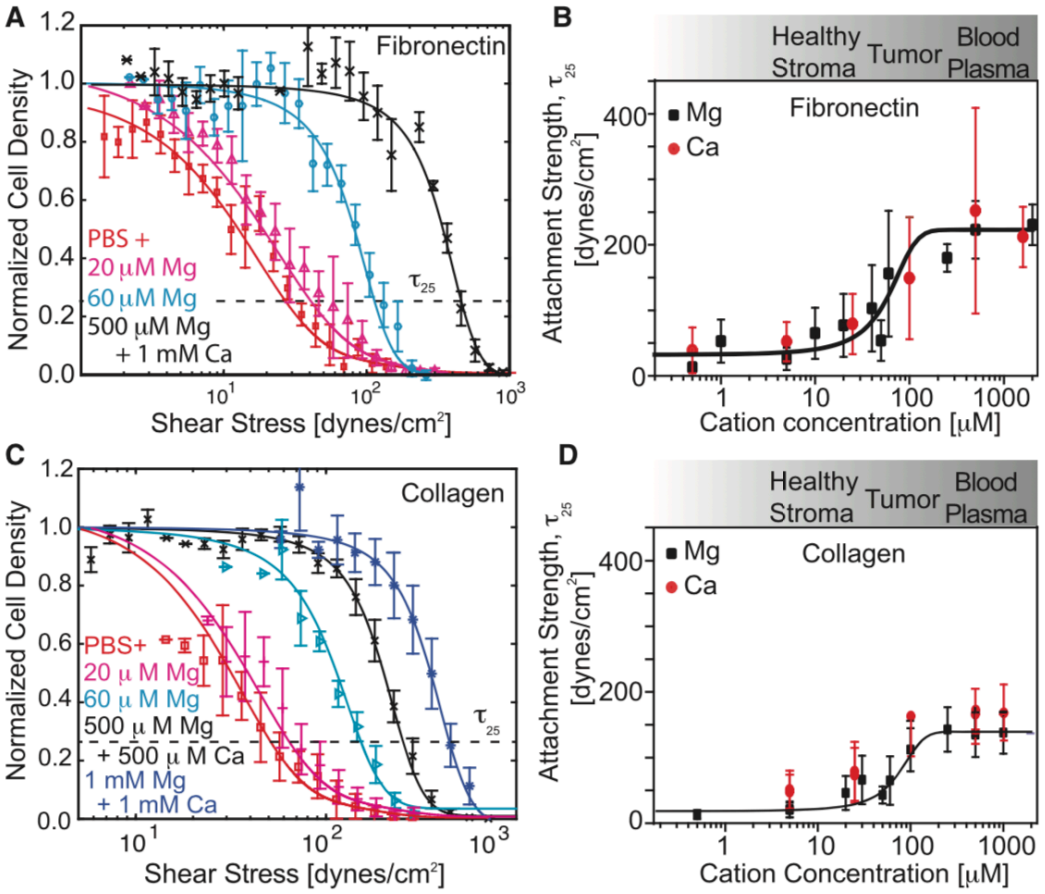

Figure 2.2. Adhesion strength can be titrated but is independent of the matrix ligand type.

(A) Representative plot for MDAMB231 cells bound to fibronectin-coated coverslips versus the applied shear. Each color corresponds to the indicated cation condition; τ_{25} is indicated. (B) Plot of the average τ_{25} adhesion strength for MDAMB231 cells bound to fibronectin-coated coverslips versus cation concentration. The data are plotted separately for modulation of Mg^{2+} (black squares) or Ca^{2+} (red circles), but the sigmoidal fit is for the combined data. The cation concentration range for the indicated tissue is provided for reference based on Seltzer et al.(*92, 93*). (C) Representative plot for MDAMB231 cells bound to collagen type I-coated coverslips versus the applied shear. Each color corresponds to the indicated cation condition; τ_{25} is indicated. (D) Plot of the average τ_{25} adhesion strength for MDAMB231 cells bound to collagen type I-coated coverslips versus cation concentra- tion. The data are plotted separately for modula- tion of Mg^{2+} (black squares) or Ca^{2+} (red circles), but the sigmoidal fit is for the combined data. All shear plots represent binned averages from biological triplicate experiments performed across multiple, overlapping shear ranges. All other plots have n > 3. To see this figure in color, go online.

2.3.2 Adhesion heterogeneity correlates with a migratory phenotype

Although metastatic mammary epithelial cells display adhesive heterogeneity in a niche with low concentrations of Mg and Ca, it remains unclear how adhesion differences affect migration. We assessed cell migration in cell media containing physiological Mg

and Ca concentrations first by selecting for strongly adherent cells, as outlined in Fig. 2.3 A. Migration appeared to change with relative adhesive heterogeneity in the absence of Mg and Ca; for example, minimal migration was observed for MCF10A cells and MDAMB231 cells selected with 45 dynes/cm^2 shear, whereas unselected MDAMB231 cells were significantly more motile (Fig. 2.3 B) and progressive in their migration. Migration of unselected MDAMB231 cells in collagen gels was increasingly persistent and linear with collagen concentration. Conversely, strongly adherent cells selected with high shear progressively lost their persistent, linear migration (Fig. 2.3 C). Other metastatic mammary cells, i.e., SUM1315, also demonstrated adhesive heterogeneity (Fig. S2.4), exhibiting more persistent, linear migration on collagen-coated, planar substrates than on collagen hydrogels. Migration of unselected SUM1315 cells, however, was more persistent and linear on collagen hydrogels compared with strongly adhering cells (Fig. S2.5 A). Migration of PC3 prostate cancer cells was also more persistent and linear with the unselected cell population (Fig. S2.5 B). These data suggest that shear selection can selectively isolate highly adhesive, Mg- and Ca-independent MDAMB231 cells, which appear to be less migratory than unselected MDAMB231 cells. Cell migration was also assessed using a transwell assay over 48 h. Relative to MCF10A cells, twice as many unselected MDAMB231 cells migrated through the pores. Metastatic cells demonstrating a strongly adherent phenotype during shear selection also exhibited decreased migration in the transwell assay. Interestingly, a significant number of MDAMB231 cells detached from the transwell insert and reattached to the chamber bottom. Significantly more MDAMB231 cells underwent this process compared with

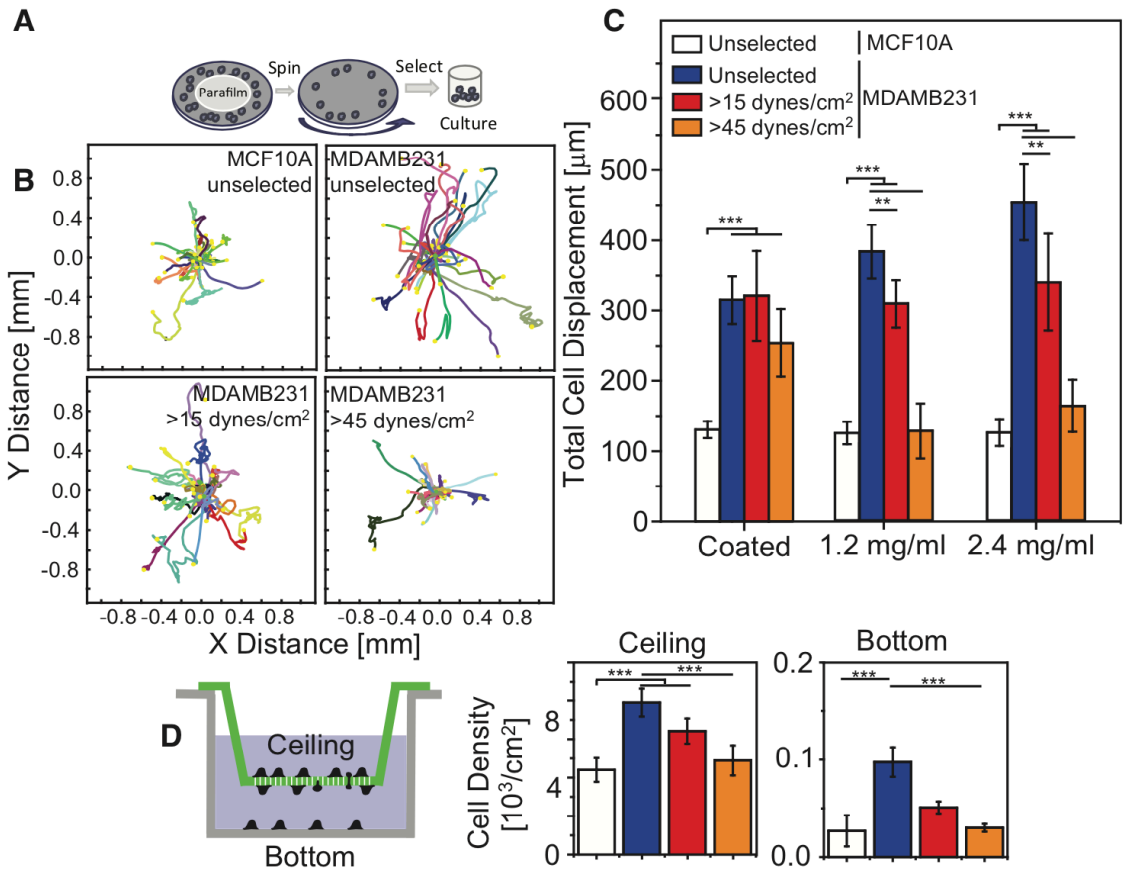

Figure 2.3. The weakly adherent subpopulation of MDAMB231 cells is highly migratory.

(A) Schematic of the selection assay, where Parafilm is used to block the center of the coverslip so that cells only adhere to regions exposed to high shear stress. After trypsinization from collagen- coated coverslips, the cells are re-plated in migration or transwell assays. (B) Rose plots of cell migration trajectories for the indicated cell lines and shear stress selection conditions. Each trajectory represents an individual cell path on a collagen-coated substrate, as observed over 24 h. (C) Total cell displacement over 24 h for the indicated cell lines, shear stress selection conditions, and substrates. Each bar represents experiments performed in biological triplicate with >20 per sample and with each cell trajectory quantified at 15 min intervals over 24 h of imaging. (D) At left is an illustration of the transwell migration assay, indicating cells that have migrated through the pores of the membrane (green; referred to as the ceiling) and those cells that subsequently detached and reattached to the bottom of the well (gray). At right are graphs of cell density for the indicated cell lines and shear stress selection conditions. Cell densities on the ceiling of the insert (top) and bottom of the well (bottom) are shown separately and represent the results of triplicate biological replicates. **p < 0.01, ***p < 0.001.

MCF10A (Fig. 2.3 D). Thus, the highly adhesive, Mg- and Ca-independent MDAMB231 cells appear to be less migratory than their unselected counterparts, which contain a highly migratory subpopulation.

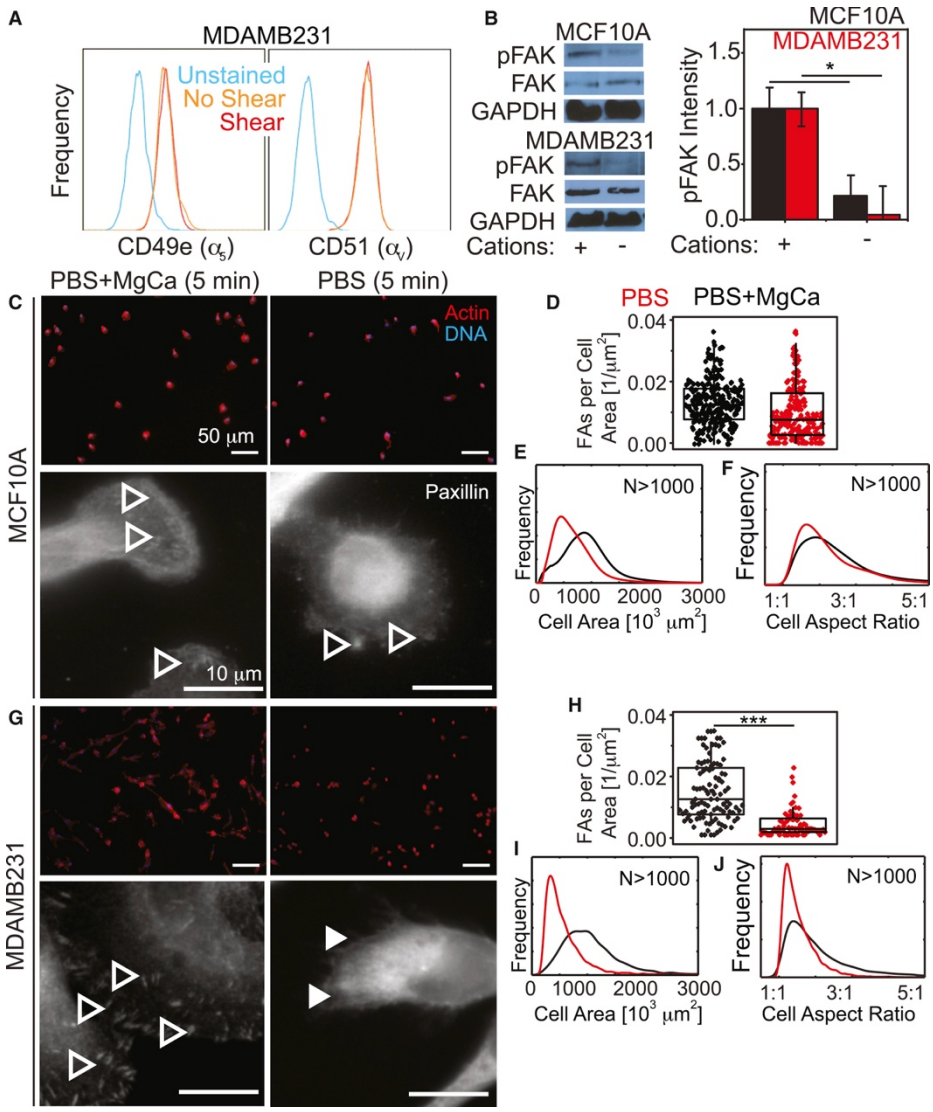

Figure 2.4. FAs are more Mg^{2+} and Ca^{2+} sensitive in MDAMB231 cells than in MCF10A cells.

(*A*) Flow-cytometry profiles for the indicated integrins of MDAMB231 cells that were previously exposed (*red*) or not exposed (*orange*) to shear stress in the absence of cations. Unstained controls (*blue*) are shown for reference. (*B*) Representative Western blots for pFAK, total FAK, and GAPDH are shown for the indicated cells exposed to the indicated cation conditions for 5 min. Quantification of band intensity, normalized to GAPDH and total FAK, is shown for MCF10A and MDAMB231 cells with and without Mg^{2+} and Ca^{2+}. (*C*) Images of MCF10A cells in the indicated buffer conditions for 5 min without shear. Upper images are lower magnification and show cells stained for actin (*red*) and DNA (*blue*). Lower images are at higher magnification for the same conditions as the upper images and were stained for paxillin (*green*), actin (*red*), and DNA (*blue*). (*D*) Scatter plot of MCF10A cells, counting the number of FA plaques per square micron. (*E* and *F*) Frequency plots of MCF10A cell area and aspect ratio. (*G*) Images of MDAMB231 cells in the same conditions indicated in (*C*) for MCF10A cells. Open and closed arrowheads in (*C*) and (*G*) indicate cells with and without visible FAs, respectively. (*H*) Scatter plot of MDAMB231 cells, counting the number of FA plaques per square micron. (*I* and *J*) Frequency plots of MDAMB231 cell area and aspect ratio. In (*D–F*) and (*H–J*), cells incubated with and without cations for 5 min before measurement are shown in black and red, respectively. The scale bar represents 50 μm for all images. All adhesion assays were performed with fibronectin-coated coverslips. $^{***}p < 0.001$. All frequency and dot plots represent triplicate experiments analyzing 500+ cells per condition.

2.3.3 Labile FAs reduce adhesion strength and enhance migration in metastatic cells.

Although these data illustrate adhesive differences and their correlation to a migratory phenotype, they do not suggest an origin for these differences. Strongly adherent MDAMB231 cells did not differentially express integrins (Fig. 2.4 A), nor did phosphorylation of FAK change between MCF10A and MDAMB231 cells as a function of shear exposure (Fig. 2.4 B), suggesting a structural mechanism. Consistent with their adhesion strength, MCF10A cells did not fully disassemble their FAs (Fig. 2.4, C and D) and maintained their size and shape (Fig. 2.4, E and F) after Mg^{2+} and Ca^{2+} removal in the absence of shear. Conversely, metastatic MDAMB231 cells disassembled their FAs (Fig. 2.4, G and H) without significant changes in their size or morphology (Fig. 2.4, I and J). Thus, Mg^{2+} and Ca^{2+} sensitivity in the absence of shear suggests that MDAMB231 adhesions are transient and independent of the amount of elapsed culture time before shear application.

Although MCF10A cells did not exhibit Mg^{2+}- and Ca^{2+}- sensitive adhesion, we next asked whether we could induce FA disassembly and adhesion strength heterogeneity in these cells. Cells were seeded onto a fibronectin-coated substrate and pretreated with the fibronectin integrin-blocking peptide RGD. When the fibronectin-binding integrins were blocked, cells without Mg^{2+} and Ca^{2+} exhibited statistically fewer FAs per area (Fig. 2.5, A and B). These data are consistent with fewer FAs but a different distribution from

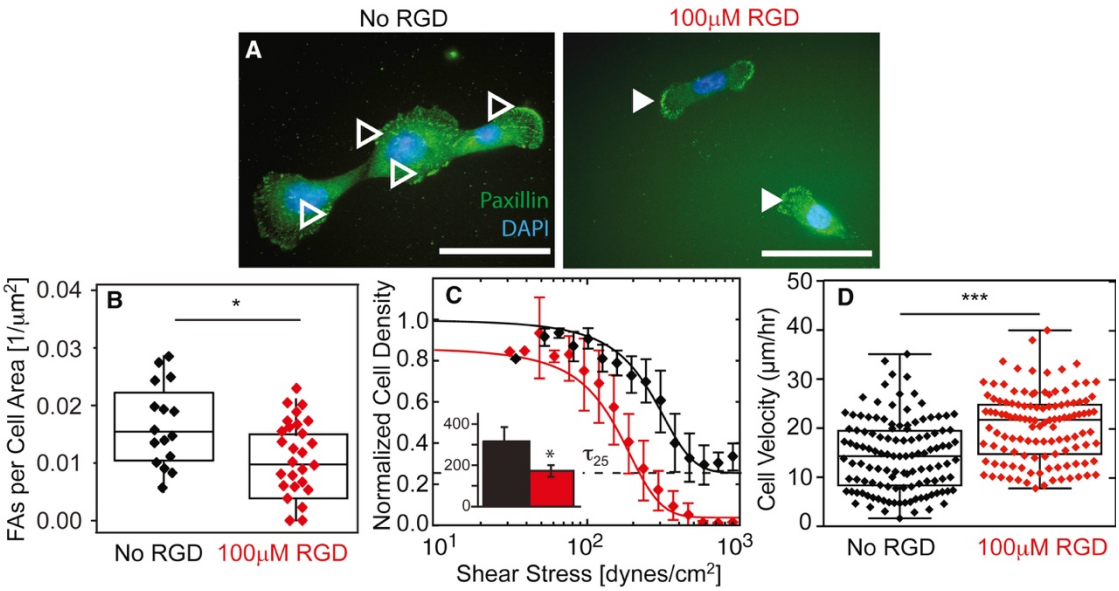

Figure 2.5. Integrin blocking reduces cation-dependent adhesion strength in nonmalignant cells. (*A*) MCF10A cells were stained for paxillin (*green*) and nuclei (*blue*). Open and closed arrowheads indicate FAs for the indicated RGD culture condition. Scale bars, 100 μm. (*B*) Plot of the number of FAs per cell area for cells without (*black*) and with (*red*) RGD. (*C*) Normalized cell density is plotted versus shear stress for cells without (*black*) and with (*red*) RGD. The inset shows the average τ_{25} adhesion strength for each condition in dynes per square centimeter. $^{*}p < 0.05$. All dot plots represent triplicate experiments analyzing >20 cells per condition. Shear plots represent binned averages from biological triplicate experiments performed across multiple, overlapping shear ranges. All adhesion-strength assays were performed using fibronectin-coated coverslips. (*D*) Plot of cell velocity, in micrometers per hour, for cells treated (*red*) or not treated (*black*) with RGD on fibronectin-coated coverslips. $^{***}p < 0.001$ for comparisons with unpaired *t*-test with Welch's correction. To see this figure in color, go online.

MDAMB231 cells (Fig. 2.5 B versus Fig. 2.4 H). When exposed to shear, RGD-treated MCF10A cells exhibited lower adhesion strengths but were not as heterogeneous as MDAMB231 cells (Fig. 2.5 C), possibly due to uniform integrin blocking with RGD ligand. Free RGD improved cell migration velocity (Fig. 2.5 D) to rates similar to those observed for MDAMB231 cells versus untreated nonmetastatic cells. Overall, these data suggest that FAs in metastatic cells are more Mg^{2+} and Ca^{2+} sensitive than those in non-metastatic cells and disassemble in stromal conditions (in contrast to nonmetastatic cells), thus driving the metastatic potential.

2.4 Discussion

Cancer is a heterogeneous disease, which can be observed in comparisons between tumors, across cell lines, and even within a single cancer cell population. Complex tumor genotyping has been used to predict metastatic risk(*136, 137*), and although these predictions are successful for some tumor subclasses(*138*), they do not identify the functional mediators of metastasis(*139*). Even in model cell lines, a subpopulation may develop increased metastatic potential under certain conditions that could inhibit metastasis for others. Rather than using biomarker(s) to predict metastatic potential(*122*), we tested a functional assay that allows the strength of cell adhesion to an underlying substrate to be observed ex vivo and in the appropriate context (i.e., with specific Mg^{2+} and Ca^{2+} concentrations to recapitulate tumor stroma)(*92, 93*). It has been observed that lower cation concentrations, akin to those found in tumor stroma, create labile adhesions(*119*) and lead to increased metastasis(*129*) and invasion(*130*). We demonstrated that 1) a systematic quantification of metastatic versus nonmetastatic cells can reveal different adhesive phenotypes, and 2) that these differences are driven by changes in FA dynamics resulting from stromal niche conditions.

Cell-matrix adhesion is an exceedingly dynamic process(*118*). To capture that complexity in a context-specific manner, a systematic quantification of adhesion under appropriate tumor and stromal cation conditions is required. Classic wash assays involve cells adhering for a short period of time (<1 h), with subsequent rinsing steps to remove unbound cells(*126*). The undefined shear in such assays makes it difficult to quantitatively assess cancer cell adhesion. Although centrifugation and micropipette assays can impose a single shear amount per culture, they typically indicate that the number of bound cancer cells(*16, 88, 127*) and the amount of activated integrin(*121*) is inversely proportional to the

metastatic potential of those cells. However, with the spinning-disk device, force is applied in a quantifiable and reproducible manner across the population(*123*). Furthermore, cation concentrations can also be probed directly since the cells remain in media(*124*). Under conditions that recapitulate estimated tumor Mg^{2+} and Ca^{2+} concentrations, e.g., 0.1–0.5 mM(*92, 93*), we found that several mammary cell lines had adhesion strengths be- tween 300 and 400 dynes/cm^2, regardless of the metastatic potential. At lower stromal cation concentrations, metastatic cells became significantly weaker and displayed adhesive heterogeneity, whether they originated from mammary (MDAMB231, SUM1315, and MDAMB468) or prostate (PC3) cancers. In contrast, nonmetastatic cell lines did not demonstrate significant adhesion strength heterogeneity. Moreover H-Ras transformation of a nonmetastatic cell line caused it to adopt adhesive heterogeneity only in Mg^{2+}- and Ca^{2+}-free conditions, indicating that independently of their genetic background, metastatic cell lines vary significantly in adhesion strength. Together with previous findings(*16, 88, 127*), these data establish an adhesion dependence on stromal-like conditions for a subset of metastatic cells.

The mechanism(s) behind adhesive heterogeneity and cation sensitivity in cells appears to be complex, whether the cells are selected by shear or not. Although metastatic behavior was previously linked to diminished integrin activation(*121*), we found no change in integrin expression or FAK phosphorylation that was independent of the buffer conditions used. However, blocking ion channels in meta- static mammary and prostate cancer cells artificially enhanced their adhesion in single-cell assays versus control cells(*88*), suggesting that cation effects are plausible. Indeed, we found that MCF10A adhesions were less cation sensitive than MDAMB231 adhesions, as their FA size and

number changed less after Mg^{2+} and Ca^{2+} removal in comparison with the MDAMB231 cells. Similarly, when MCF10A cell FA assembly was modulated by the addition of soluble RGD, the resulting changes in FAs reduced adhesion strength in a manner consistent with that observed for MDAMB231 cells. It should be noted that MCF10A cells were more sensitive to ligand type, although the sensitivity was always observed with adhesion strengths well above 100 dynes/cm^2. The sensitivity of MDAMB231 cells was observed at lower adhesion strengths and also induced heterogeneous adhesion, i.e., a shallow logarithmic slope. Under comparable matrix and cation conditions, MCF10A cells never exhibited heterogeneous adhesion. Together, these data suggest that assembly differences in low Mg^{2+} and Ca^{2+} conditions in the stroma could drive adhesion strength heterogeneity. As such, assembly changes have been equated to differences in turnover(*90*) and might be expected to create MDAMB231 cells with labile adhesions required for 3D protrusion and migration(*140*). This interpretation is consistent with metastatic and invasive behaviors observed in low Mg^{2+}- and Ca^{2+}-containing stroma(*129, 130*). We also showed that shear selection of the strongly adhering subpopulation of MDAMB231 cells (>45 dynes/cm^2) suppressed their migration on collagen gels and their ability to migrate through transwells, such that they resembled the less cation-sensitive, nonmetastatic cells. Although the origin of increased FA cation sensitivity remains unclear, the mechanism is not specific to mammary cells, since adhesion-selected PC3 prostate cancer cells also failed to migrate on substrates and/or in transwell assays as did their unselected counterparts. Together, these data suggest that there is a common heterogeneous adhesive signature in cell lines described as having metastatic potential, and importantly, within this population is a subset of weakly adherent, highly migratory cells.

2.5 Conclusions

Given the heterogeneity and plasticity observed in the adhesive phenotype and the inverse correlation between migration and strongly adherent subpopulations, the data presented here emphasize the importance of therapeutically targeting as many cancer cell states as possible, instead of focusing on the largest population or most aggressive phenotypes. These data also suggest that the adhesive state, when measured in the appropriate stromal cation concentrations, could serve as a unique biophysical marker for highly migratory behavior in metastatic cells generally.

2.6 Methods

2.6.1 Cell culture

Cells were cultured in their respective media as indicated in Supplementary Table 2.6 in the Supporting Material, using typical formulations from Life Technologies (Carlsbad, CA) and the American Type Culture Collection (ATCC, Manassas, VA). When applicable, cells were selectively cultured with RGD peptides (Sigma, St. Louis, MO). All cells were cultured at 37C in a humidified incubator containing 5% CO2. Unless otherwise noted, cell culture products were purchased from Life Technologies. All cells were obtained from the ATCC cell bank and verified to be mycoplasma free. Cells were also authenticated by the ATCC based on morphology, growth curve analysis, and isoenzyme analysis, and were passaged for <6 months after resuscitation.

2.6.2 Cell adhesion-strength assay

Glass coverslips (25 mm, Fisher Scientific, St. Louis, MO) were sonicated in ethanol and pure water before incubation with 10 mg/mL human fibronectin (isolated from serum(*141*)) for 60 min at room temperature. All adhesion-strength assays were performed on fibronectin-coated coverslips unless otherwise noted, and 20 mg/mL type I collagen (rat tail; BD Biosciences, Franklin Lakes, NJ) was used. Under regular conditions, cells were allowed to attach for 24 h at 37C and 5% CO_2 using cation-containing media. The coverslips were then mounted on a custom-built spinning-disk de- vice and dipped into temperature-controlled spinning buffer (37C)(*124*). Phosphate-buffered saline (PBS; without magnesium and calcium or with 0.5 mM $MgCl_2$ and 1 mM $CaCl_2$ (Cellgro, Manassas, VA)) was used as the spinning buffer. All spinning buffers contained 4.5 mg/mL dextrose. Once immersed in the spinning buffer, the coverslips were spun for 5 min at defined angular velocities and then the culture was continued or the cells were fixed with 3.7% formaldehyde immediately after spinning.

To select for strongly attaching cells, the center of the coverslips was covered with Parafilm that had been circularly cut with a crafting punch (The Punch Bunch, Temple, TX) and removed before shear application to ensure that all cells were subjected to a minimum shear. After 5 min of shear application, cells were allowed to recover in cell culture media for 1–2 h. The remaining cells were then trypsinized and re-plated on regular petri dish plastic. Control cells were treated likewise but without application of shear (i.e., 0 rpm).

2.6.3 Quantification of adhesion strength

Shear stress, t, by radial fluid motion over the surface of the coverslip was calculated(*123, 135*) such that:

$$\tau = \frac{4}{5} r \sqrt{\rho \mu \omega^3},$$

where r is the radial position from the center of the disk, ρ is the buffer density, μ is the buffer viscosity, and ω is the rotational speed. To obtain quantitative information about the adhesion strength, whole 25 mm coverslips were imaged at 10X magnification on a Nikon (Melville, NY) Ti-S microscope (~1000 individual images stitched together with Metamorph 7.6 soft- ware and custom macros) and analyzed using a custom-written MATLAB (The MathWorks, Natick, MA) program. In brief, in this approach, the user defines the outer circle of the coverslip from a stitched overview image and the software then finds the position of each nucleus relative to the center of the coverslip. Cell densities, as a function of radial position and subsequently shear, are stored and combined with other measurements, e.g., those obtained at different RPMs. A sigmoidal decay fit is used to quantify values of adhesion strength and the logarithmic slope, i.e., the fit parameter in the sigmoid for curve steepness.

2.6.4 Migration assays

For two-dimensional migration experiments, tissue-culture-treated 12- and 24-well plates were coated with soluble rat-tail type I collagen in acetic acid (BD Biosciences) to achieve a coverage of 20 mg/cm^2 and incubated at room temperature for 1 h. For two-dimensional migration, collagen matrices at 1.2 and 2.4 mg/mL concentrations were prepared as described elsewhere(*140*). In brief, collagen was mixed with ice-cold PBS and 1 M NaOH was then added to normalize the pH to 7.0. Cells were imaged with a Nikon Eclipse Ti-S microscope equipped with a motorized temperature- and CO2-controlled stage. Cells were imaged at 10$ in bright field at multiple positions every 15 min for up to

48 h. Most of the migration data were analyzed by Time Lapse Analyzer, a freely available MATLAB program for cell migration analysis(*142*). Samples that could not be analyzed by the automated software (due to gel swelling and/or z-migration of the cells) were tracked manually with ImageJ (NIH, Bethesda, MD).

Additional migration experiments utilized six-well plates with transwell permeable supports (8 mm polycarbonate membrane; Corning, Corning, NY) that were seeded with 100,000 cells. After cells adhered to the permeable support, media was added to the whole well. Cells were allowed to migrate through the membrane for 24 h and then fixed and stained for nuclei (DAPI). Cells that successfully migrated through the membrane were counted on the bottom of the permeable support (ceiling). Additionally, cells that dropped off the support and adhered to the bottom of the six-well plate were also counted (bottom).

2.6.5 Immunofluorescence staining and focal adhesion analysis

Fixed cells were incubated for 10 min with 0.25% Triton X-100 followed by 1% albumin overnight at $4^{o}C$ for blocking. Primary paxillin antibody (1:2000; ab32084, Abcam, Cambridge, UK) was applied for 2 h at room temperature. Then, a secondary Alexa Fluor 488-conjugated antibody (1:2000, Invitrogen, Carlsbad, CA) was applied for 1 h or rhodamine phalloidin (1:2000, Invitrogen) and Hoechst 33342 (3.2 mM, Invitrogen) were applied for 30 min at room temperature. The cells were subsequently mounted with Fluoromount-G (Southern Biotech, Birmingham, AL). All buffers contained 1 mM $MgCl_2$. The samples were imaged with the use of a CARV II confocal (BD Biosciences) Nikon Eclipse Ti-S microscope equipped with a motorized, programmable stage using a Cool-Snap HQ camera (Photometrics, Tucson, AZ) and controlled by Metamorph 7.6 (Molecular Devices, Sunnyvale, CA). A custom-written MATLAB program was used to quantify cell

area and FA number and size(*124*). All FA metrics were computed across the entire cell to avoid regional biases.

2.6.6 Western blotting

Cell lysates were collected in mRIPA buffer (50 mM HEPES (pH 7.5), 150 mM NaCl, 1.5 mM $MgCl_2$, 1% Triton X-100, 1% Na-DOC, and 0.1% SDS) with 1 mM EGTA, 1 mM Na_3VO_4, 10 mM $Na_4P_2O_7$, and 1 mM phenylmethanesulfonylfluoride for Western blots. Samples were run in 10% SDS-PAGE gels at 150 V until proteins were separated and then transferred onto polyvinylidene fluoride membranes (Bio-Rad, Hercules, CA) to be run at 100 V for 1 h 15 min in the transfer apparatus (Bio- Rad). The membranes were washed in buffer A (25 mM Tris-HCl, 150 mM NaCl, and 0.1% Tween-20) 5% bovine serum albumin overnight at $4^{o}C$ and then incubated for 2 h with the following antibodies: FA kinase (FAK; ab40794) at 1/500 and pFAK anti-phospho Y397 (ab4803) at 1/500 (both from Abcam), and glyceraldehyde 3-phosphate dehydrogenase (GAPDH; MAB374) at 1/250 (Millipore, Billerica, MA). After three 10-min washes with buffer A, secondary goat anti-rabbit horseradish peroxidase (Bio-Rad) and anti-mouse horseradish peroxidase (Abcam) were used for incubation for 30 min. Immunoblots were visualized using enhanced chemiluminescence reagent (Thermo Fisher, Waltham, MA).

2.6.7 Fluorescence-activated cell sorting analysis

Cells were detached from fibronectin-treated coverslips by incubation for 5–10 min with PBS without cations at $37^{o}C$ and gentle pipetting. After re-suspension in flow-cytometry buffer (DPBS, 2.5% goat serum, 1 mM EDTA (pH 7.4)), the cells were incubated with fluorescent-conjugated antibodies against CD49e (phycoerythrin) and

CD51 (fluorescein isothiocyanate) (Biolegend, San Diego, CA) for 30 min on ice. Cells were analyzed using a FACScan flow cytometer (BD Biosciences).

2.6.8 Statistical analysis

Nonparametric Kruskal-Wallis analysis of variance tests were used for all statistical analyses unless indicated otherwise. All data in shear plots are expressed as mean 5 SD. All experiments were performed at least in biological triplicate, and analyses represent hundreds of cells per condition.

2.7 Supplementary Figures

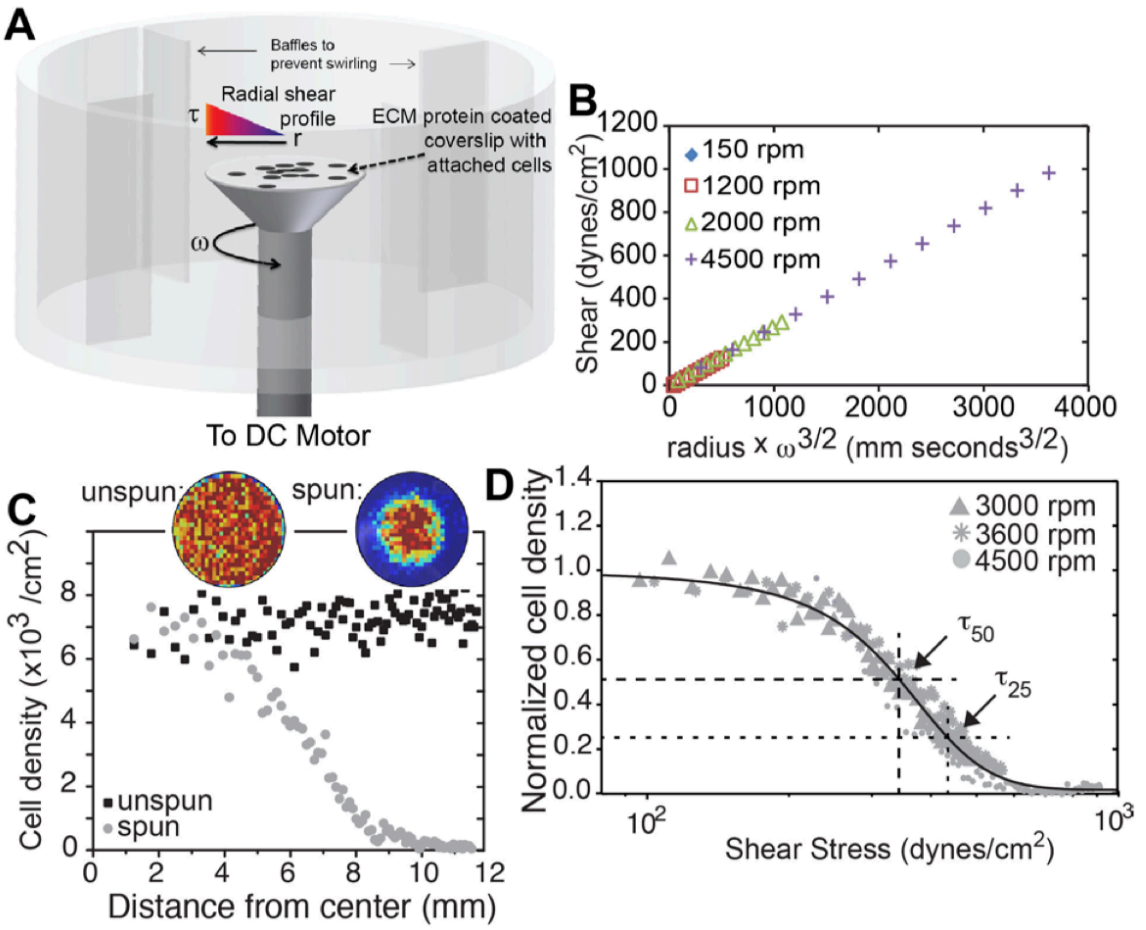

Supplementary Figure 2.1. Spinning Disc Assay Creates a Radially-dependent Shear Profile.
(A) The spinning disc device is illustrated with cells attached to an extracellular matrix protein-coated coverslip mounted and rotating on a spinning rod in buffer. The radially-dependent shear profile is highlighted showing that cells at the center only rotate in place while those at the edge move around at a high linear velocity. (B) The plot shows the relationship of radial position on the coverslip and angular velocity versus applied shear stress at a given point for the indicated velocities (in revolutions per minute; rpm). (C) Plot of the relationship between radial position and cell density. Inset images show heat maps of cell density. Warm (red) and cool (blue) colors indicate high and low densities, respectively. (D) Plot of cell density, normalized to the center of the coverslip, versus the applied shear. Data is plotted for the indicated velocities. τ25 and τ50, i.e. the shear to detach 25 and 50% of cells, respectively, are indicated in the plot and are 438 and 346 dynes/cm2, respectively.

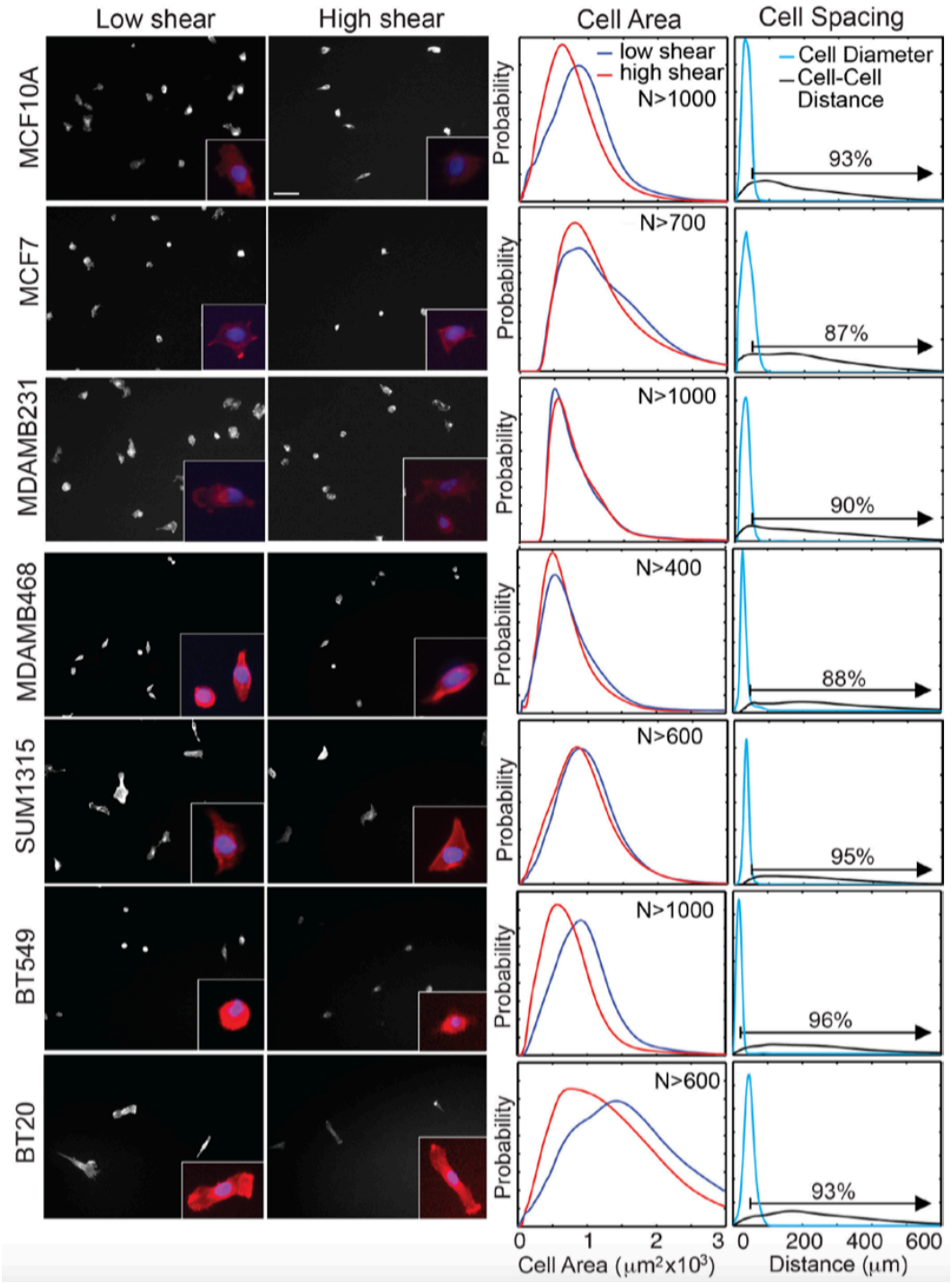

Supplementary Figure 2.2. Cell Morphology and Distribution are Independent of Mammary Epithelial Cell Line.

At the left are low magnification images of MCF10A, MCF7, MDAMB231, MDAMB468, SUM1315, BT549, and BT20 cells at low and high shear, which were stained with Rhodamine-Phalloidin. Inset images at higher magnification were also stained with DAPI. At right are plots of cell area (blue and red lines indicating high and low shear) and cell-to-cell spacing frequency for the indicated number of cells (N). Indicated within the plots is the percentage of cells spaced further apart than the average diameter of each cell line.

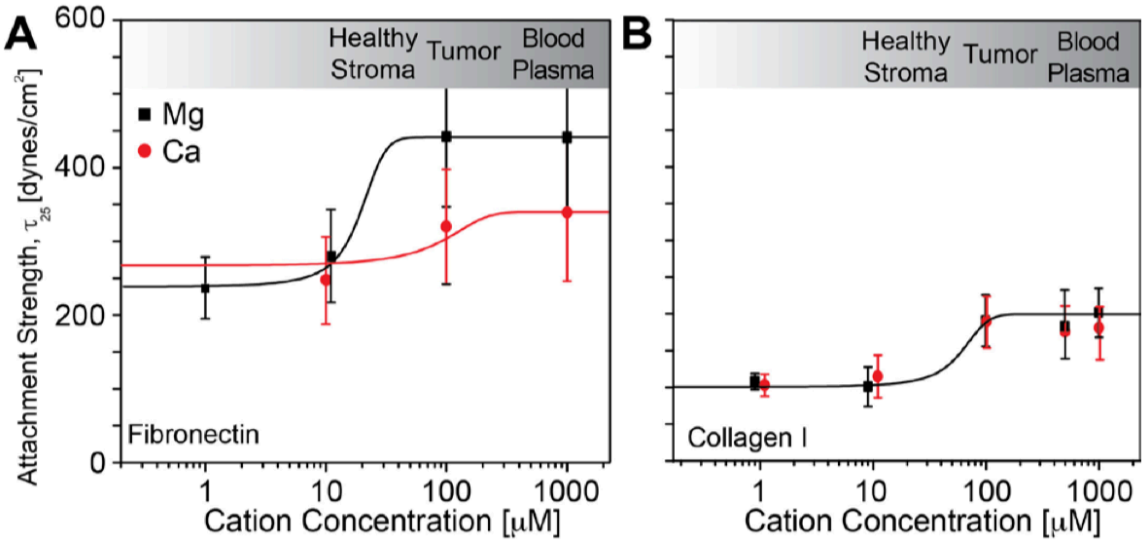

Supplementary Figure 2.3. MCF10A Cells Exhibit Cation-Sensitive Change in Attachment Strength. MCF10A, cells had homogeneous and strong attachment strengths, i.e. τ25, as plotted versus cation concentration for Mg2+ (black squares) and Ca2+ (red circles) for cells bound to (A) collagen type I-coated and (B) fibronectin-bound coverslips. Cation concentration range for the indicated tissue is provided for reference. A sigmoidal fit for each cation is shown in panel A but they are combined in panel B.

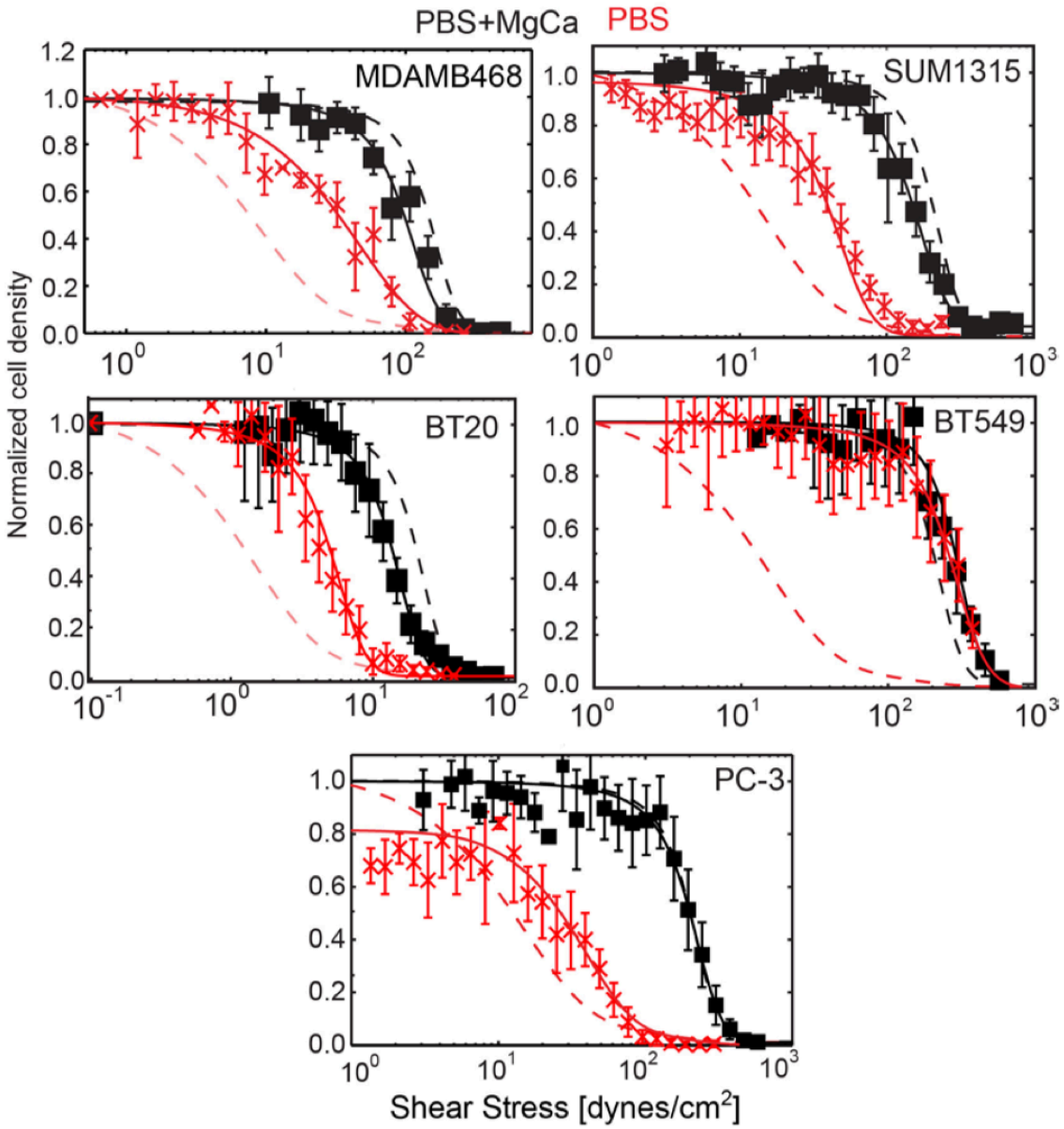

Supplementary Figure 2.4. Attachment Strength is Heterogeneous for Additional Mammary Epithelial Cells and Prostate Cancer Cells in Stromal-like Niche.
Normalized cell density is plotted versus shear for MDAMB468, SUM1315, BT20, BT549 and PC-3 cells. Cells were tested with (black) and without (red) media containing cations as defined in Figure 1. Dashed lines in each plot indicate the fits for MDAMB231 cells with (black) and without (red) media containing cations.

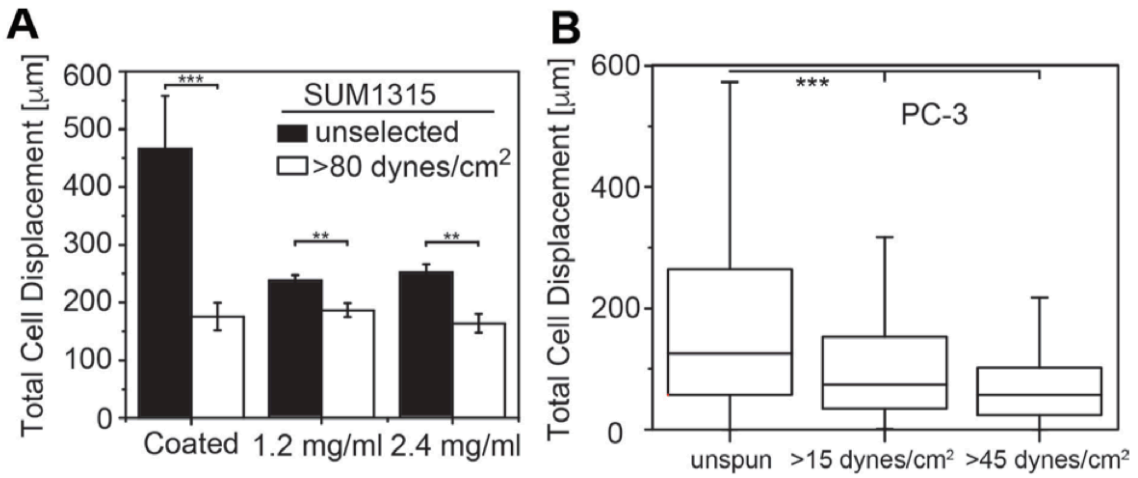

Supplementary Figure 2.5. Migration for SUM1315 and PC-3.
(A) SUM1315 cells, either unselected (blue) or selected with 80 dynes/cm2 (orange), plated onto collagen-coated, planar substrates (left) and 1.2 mg/ml (center) and 2.4 mg/ml (right) collagen hydrogels were plotted for the total distance migrated over 24 hours post-plating. Note that the migration of many unselected cells on planar surfaces exceeded the viewable window of the microscope over 24 hours, and thus these data represent a minimum distance traveled. (B) Total cell displacement over 24 hours for PC3 cells are plotted for the indicated shear stress selection conditions on collagen-coated substrates. PC-3 cell migration is more heterogeneous and thus displayed in a box and whisker plot **p <0.01, ***p < 0.001.

Supplementary Table 2.6. Media formulations for the indicated cell lines.

Cell Line	Base Media	Serum	Antibiotics	Others
MCF10A, MCF10A T	DMEM/ F12	5% HS	100 units/ml Penicillin, 100 µg/ml Streptomycin	0.5 µg/ml Hydrocortisone, 20 ng/ml hEGF, 10 µg/ml Insulin, 100 ng/ml Cholera toxin
MCF7	DMEM	10% FBS	100 units/ml Penicillin, 100 µg/ml Streptomycin	10 µg/ml Insulin
MDAMB231, MDAMB468, BT20	DMEM	10% FBS	100 units/ml Penicillin, 100 µg/ml Streptomycin	
SUM1315	DMEM/ F12	5% FBS	100 units/ml Penicillin, 100 µg/ml Streptomycin	5µg/ml hEGF, 5 µg/ml Insulin
BT549	DMEM	10% FBS	100 units/ml Penicillin, 100 µg/ml Streptomycin	1 µg/ml Insulin
PC3	F-12K	10% FBS	100 units/ml Penicillin, 100 µg/ml Streptomycin	

2.8 Acknowledgements

The authors thank Drs. Caroline Damsky and David Strom for antibodies obtained via the Developmental Studies Hybridoma Bank under the auspices of the National Institute of Child Health and Human Development, and maintained by the University of Iowa (Iowa City, IA). The authors also thank Dr. Philippe Gascard for a helpful review of the manuscript. The spinning-disk device was designed and manufactured by Jeremy Riley, Ryan Tam, Joe Shu, and the UC San Diego Campus Research Machine Shop.

This work was supported by grants from the National Institutes of Health (DP2OD006460 and U54CA143803-03 to A.J.E.), the Department of Defense (W81XWH-13-1-0133 to A.J.E.), and the National Science Foundation Graduate Research Fellowship Program (to A.B. and P.B.).

Chapter 2, in full, is a reprint of the material as it appears in Fuhrmann, A., Banisadr, A., Beri, P., Tlsty, T.D., and Engler, A.J. “Metastatic State of Cancer Cells may be indicated by Adhesion Strength.” *Biophys J*, 2017. 112(4): 736-745. The dissertation author was a corresponding author of this paper.

Chapter 3.

Cell adhesiveness serves as a biophysical marker for metastatic potential

3.1 Abstract

Tumors are heterogeneous and comprised of cells with different dissemination abilities. Despite significant effort, there is no universal biological marker that serves as a metric for metastatic potential of solid tumors. Common to disseminating cells from such tumors, however, is the need to modulate their adhesion as they detach from the tumor and migrate through stroma to intravasate. Adhesion strength is heterogeneous even amongst cancer cells within a given population, and using a parallel plate flow chamber, we separated and sorted these populations into weakly and strongly adherent groups; when cultured under stromal conditions, this adhesion phenotype was stable over multiple days, sorting cycles, and common across all epithelial tumor lines investigated. Weakly adherent cells displayed increased migration in both 2D and 3D migration assays; this was maintained for several days in culture. Subpopulations did not show differences in expression of proteins involved in the focal adhesion complex but did exhibit intrinsic focal adhesion assembly as well as contractile differences that resulted from differential expression of genes involved in microtubules, cytoskeleton linkages, and motor activity. In human breast tumors, expression of genes associated with the weakly adherent population resulted in worse progression-free and disease-free intervals. These data

suggest that adhesion strength could potentially serve as a stable marker for migration and metastatic potential within a given tumor population and that the fraction of weakly adherent cells present within a tumor could act as a physical marker for metastatic potential.

3.2 Introduction

The high mortality rate associated with cancer is due to metastasis from a primary tumor to a distal site(*143, 144*). Patient outcomes typically scale with rate of cell dissemination from the tumor, resulting in lower five-year survival rates for aggressive tumors such as invasive ductal carcinoma (*143*). However, determining cell dissemination rate from a tumor is difficult due to heterogeneity, *i.e.* cells in the same tumor have different propensities for forming secondary metastases (*117, 145, 146*). Furthermore, there are no universal biochemical markers that predict metastatic potential across solid tumors (*122, 145*); next generation assays that use these biomarkers typically only surveil cells post-intravasation.

Biophysical markers, such as cell deformability, are an emerging alternative to assess metastatic potential (*80, 84-87, 147*). Assays based on these metrics focus largely on characterizing the physical properties of already circulating cells rather than understanding how cancer cells physically interact with and adhere to the extracellular matrix (ECM) at the onset of invasion. Given that all cancer cells must interact with the ECM to initiate metastasis, understanding variations in these interactions can serve as an early indicator of metastatic ability. For optimal cell migration into adjacent parenchyma, cells must turnover their focal adhesions to move through the tissue effectively; extremely unstable or stable adhesion can arrest migration as the cell can never establish contractile

forces or unbind and retract rear portions of the cell (*120*). Thus, migration speed is a function of the strength of attachment and is maximized when migrating cells can cycle their adhesions (*120, 148*). Indeed, invasive cancer cells have more dynamic focal adhesions than their non-invasive counterparts (*90*), and decreased adhesion strength corresponds to increased metastatic potential (*121*). As a result, the adhesion of cancer cells to ECM proteins is becoming an accepted metric for metastatic potential (*16, 126*).

Many assays have been developed to demonstrate how adhesion differs in metastatic cells compared to their non-metastatic counterparts (*16, 88, 149, 150*). However, such assays are either low throughput or not quantitative. It is also difficult to assess adhesive heterogeneity within a single cancer line using these methods (*128*). We have previously demonstrated that metastatic breast cancer cells display lower cell-ECM adhesion strength than their non-metastatic counterparts using a spinning-disk shear assay (*91, 124*), especially when cells are exposed to an environment whose low cation concentration mirrors stroma (*151, 152*). We also observed an inherent heterogeneity in adhesion strength in multiple lineages including breast, prostate, and lung cancer cell lines (*91*). Given this information, we developed a parallel plate flow chamber to isolate distinct fractions of cells from a heterogeneous population. Cells were isolated by applying a uniform shear stress to the cell population in the presence of stromal concentrations of Mg and Ca cations (*151, 152*). Within a given tumor line, we observed significant adhesion heterogeneity and found that the more weakly adherent fraction displays increased migration in both 2D and 3D. This is due to the increased contractility and focal adhesion disassembly present in weakly adherent cells, resulting from transcriptomic expression differences in cytoskeletal components. Together, these data suggest that intrinsic

differences in adhesion strength of cells within a population can act as markers of intratumoral heterogeneity in metastatic potential and be exploited to biophysically fractionate subpopulations.

Figure 1

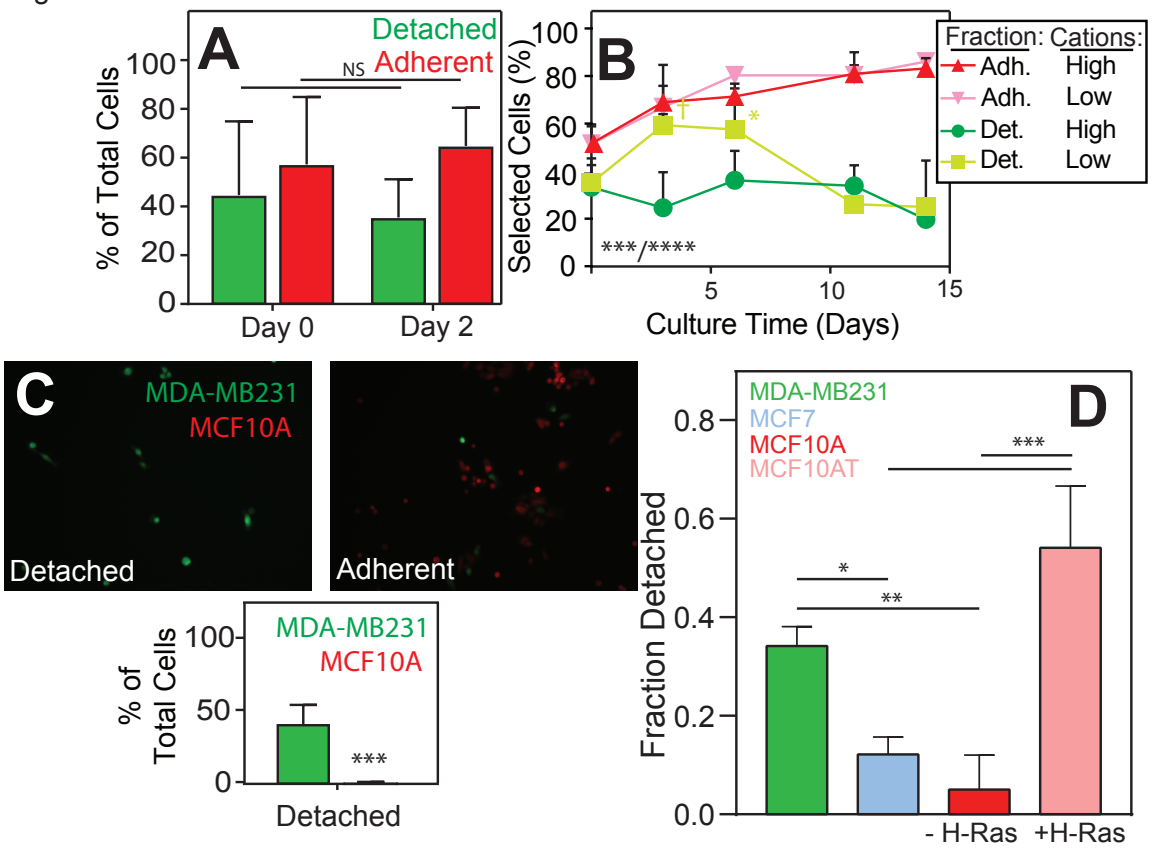

Figure 3.1. Low Cation PPFC Accurately and Precisely Sorts Cancer Cell Populations that are Stable Long-term.
(A) MDA-MB231 populations were sorted at day 0, remixed, and then resorted at day 2. Differences between weakly and strongly adherent populations were assessed by two-tailed unpaired t-test (n=3). (B) Adherent cells post-sort were cultured in high cations for 3, 6, 11, and 14 days and resorted. Cells that detached were cultured in high cations or low cations mirroring stroma prior to re-sorting. Differences between weakly and strongly adherent populations as a function of culture time and condition were assessed by two-way ANOVA with Tukey test for multiple comparisons (n=3). For time and condition, ANOVA showed ***$p<0.001$ and ****$p<0.0001$, respectively as indicated at the corner of the plot. Individual comparisons to their counterpart cation conditions are indicated in the plot with $^{\dagger}p<0.1$, and *$p<0.05$. (C) Images of cells from the flow-through (detached) and remaining on the plate (adherent) after exposure to shear along with quantification of the percentage of cells that detached relative to plated cells from each line. n=3. ***$p<0.001$ for two-tailed unpaired t-test between lines. (D) Plot showing the fraction of detached cells from MDA-MB231, MCF7, and MCF10A and their H-Ras transformed counterparts MCF10AT after exposure to 250 dynes/cm^2 of shear stress.

3.3 Results

3.3.1 Strongly and weakly adherent phenotypes are maintained post sort.

We fabricated a parallel plate flow chamber that exposes cells to discrete, uniform shear stresses in order to isolate fractions of cells based on adhesion strength and study those cells within a heterogeneous population (Figure S3.1). To ensure that the application of shear did not change the adhesive heterogeneity of the population, we isolated weakly and strongly adherent fractions of MDA-MB231 cells from a parental cell population by exposing the cell to a shear of 170 dynes/cm^2 and stratifying the populations depending on whether they were found in the flow-through or still attached to the device. After sorting, cells were cultured separately, re-mixed, seeded into the device, and subsequently sheared. We found no significant changes between the percent of weakly and strongly adherent cells when tracking cells between days 0 and 2 (Figure 3.1A), indicating that the parallel plate shear device assesses, but does not alter, the inherent adhesion heterogeneity of the population.

We next wanted to determine if the adhesion phenotype is stably maintained post-isolation. We isolated both fractions from MDA-MB231 cells, cultured them separately in either normal or reduced cation media, and then repeated the isolation on the separated fractions. We found that strongly adherent cells maintained their adherent phenotype 14 days post-isolation, regardless of culture conditions. Weakly adherent cells did not maintain their adhesion phenotype in normal culture media as cells reverted back to their distribution in the parental population; if the selection pressure of low stromal-like cation concentrations was maintained post-isolation, weakly adherent cells were enriched to >70% of the population 6 days post-isolation (Figure 3.1B).

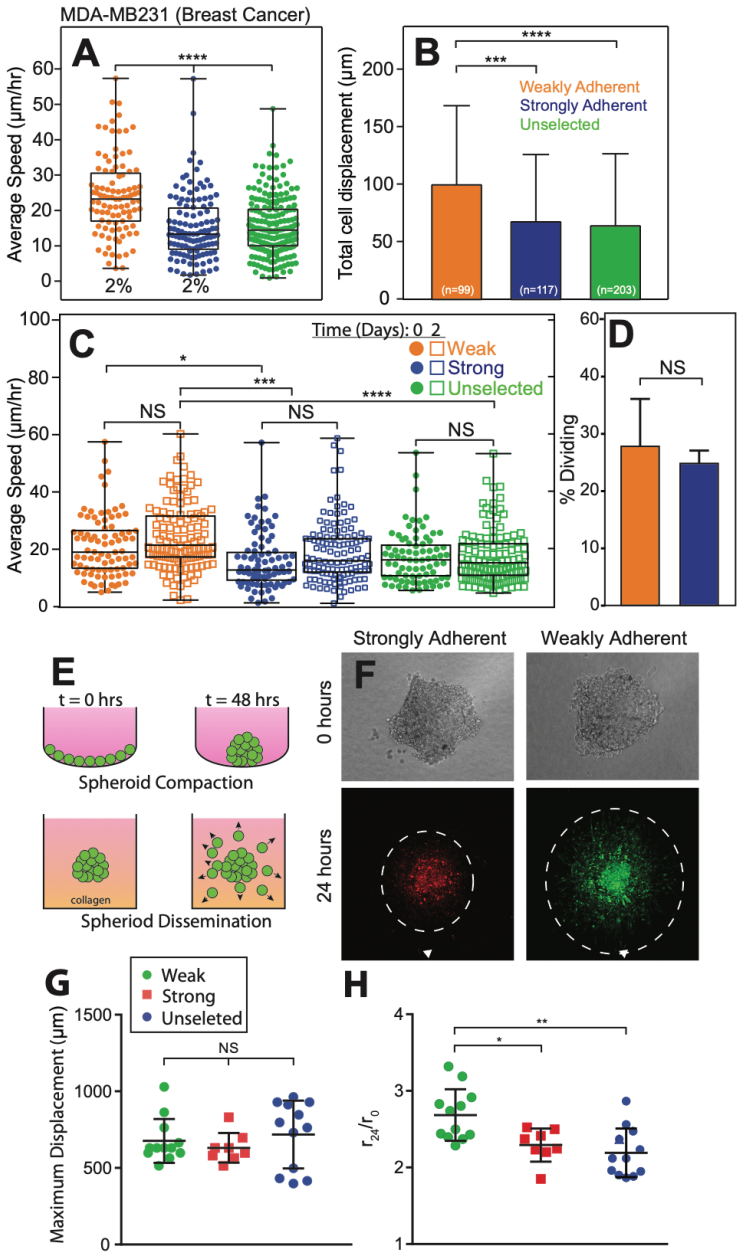

Figure 3.2. Sorted Populations of Single cells and Spheroids Exhibit and Sustain Different Migration Patterns.

(A) Average speed and (B) total displacement is plotted for MDA-MB231 cells sorted by the indicated shear stress and allowed to migrate on collagen gels for 24 hours. Percentages in panel A reflect the portion of each population that detaches or remains adherent at a given stress. n=3 biological replicates for the number of cells per condition inset in the bars in panel B. (C) Average speed was measured after initial isolation and after 2 days. n=3 biological replicates. (D) Plot showing the percentage of dividing cells on a collagen gel over 24 hours for cells selected by the indicated shear stress. n=3 biological replicates. (E) Schematic of tumor spheroid formation (top) and subsequent dissemination (bottom) in a collagen gel. (F) Brightfield images at the time of spheroid embedding in a collagen gel and fluorescent image 24 hours later. Dashed line indicates the average radius of disseminating cells. Plots of (G) maximum and (H) normalized average outward radial migration of cells selected by indicated shear (see Supplemental Figure 5 for radius measurements). One-way ANOVA with Tukey test for multiple comparisons was used to indicate significance where *p<0.05, **p<0.01, ***p<0.001, ***p<0.0001, and N.S. = not significant.

3.3.2 Parallel plate flow chamber can distinguish between weakly adherent and strongly adherent cell lines.

To test the ability of the flow chamber to select for cells known to have a weaker adhesion strength as a result their higher metastatic potential, MDA-MB231 (metastatic breast cancer line) and MCF10A (non-malignant breast cell line) cells were seeded in a 50:50 mixture and exposed to a shear stress that should detach the MDA-MB231 cells but not the MCF10A cells (170 dynes/cm^2 based on population adhesion assays (*91*)). The fraction of cells that detached contained 41.7% of the total number of MDA-MB231 cells, while only 0.7% of the total number of MCF10A cells were present in the detached fraction (Figure 3.1C), consistent with 10-fold higher adhesion strength of MCF10A vs. MDA-MB231 cells in the absence of cations (*91*) and suggesting that this assay could distinguish metastatic cells from non-cancerous cells.

In order to link quantitative adhesiveness to metastatic potential, we exposed four cell lines of varying metastatic potential (high metastatic capability: MDA-MB231; low metastatic capability: MCF7 and MCF10A; and H-Ras transformed: MCF10AT, which give rise to invasive carcinomas *in vivo (134)*) to 250 dynes/cm^2 of shear stress and counted the fraction of detached cells. As expected, cells with greater tumorigenic and/or metastatic potential had significantly greater detachment at the same shear stress in comparison to cells with lower tumorigenic and/or metastatic potential (Figure 3.1D).

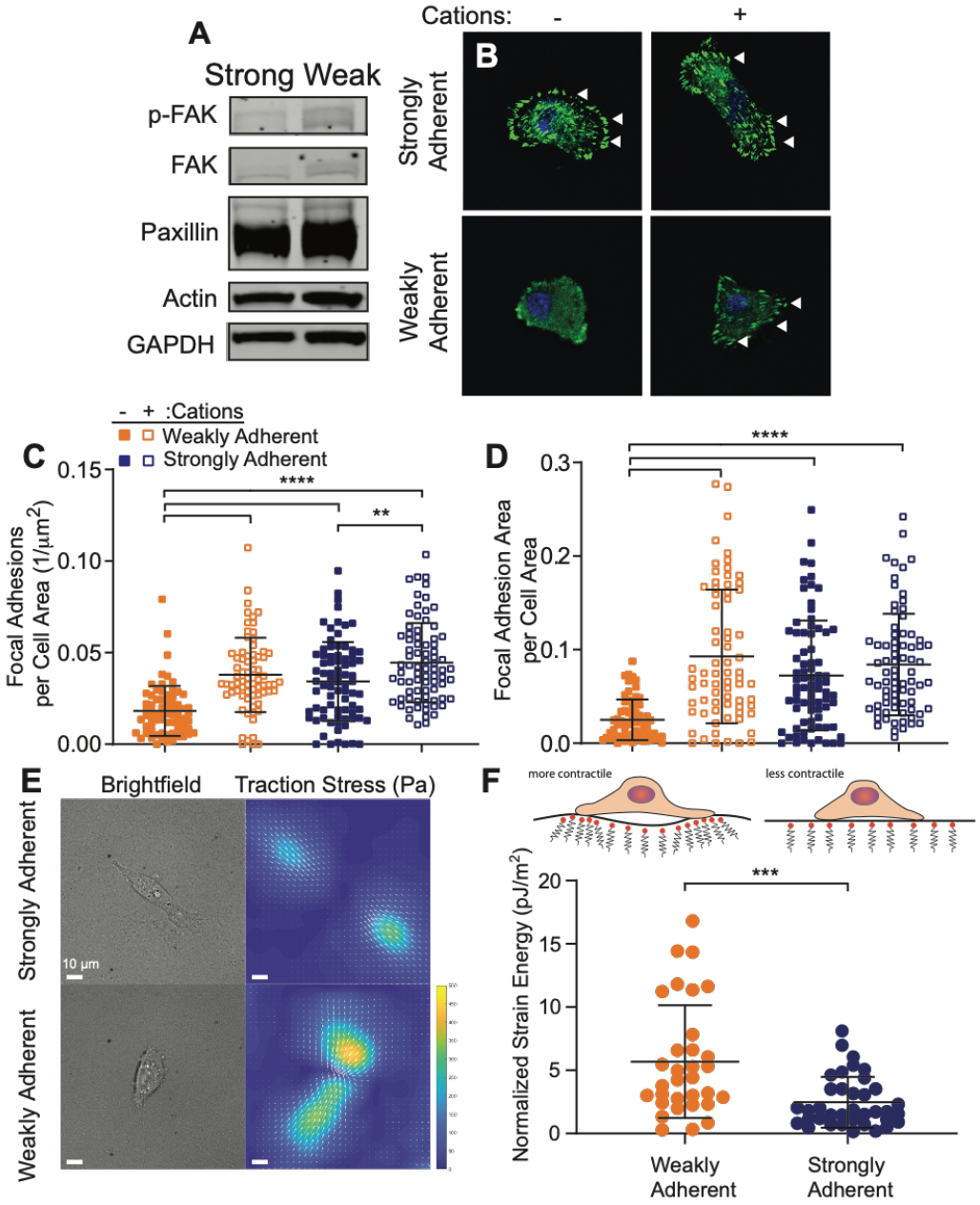

Figure 3.3. Adherent Phenotypes within a Cancer Line Result from Intrinsic Adhesion Stability and Contractility Differences.

(A) Comparison of the expression of common focal adhesion proteins in strongly adherent (SA) and weakly adherent (WA) cells. (B) Representative images of focal adhesions in SA and WA cells when subjected to with or without cation conditions. (C) Focal adhesion density and (D) total area per cell area is plotted for the indicated sorting and cation conditions. n=3 biological replicates and >50 cells/condition. One-way ANOVA, with Tukey's multiple comparison test was performed for the indicated comparisons with **p<0.01, ***p<0.001, and ****p<0.0001. (E) Brightfield and traction stress plots for cells from the indicated shear conditions. Scale bar is 10 microns. (F) Plot of normalized strain energy for WA and SA cells. n=3 biological replicates and >30 cells/condition. A two-tailed unpaired t-test between lines indicated **p<0.01, ***p<0.001, and ****p<0.0001.

3.3.3 Weakly adherent cells display greater migratory propensity than strongly adherent cells.

To assess migration differences in adhesion sorted populations, we isolated the ~2% most weakly and most strongly adherent cells of the MDA-MB231 population using 28 dynes/cm^2 and 510 dynes/cm^2, respectively and seeded them onto type-I collagen gels. Over 24 hours post-plating, we found that weakly adherent cells displayed significantly higher average speed than the strongly adherent or unselected (non-sheared) cells (Figure 3.2A). Weakly adherent cells also displayed increased total cell displacement than the strongly adherent or unselected cells (Figure 3.2B, Figure S3.2). Since the adhesion phenotype appears stable, we investigated if migratory differences were stable. Weakly and strongly adherent cells along with unselected population were imaged post selection, and then re-imaged 2 days later. No significant differences for any population were observed post selection or later while the weakly adherent fraction maintained its increased migratory propensity (Figure 3.2C). The two populations did not exhibit differential proliferation during migration assessments (Figure 3.2D), suggesting that higher migration speeds for weakly adherent cells were not the result of proliferation differences. In addition to sorting a metastatic population, we further demonstrated sorting fidelity by directly comparing the ~2% most weakly and strongly adherent of MCF10A and isogenic H-Ras transformed MCF10AT cells. Post-sort on collagen gels, we observed that the weakly adherent fraction of MCF10AT cells had increased migration speed and displacement relative to its strongly adherent counterpart, while MCF10A cell fractions did not show differences (Figure S3.3). These data suggest that heterogeneity in migratory phenotype as

a result of selection by adhesion strength is only present in more aggressive cells with increased tumorigenic capability.

Migration can often be affected by matrix properties, and so we sought to determine if migration differences are intrinsic and therefore persist regardless of environmental changes that could reduce substrate adhesion. Weakly and strongly adherent MDA-MB231 cells were plated on polyacrylamide gels of low (300 Pa) and high stiffness (1.8 kPa) and migration observed for 24 hours. Weakly adherent cells were more migratory that the strongly adherent cells independent of substrate stiffness. However, average speed scaled with substrate stiffness gel for both cell fractions, which indicates that both fractions are mechanically sensitive (Figure S3.4). These results indicate that there are cell intrinsic differences independent of environmental changes that could potentially alter substrate adhesion.

Assays thus far show behaviors in 2D rather than 3D, so we next assessed the outward migration from spheroids containing weakly adherent, strongly adherent or unselected cells (Figure 3.2E, F). There was no significant difference in maximum cell displacement (Figure 3.2G), but the leading edge of weakly adherent cells, i.e. the distance at which the signal is higher than background (Figure S3.5), migrated further than strongly adherent and unselected cells, indicated by the significantly higher ratio of final radius to initial radius (Figure 3.2F, H). Consistent with 2D migration, these 3D spheroid data bolster the concept that the fraction of tumor cells with the weakest adhesion most represents those with the highest metastatic potential.

All the cells examined thus far are mammary epithelial, so we next explored whether cells from other epithelial tumors would exhibit the same cation dependent

adhesion sorting and migration phenotype. Weakly and strongly adherent NCI-H1299 metastatic lung cancer cells were isolated and their migration analyzed. As with the metastatic mammary tumor line, weakly adherent metastatic lung cancer cells were more migratory than their strongly adherent counterparts (Figure S3.6), suggesting that this behavior may be universal across epithelial tumors.

3.3.4 Weakly adherent cells have more labile focal adhesions and are more contractile.

Migratory differences between weakly and strongly adherent cells did not result from expression differences in focal adhesion proteins, *e.g.* pFAK, FAK, paxillin, or actin (Figure 3.3A). However, we previously found that metastatic cells preferentially disassemble their focal adhesions relative to non-metastatic cells when exposed to low cation conditions (*91*). Consistent with this, we found that the strongly adherent subpopulation of MDA-MB231 cells did not fully disassemble focal adhesions after removal of cations. Conversely, weakly adherent cells disassembled their focal adhesions in the absence of cations on fibronectin (Figure 3.3B-D) or on type I collagen-coated substrates (Figure S3.7). These data suggest that weak adhesion could be driven by differential sensitivity to cations and could therefore enhance migration. Similarly, cancer cells that exhibit increased contractility are also more migratory than their less contractile counterparts (*8, 153*). To ascertain if adhesive state is coupled with contractility differences, traction force microscopy was performed on cells post-sort. Weakly adherent cells were significantly more contractile than their strongly adherent counterparts (Figure 3.3E-F), suggesting that weakly adherent cells represent a more aggressive fraction of the population.

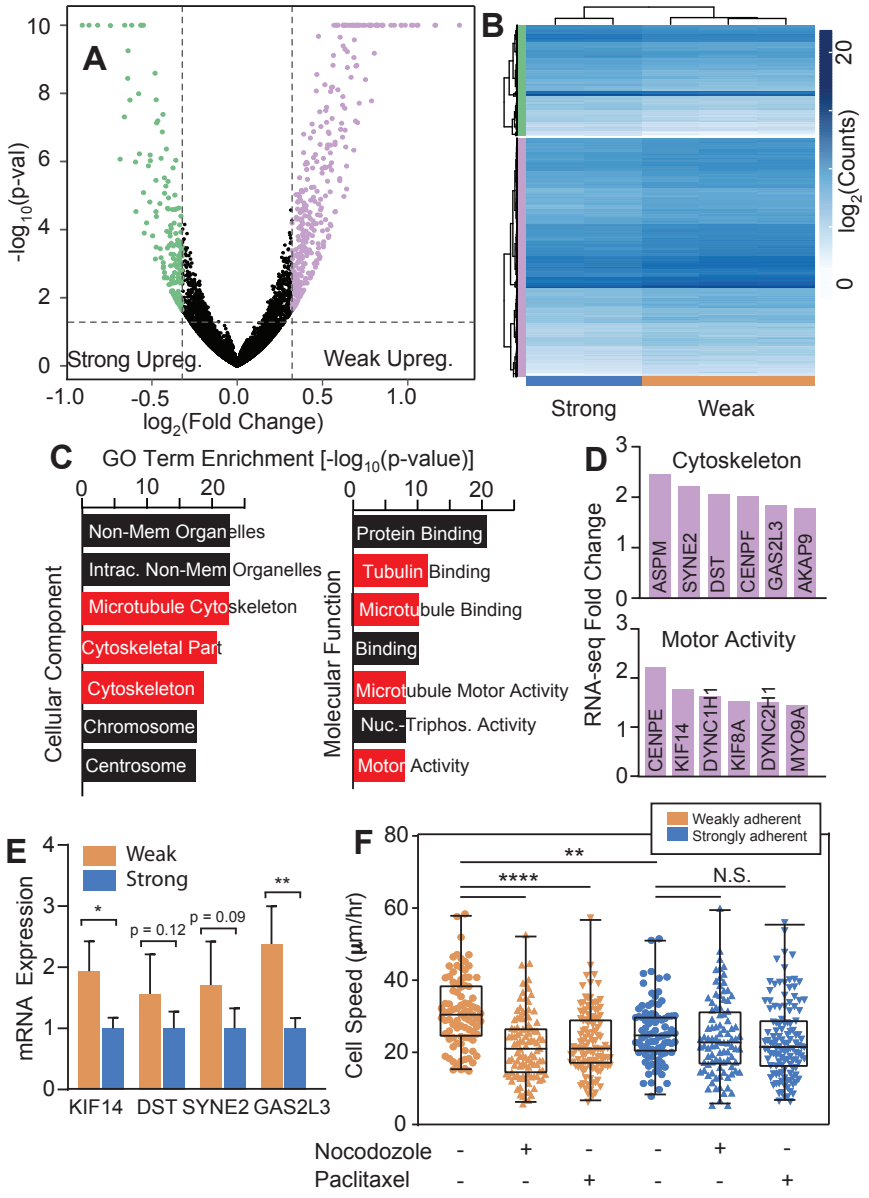

Figure 3.4. RNA-seq Identifies Intrinsic Patterns that Indicate Structural rather than Expression Changes in Adhesion.

(A) Differences in gene expression between weakly and strongly adherent MDA-MB231 cells. (B) Hierarchical clustering of differentially expressed genes between weakly and strongly adherent cells. Vertical bars indicate clustering of genes that are upregulated in strongly adherent cells and weakly adherent cells. (C) Genes ontology terms that are upregulated in the weakly adherent subpopulation. Cytoskeletal and microtubule gene ontology terms, as well as proteins that bind to these components, were significantly upregulated in weakly adherent cells. (D) Expressions of genes upregulated in Cytoskeleton and Motor Activity, normalized to strongly adherent subpopulation. (E) Validation of RNA seq gene expression differences via qPCR for select genes. *p<0.05 and **p<0.01 for two-tailed unpaired t-test between weakly and strongly adherent cells. (F) Average speed of weakly and strongly adherent cells when treated with microtubule-targeting drugs. At identical concentrations of nocodazole (0.2 ug/mL) and paclitaxel (0.5 ug/mL), weakly adherent cells displayed a significant decrease in migration speed, while the strongly adherent cells demonstrated no change. One-way ANOVA, with Tukey's multiple comparison test was performed for the indicated comparisons with **p<0.01, ***p<0.001, and ****p<0.0001.

3.3.5 Intrinsic transcriptional variation in microtubule proteins contributes to increased migration of weakly adherent cells.

Given that populations sorted at the less restrictive 170 dynes/cm^2 still remain stable with over 1-2 weeks in culture, and cells sorted at the more restrictive 28 dynes/cm^2 show cell intrinsic migration differences independent of environmental changes that are stable for days in culture, we next interrogated transcriptional differences underlying weakly and strongly adherent phenotypes sorted at 28 dynes/cm^2. Stability appears in part because individual populations do not out compete each other, i.e. cell proliferation rates appear similar (Figure S3.8). With stable sorting and expansion, we sought to assess differences through post-sort RNA sequencing. Analyses revealed 500 differentially expressed genes between the sub-populations (Figure 3.4A); replicates clustered by sub-population when comparing differentially expressed genes (Figure 3.4B). Analysis of genes upregulated in weakly adherent cells demonstrated significant enrichment of gene ontology terms involved in microtubule and cytoskeletal organization and binding (Figure 3.4C). Genes in these categories with the most significant expression differences are involved in cytoskeletal components, specifically microtubule-associated proteins. For example, GAS2L3 has been implicated in linking microtubules and actin and results in increased focal adhesion turnover and migration; SYNE2 is also essential for nuclear-cytoskeletal mechano-transduction in invasion and cell contraction (*154-156*). Components linking the cytoskeleton to the nuclear or plasma membranes were also implicated, *e.g.* AKAP9, which regulates microtubule movement and is highly expressed in highly metastatic cells (*157, 158*) (Figure 3.4D). There was also significant enrichment in the expression of motor proteins, specifically those involved in vesicular transport along

microtubules (KIF14, DYNC1H1) as well as in cytoskeletal contraction (MYO9A) (Figure 3.4C-D). KIF14, in particular, is a potent oncogene that is highly expressed in several cancers, particularly breast cancer, and is linked to improved invasiveness and dynamically changing focal adhesions (*159, 160*). Changes detected through RNA sequencing were validated by qPCR, which confirmed increased expression in weakly adherent cells (Figure 3.4E).

To functionally confirm a link between the upregulated microtubule components in the weakly adherent cells and their subsequent increased migration, we exposed both weakly and strongly adherent cells to either nocodazole or paclitaxel to dissemble or cap microtubules, respectively. When tracking migration, untreated weakly adherent cells had increased average speed compared to untreated strongly adherent cells. However when treated with either microtubule-targeting drugs, the weakly adherent cells exhibited a significant decrease in average speed, while the strongly adherent cells were unaffected (Figure 3.4F). These data suggest that inhibiting the microtubule cytoskeleton preferentially impacts the weakly adherent fraction and points to microtubule-affecting agents as potent therapeutic targets.

Finally, we investigated whether differentially expressed genes linked to the highlighted microtubule, cytoskeletal, and microtubule-binding protein ontology terms played a role in human cancer progression. We narrowed the list of genes down to those linked to our highlighted GO terms in Figure 4C, resulting in 100 genes (Supplemental Table 3.10). Using this gene set, we then analyzed The Cancer Genome Atlas (TCGA) breast cancer dataset and restricted our analysis to triple-negative breast cancer (TNBC) patients with tumors that ranged from Stage I to III. We then compared patients that had

gene expression scores that aligned with the strongly and weakly adherent cells. We observed that patients with gene expression profiles similar to the weakly adherent cells had decreased progression-free intervals (Figure 3.5A) and disease-free intervals (Figure 3.5B) compared to patients with gene expression profiles similar to the strongly adherent cells. These data suggest that increased expression of genes associated with microtubule and microtubule-binding proteins, as present in the weakly adherent fraction, could define an "adhesive signature" that results in an increase in metastatic potential and promotes human breast tumor progression.

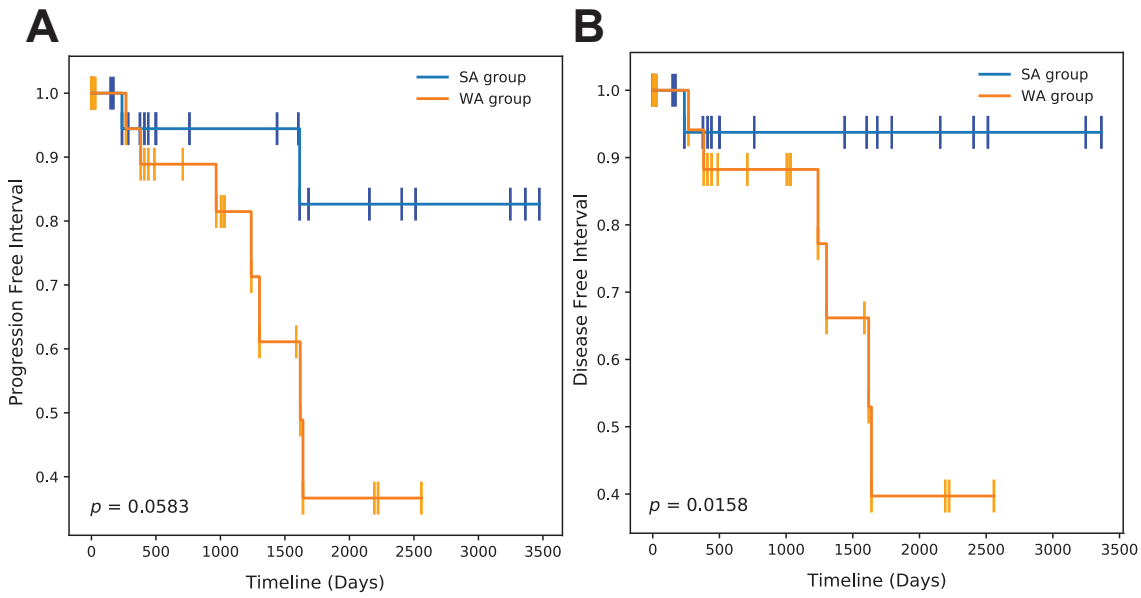

Figure 3.5. Expression of microtubule-associated genes resembling weakly adherent fraction predicts poor outcome in breast cancer patients.
(A) Progression-free interval and (B) disease-free interval of TNBC patients with Stage I-III tumors. Patients with gene expression that resembled strongly adherent and weakly adherent cells were compared. Genes were restricted to those associated with highlighted GO terms in Figure 4C, resulting in a cohort of 100 genes.

3.4 Discussion

Due to the highly heterogeneous nature of tumor cells, both within a given tumor as well as across tumors from different patients, it is difficult to assess tumor aggressiveness and the likelihood of metastasis. In addition, there are no universal

biochemical markers that can be utilized to determine metastatic potential. The emergence of biophysical markers is a new approach to identifying the most aggressive subpopulations of the tumor population. Common cell-ECM interactions of early dissemination of cancer cells of different tumor origins and subsequent ECM deformation reflect the importance of identifying biophysical markers as metrics for metastatic potential (*143, 144*). To accomplish this, we utilized a parallel plate flow chamber to study the correlation between decreased adhesion strength of cells to ECM proteins and their subsequent metastatic potential. In conjunction with our previous studies (*91*), we showed that metastatic cancer cells are significantly less adherent than their non-metastatic counterparts. This is demonstrated by the ability to select for MDA-MB231 cells over MCF10A cells from a mixed population. We also found that weak adhesion can serve as a potential marker for metastatic potential, which was demonstrated by the greater percent detachments of MDA-MB231 and MCF10AT cells in comparison to MCF7 and MCF10A cells at the same shear stress.

This study also identified heterogeneity in adhesion strength of cells within a metastatic cancer cell population, especially under stromal-like cation conditions, which may be linked to heterogeneity in metastatic potential of cells within a tumor population and/or circulating tumor cells. This notion is supported by our observations that weakly adherent MDA-MB231 cells exhibited increased migration in comparison to their strongly adherent counterparts. These differences in migration exist in both 2D and 3D environments, which indicates that the weakly adherent subpopulation represents the cells that are more likely to leave the primary tumor and establish secondary metastases (*161-163*). The stability of this increased migratory propensity for multiple days post-sorting

further demonstrates the intrinsic nature of this phenotype. In addition, recapitulating this phenotype in metastatic lung cancer cells suggests that adhesion strength is broadly involved in the more migratory subpopulations within tumors from multiple epithelial backgrounds.

The ability to select this more migratory subpopulation of the cell line stems from differences in focal adhesion disassembly between the weakly adherent and strongly adherent cells. Faster focal adhesion disassembly of weakly adherent cells is consistent with previous findings that link quicker focal adhesion disassembly to more migratory cell lines (*90, 164, 165*). In addition, weakly adherent cells are more contractile than their strongly adherent counterparts, where increased contractility has also been linked to increased migration and more aggressive cancers (*8, 153*). Differences in migration, focal adhesion assembly, and contractility can be tied to inherent transcriptomic differences between weakly and strongly adherent cells; genes linked to the cytoskeleton, specifically to microtubules, as well as motor proteins involved in vesicular transport and contraction showed significant differential expression. When we compared human breast cancer patients with gene expression signatures that resembled the weakly and strongly adherent cells for our genes of interest, we observed decreased progression-free and disease-free intervals, implying that tumors resembling the weakly adherent fraction are more aggressive. Several standard cancer therapy drugs (nocodazole, taxols, etc.) target microtubules in order to reduce the growth and spread of aggressive tumors, indicating that differences in microtubules and the cytoskeleton could explain the heterogeneity of tumor cell populations. We confirmed these findings by treating weakly adherent cells to nocodazole and paclitaxel and found that their migration speed reduced to that of the

strongly adherent cells, whose speed was unaffected by both drugs. Therefore, targeting the cytoskeleton is potentially an important method of restricting the motility of highly aggressive subpopulations early in tumor development and suppressing the migratory populations that we observe (*166*).

This study reveals a strategy to identify distinct subpopulations via shear separation that can be implemented to study the dissemination of cells from a variety of epithelial cancers. Comparing weakly adherent cell populations across multiple metastatic cell lines of various tumor origins could enable the identification of similarities amongst the most aggressive subpopulation in an effort to identify more universal targeted treatments. Lastly, this shear assay can be adapted to study diseases with a similar adhesion component, highlighting the versatility of this technique.

3.5 Methods

3.5.1 Cell Culture

MDA-MB231 and MCF7 cells were cultured in DMEM, 10% Fetal Bovine Serum (FBS), and 1% antibiotic/antimycotic; MCF10A and MCF10AT cells were cultured in DMEM/F-12, 5% horse serum, 1% penicillin/streptomycin (Pen/Strep), 0.5 µg/ml Hydrocortisone, 20 ng/ml hEGF, 10 µg/ml Insulin, 100 ng/ml Cholera toxin; NCI-H1299 cells were cultured in RPMI, 10% FBS, and 1% Pen/Strep. Products were purchased from Life Technologies. All cells were obtained from ATCC (authenticated by morphology, growth curve, and isoenzyme analysis), verified mycoplasma free via PCR, and were not used beyond passage 10.

3.5.2 Parallel plate shear assay

Glass plates (Brain Research Laboratories, Waban MA) were sonicated in 70% ethanol and water. Plates were coated with fibronectin at 2 μg/cm^2 for 60 minutes and then blocked with 5% bovine serum albumin for 2 hours at 37ºC. Plates are then seeded with cells at a density of 5000 cells/cm^2 and incubated overnight. Components of the parallel plate shear assay (polysulfone base plate, 38 μm thick silicone gasket (SMI), polypropylene luer fixtures (Cole Parmer), 1/8-inch inner diameter tubing (Fisher Scientific)) were assembled and the glass plate was clamped to the base plate containing the inlet and outlet. The inlet tubing was connected to a syringe pump. Shear stress, τ, was calculated using the following equation:

$$\tau = \frac{6\mu Q}{wh^2} \quad (1)$$

Where μ is viscosity of the fluid, Q is volumetric flow rate, w is the width of the chamber, and h is the height of the chamber.

3.5.3 Isolating weakly (WA) and strongly (SA) adherent cells

To test adhesion stability of WA and SA fractions of the population, we first determined an intermediate shear stress to detach roughly 40% of cells (~170 dynes/cm^2 for MDA-MB231 cells). Phosphate-buffered saline without magnesium and calcium and with 4.5 g/L of dextrose was used to shear cells. Cells were subjected to the intermediate shear stress for 3 minutes to isolate WA cells in the flow-through, which was collected at the outlet. 0.25% Trypsin-EDTA was added to the device to isolate SA cells. Once cells detached, media was pushed through the device to neutralize the trypsin and remove the SA cells. Both populations were then seeded.

To perform the adhesion stability re-mixed population assay, WA and SA cells were isolated at day 0, cultured separately for 24 hours, re-mixed and seeded onto a plate overnight, then re-isolated at 48 hours after the initial isolation.

To isolate the weakest and strongest 2% of the MDA-MB231 cell population for migration assays, the seeded plate was subjected to a low shear stress (28 dynes/cm^2) for 3 minutes to isolate WA cells in the flow through from the outlet. The shear stress was then increased to a high shear stress (510 dynes/cm^2) for 2 minutes to eliminate intermediate cell fractions. The remaining steps to isolate SA cells are listed above. The weakest MCF10A and MCF10AT cells were isolated using 170 and 130 dynes/cm^2 of shear stress respectively; the strongest were isolated using 1275 and 595 dynes/cm^2 respectively.

3.5.4 Co-culture assay

MDA-MB231 and MCF10A cells were trypsinized and resuspended in 25 μM of CellTracker fluorescent probes (Molecular Probes, Life Technologies) in serum-free DMEM: MDA-MB231 in Green CMFDA and MCF10A in Orange CMRA. Cell-dye solutions were incubated at room temperature (RT) for 20 minutes. The cells were then centrifuged and resuspended in MDA-MB231 media. Cells were mixed 50:50 and seeded such that the final seeding density was 5000 cells/cm^2, then incubated overnight.

Upon isolation of WA and SA cells, both fractions were seeded, incubated overnight, then fixed the following day with 3.7% formaldehyde for 10 minutes. Cells were imaged using a Nikon Eclipse Ti-S microscope at 10X magnification with FITC and Texas Red and counted by color.

3.5.5 Measuring percent detachment versus metastatic capability

MDA-MB231, MCF7, MCF10A, and MCF10AT cells were subjected to 250 dynes/cm^2 of shear. The detached and adherent fractions were isolated as described and counted to calculate the fraction of cells detached.

3.5.6 Immunofluorescence staining and focal adhesion (FA) analysis

Fixed cells were incubated for 10 minutes at RT with CellMask Deep Red plasma membrane stain (1:1000, Thermo Fisher) in 1 mM $MgCl_2$ solution, followed by incubation for 1 hour at RT with blocking solution of 10% goat serum, 0.1% saponin, 1% bovine serum albumin, 0.03 M glycine in 1 mM $MgCl_2$ solution. Primary paxillin antibody (1:250; ab32084, Abcam) in blocking solution was applied overnight at 4°C. Then, a secondary Alexa Fluor 488-conjugated antibody (1:2000, Invitrogen) in blocking solution was applied for 1 hour at RT, followed by Hoechst 33342 (1:2000, Invitrogen) in DI water for 10 min at RT. The cells were subsequently mounted with Fluoromount-G (Southern Biotech). The samples were imaged with a Zeiss LSM 780 confocal microscope (Zeiss) with a 63x oil-immersion objective. A custom-written ImageJ program was used to quantify cell area and FA number and size. All FA metrics were computed across the entire cell to avoid regional biases.

3.5.7 Traction Force Microscopy (TFM)

Cell tractions were measured as described and calculated using a custom Matlab routine (*167*). 2% v/v of 0.2 μm diameter 580/605 FluoSpheres microspheres (Invitrogen) were added to the prepolymer solution, comprised of 5% acrylamide, 0.06% bis-acrylamide, 1% ammonium persulfate (Fisher), and 0.1% v/v of N,N,N',N'-Tetramethylethylenediamine (VWR International). Gels were prepared in 12 well glass

bottom plates (Cellvis), which were precleaned in a UV/Ozone cleaner (ProCleaner™ Plus, Bioforce Nanosciences) and methacrylated to ensure binding of the gel. Collagen was bound to the surface by adding 0.2 mg/ml sulfo-SANPAH and activating with UV light (wavelength 350 nm) for 10 minutes followed by incubation with 0.15 mg/ml type I collagen. Isolated cells were seeded at ~15,000 cells/cm^2 on the gels and allowed to adhere for 3 hrs. Brightfield images were taken of each cell prior to obtaining microsphere displacements at 60x. Bead reference positions were then re-obtained after removing the cells with a 10% v/v Triton X solution for 10 minutes. Strain energy was determined from the traction stress map and normalized to cell area.

3.5.8 Western blotting

Weakly and strongly adherent cells were isolated and plated in fibronectin-coated 12-well plates for 3 hours. Cells were lysed with mRIPA supplemented with phosphatase and protease inhibitors as described (*168*). Protein concentration was measured using a BCA assay. 5 μg protein was mixed with 50 mM DTT, Loading Buffer, and mRIPA, heated at 95ºC for 5 minutes, and loaded into a Bolt 4-12% Bis-Tris Plus gel (Invitrogen) and then run with MES running buffer for 30 min at 200 V. Protein was transferred to a nitrocellulose membrane using an iBlot Cell Transfer Stack (Invitrogen). Membrane was blocked with 5% SeaBlock for 1 hour at RT then incubated overnight at 4ºC with anti-paxillin (Abcam, ab32084), anti-pFAK (Y397) (Abcam, ab81298), anti-FAK (Origene, TA506161), anti-Actin (Abcam, ab8226), and anti-GAPDH (Abcam, ab8245). The membrane was then incubated for 2 hours at RT with AlexaFluor 680 donkey anti-mouse (Life Technologies, A32788) and AlexaFluor 790 donkey anti-rabbit (Life Technologies,

A11374) antibodies. The membrane was imaged using a Li-Cor Odyssey CLx and analyzed using Image Studio Lite (Li-Cor).

3.5.9 2D migration assays on collagen gels

2.4 mg/mL Type I collagen gels were prepared by mixing collagen (Corning) with PBS, DI water, and 1 M NaOH and adjusted to pH 7.0. Gels were added to a 12-well plates and cured at 37ºC for 30 minutes. The weakest and strongest 2% of the cell population were seeded onto the gels and incubated overnight. The cells were imaged with a Nikon Eclipse Ti-S microscope equipped with a temperature- and CO_2-controlled stage. Cells were imaged at 10X in brightfield every 15 minutes for 24 hours. The migration data was analyzed via Fiji. The positions were normalized to the starting point and analyzed via a custom MATLAB script to compute instantaneous speed and cell displacement. Cells that divided or did not remain in the frame for 24 hours were not tracked. Cells that interacted with other cells for more than 2 hours were not tracked, as cell-cell interactions artificially slowed cell speed. For MDA-MB231 cell migration under drug treatment, cells were treated with either 0.2 μg/mL nocodazole (Cayman Chemical) or 0.5 μg/mL paclitaxel (LC Laboratories). Cells were imaged the following day for 24 hours and tracked as stated above.

3.5.10 2D migration assays on polyacrylamide gels of varying stiffness

Polyacrylamide gels of low and high stiffness were prepared as described in the TFM methods section, without fluorescent microbeads. The high stiffness prepolymer solution has an identical composition to the gels used for TFM, while the low stiffness prepolymer solution consists of 3% acrylamide and 0.06% bis-acrylamide with all other

components identical to the high stiffness gel. Cells were isolated, seeded, and tracked as described.

3.5.11 Preparing spheroids of MDA-MB231 cells

The weakest and strongest 2% of the MDA-MB231 cell population and unselected cells were isolated and seeded in a 12-well plate overnight. Cells were trypsinized and resuspended in 25 μM CellTracker fluorescent probes (Molecular Probes, Life Technologies) as described above. Cells were then centrifuged and resuspended in a solution of 0.25% Methocult in culture media. 2,500 cells (either WA or SA) were added to wells in a 96-well Corning Ultra-Low Attachment Spheroid Microplate (Corning) then incubated for 48 hours.

3.5.12 3D migration assay in collagen gels

Collagen gels were prepared as described above. Spheroids were embedded in a collagen gel solution and added to a 24-well plate. Media was added to the top of the gel, and a time 0 image was captured at 10X magnification with brightfield to obtain initial radius. Embedded spheroids were incubated for 24 hours, after which they were fixed with 3.7% formaldehyde in solution A for 20 minutes. Spheroids were imaged with a Zeiss LSM 780 Confocal Microscope at 10X magnification with the FITC and Texas Red channel. Z-stack images were acquired at 30 μm intervals from the bottom to the top of the spheroid. Maximum intensity projection images were generated and input into a custom Python script to analyze invasive index of spheroid and maximum displacement of cells in the spheroid. Invasive index is defined as:

$$I = \frac{r_{final}}{r_{initial}} \tag{2}$$

Where $r_{initial}$ is the radius at time t = 0 hours of the spheroid and r_{final} is the radius at time t = 24 hours.

3.5.13 RNA Sequencing

RNA from WA and SA cells was purified using Qiagen RNeasy Mini Kit (Qiagen, 74104). RNA quality was assessed using TapeStation (Agilent), RNA libraries were prepared using the Illumina TruSeq Stranded RNA, High Throughput Library Prep Kit and sequenced using the Illumina HiSeq 4000 system to generate 50 bp single-end reads. Data was analyzed by Rosalind (https://rosalind.onramp.bio/), with a HyperScale architecture developed by OnRamp BioInformatics, Inc. (San Diego, CA). Reads were trimmed using cutadapt (*169*). Quality scores were assessed using FastQC (*170*). Reads were aligned to the Homo sapiens genome build hg19 using STAR (*171*). Individual sample reads were quantified using HTseq (*172*) and normalized via Relative Log Expression (RLE) using DESeq2 R library (*173*). Read Distribution percentages, heatmaps, and sample plots were generated as part of the QC step using RSeQC (*174*). DEseq2 was also used to calculate fold changes and p-values. Clustering for the differentially expressed gene heatmap was done using the Partitioning Around Medoids method with the fpc R library (*175*). Functional enrichment analysis of pathways, gene ontology, domain structure and other ontologies was performed using HOMER (*176*). Enrichment was calculated relative to a set of background genes relevant for the experiment.

3.5.14 Quantitative PCR

RNA from WA and SA cells was purified using Qiagen RNeasy Mini Kit and reverse transcribed using SuperScript III Reverse Transcriptase (ThermoFisher Scientific,

18080093). Quantitative PCR was performed (45 cycles, 95°C for 15 seconds followed by 60°C for 1 min) using a 7900HT Fast Real-Time PCR System (Thermo Scientific, 4329001) with the primers listed (Supplemental Table S1), and iQ SYBR Green Supermix (Bio-Rad Laboratories, 1708880). Target genes were normalized to GAPDH and mRNA quantity was calculated based on a standard curve generated from a fibronectin plasmid.

3.5.15 TCGA Dataset Analysis

The TCGA raw data were downloaded from NIH NCI GDC Data portal directly. Corresponding clinical metadata were obtained from a previous publication (*177*). Only the breast cancer (BRCA) patients with reported negative histological staining for the three markers (Her2, ER, PR) and American Joint Committee on Cancer (AJCC) pathology stages below stage IV were included in our analysis cohort. Patient data were analyzed to determine correlation between gene expression corresponding to weakly adherent or strongly adherent phenotypes and 5-year survival. Patient data were analyzed by normalizing patient gene expression to z-transformed scores with respect to the differentially expressed genes between the weakly adherent and strongly adherent sub-populations. The z-scores were then summed for every patient, and z-score sum-based quantiles were mapped to Strongly Adherent (SA) and Weakly Adherent (WA) categories based on mean gene expression levels. The Kaplan-Meier method was used to create survival plots comparing the 20% of individuals with the lowest score to the 20% with the highest score. The log-rank test was used to determine significance of survival differences between groups. Survival analyses use the Lifelines python library (https://lifelines.readthedocs.io/en/latest/). Relevant scripts for the analysis of TCGA data

are available at: https://github.com/kec162ucsd/Tumor-Heterogeneity-Adhesion-Strength/

3.5.16 Statistics

2D migration assays, 3D spheroid migration assays, and focal adhesion disassembly plots were analyzed using a one-way ANOVA with Tukey test for multiple comparisons. Adhesion stability re-mixed population assay was analyzed with a two-way ANOVA, with Sidak multiple comparison test. All other comparisons were performed using two-tailed unpaired t-test unless otherwise indicated. For all analyses, *$p<0.05$, **$p<0.01$, ***$p<0.001$, ****$p<0.0001$. Data expressed as box-and-whisker plots show all points with the whisker ends corresponding to minimum and maximum values. All other values are expressed as mean +/- standard deviation. Statistical analyses were performed using Prism software.

3.5.17 Data availability

Data generated in this study was deposited to NCBI under GEO GSE135515. We do not impose any restrictions on data availability.

3.6 Supplementary Figures

Figure S1

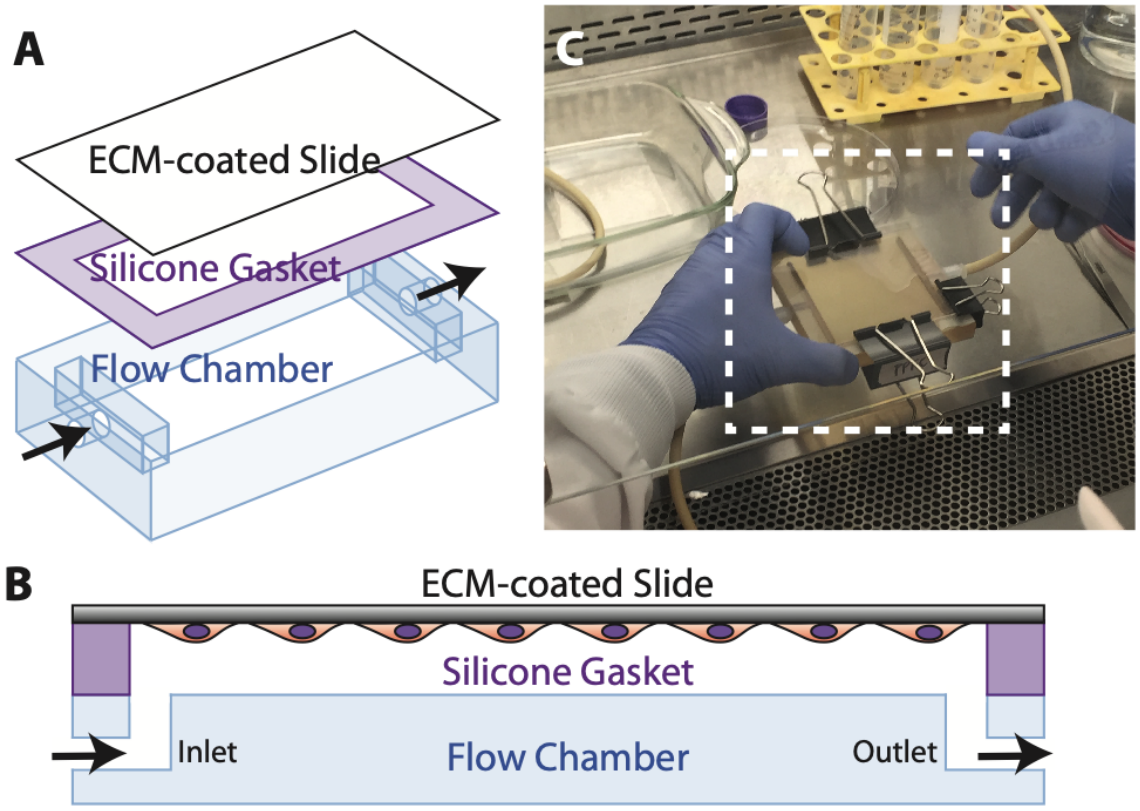

Supplementary Figure 3.1. PPFC Assembly and Use.
(A) Exploded parts diagram of the flow chamber. Arrows indicate fluid direction. (B) Assembled cross-section schematic of the flow chamber with cell locations shown and fluid flow indicated. (C) Image of assembled flow chamber (dashed lines).

Figure S2

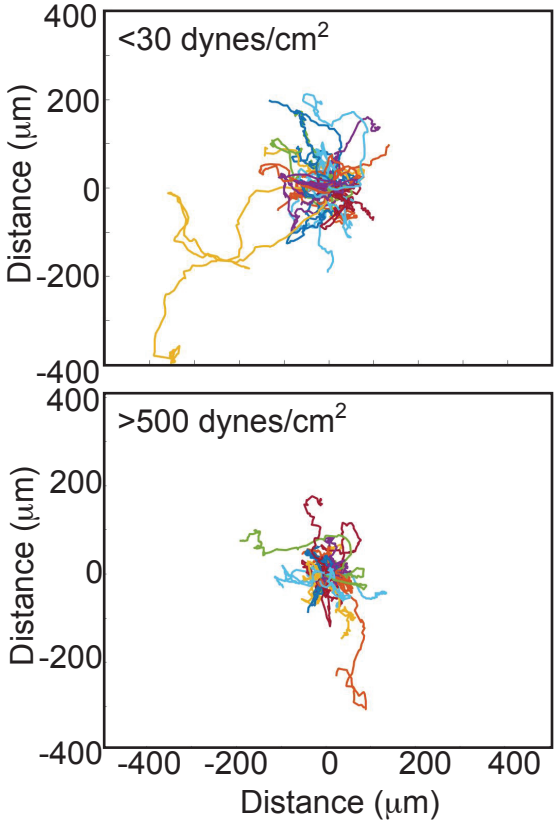

Supplementary Figure 3.2. Rose Plots of Post-Sort Cells.
Rose plots of MDA-MB231 cells (each colored differently to visualize their paths) selected at <30 or >500 dynes/cm2. n=3 biological replicates and 250 cells/condition shown.

Figure S3

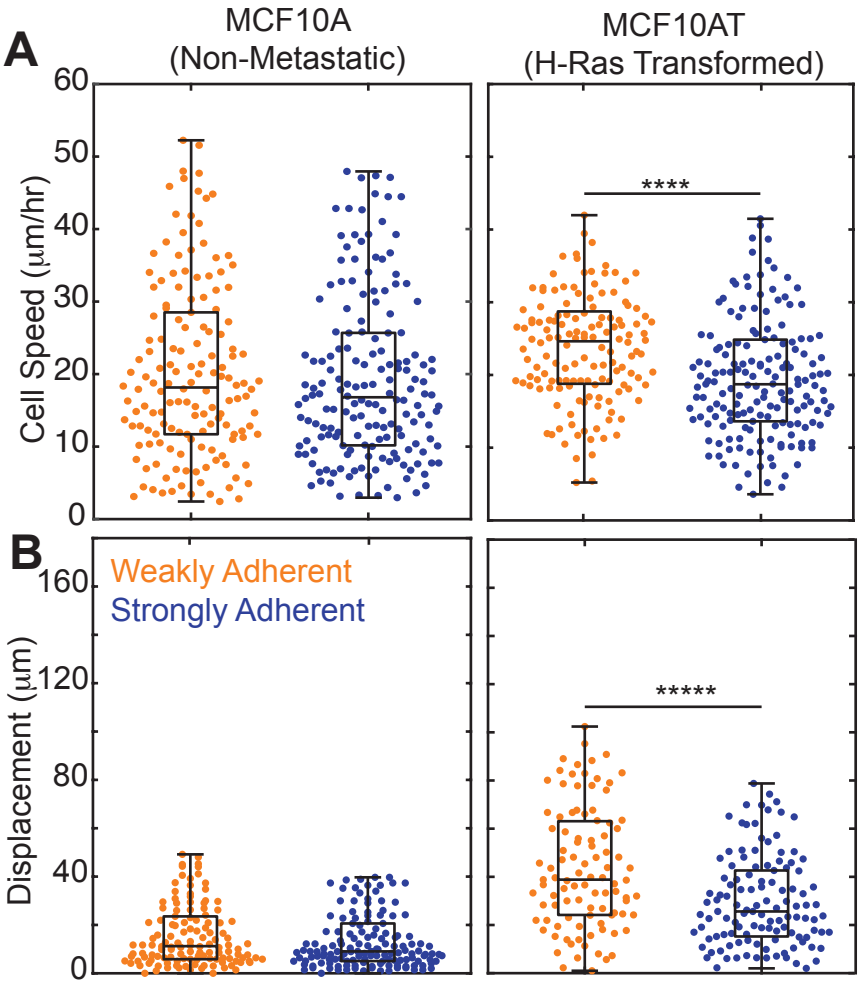

Supplementary Figure 3.3. Migratory Differences in Isogenic MCF10A and MCF10AT Cells.
(A) Average speed and (B) total displacement of MCF10A and MCF10AT cells sorted for the indicated fractions and allowed to migrate on collagen gels for 8 hours. n=3 biological replicates and >90 cells/condition. A two-tailed unpaired t-test between lines indicated ****$p<0.0001$ and *****$p<0.00001$.

Figure S4

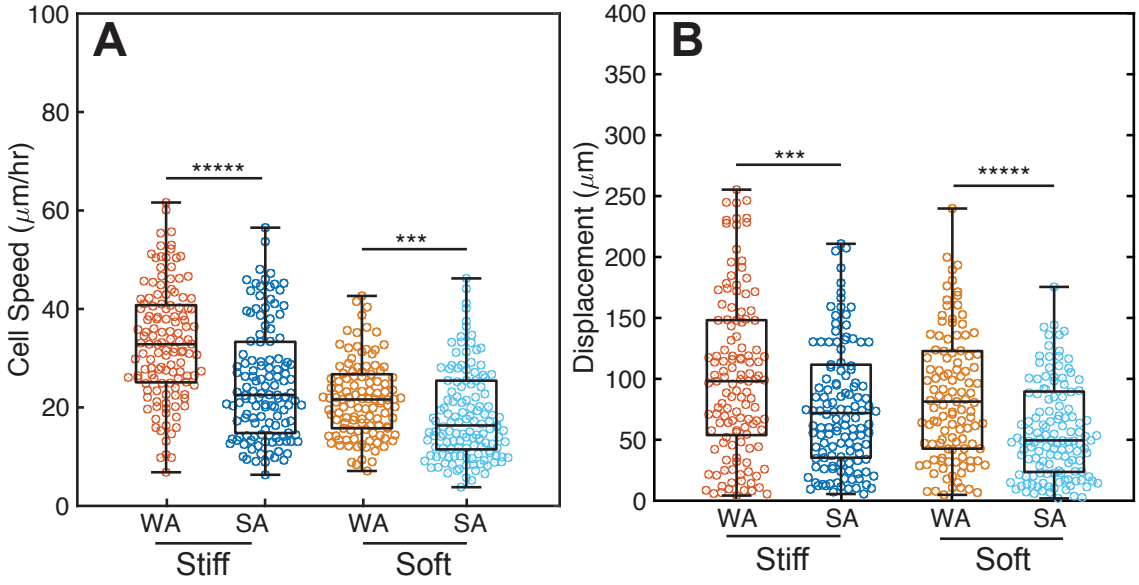

Supplementary Figure 3.4. Sorted Populations of MDA-MB231 Cells Display Migratory Differences Under Different Substrate Stiffnesses.
(A) Average speed and (B) total displacement over 24 hours is plotted for MDA-MB231 weakly and strongly adherent cells on soft (300 Pa) and stiff (1.8 kPa) collagen-coated polyacrylamide gels. A two-tailed unpaired t-test between lines indicated ****p<0.0001 and *****p<0.00001.

Figure S5

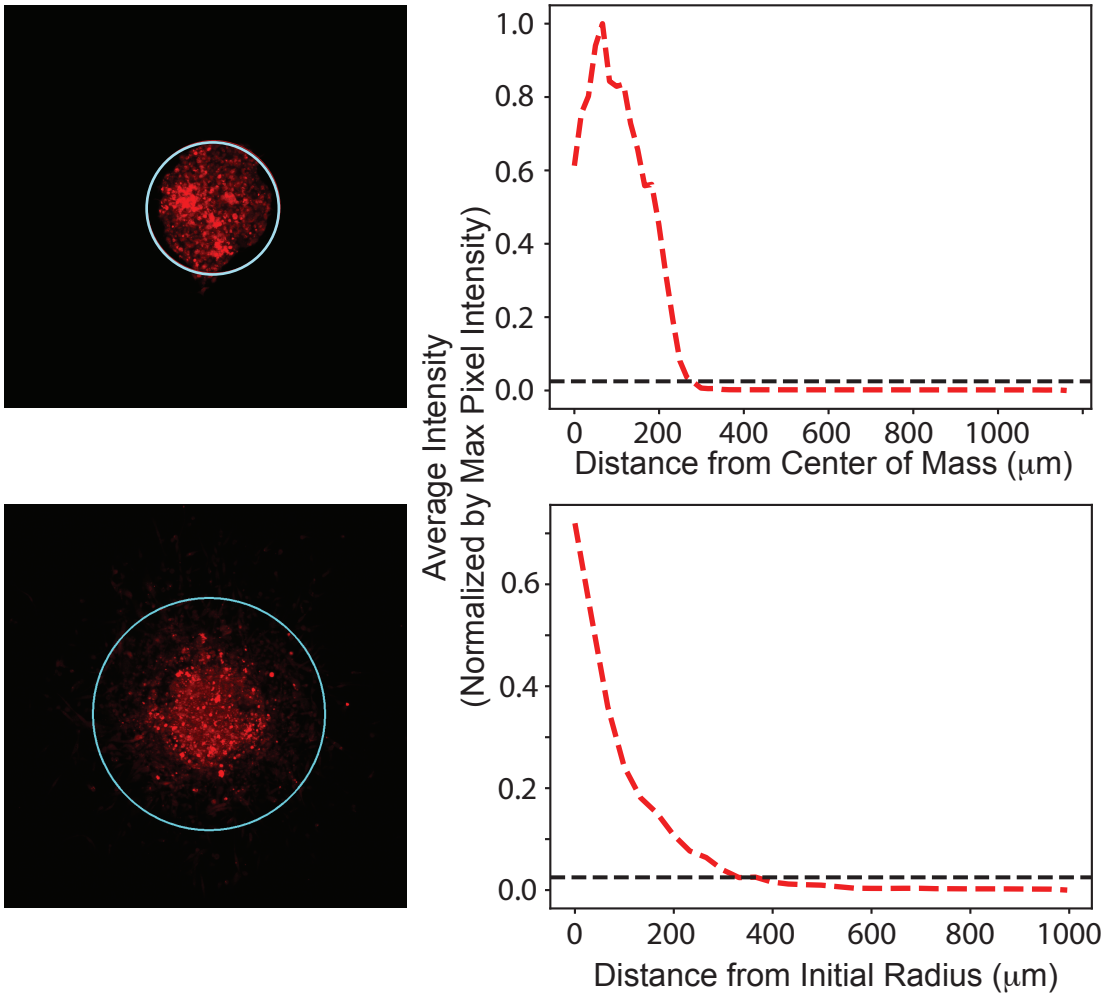

Supplementary Figure 3.5. Determining Spheroid Invasive Front
To automate the detection process for the leading edge of a spheroid embedded in and migrating through a collage gel, image analysis code was written to identify the radial intensity of the spheroid and surround matrix. When that line drops to within 2% of baseline, the average radius of the spheroid is calculated. The invasive ratio is then calculated. Examples of image used to determine the threshold for average radius (top) and the calculation of average radius after 24 hours (bottom) are displayed.

Figure S6

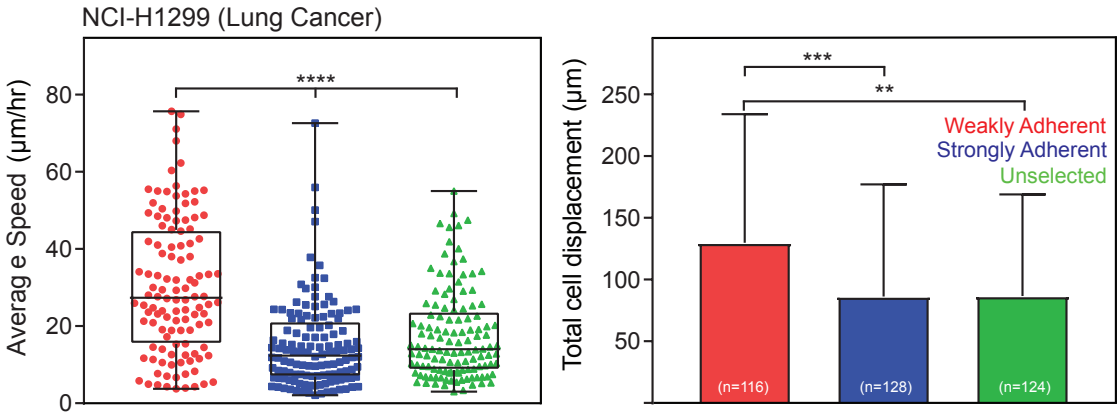

Supplementary Figure 3.6. Other Epithelial Cells Populations Exhibit Migration Differences Post-Sort. (A) Average speed and (B) total displacement is plotted for NCI-H1299 lung carcinoma cells sorted by the indicated shear stress and allowed to migrate on collagen gels for 24 hours. Percentages in panel A reflect the portion of each population that detaches or remains adherent at a given stress. n=3 biological replicates for the number of cells per condition inset in the bars in panel B. One-way ANOVA with Tukey test for multiple comparisons was used to indicate significance where **p<0.01, ***p<0.001, and ***p<0.0001.

Figure S7

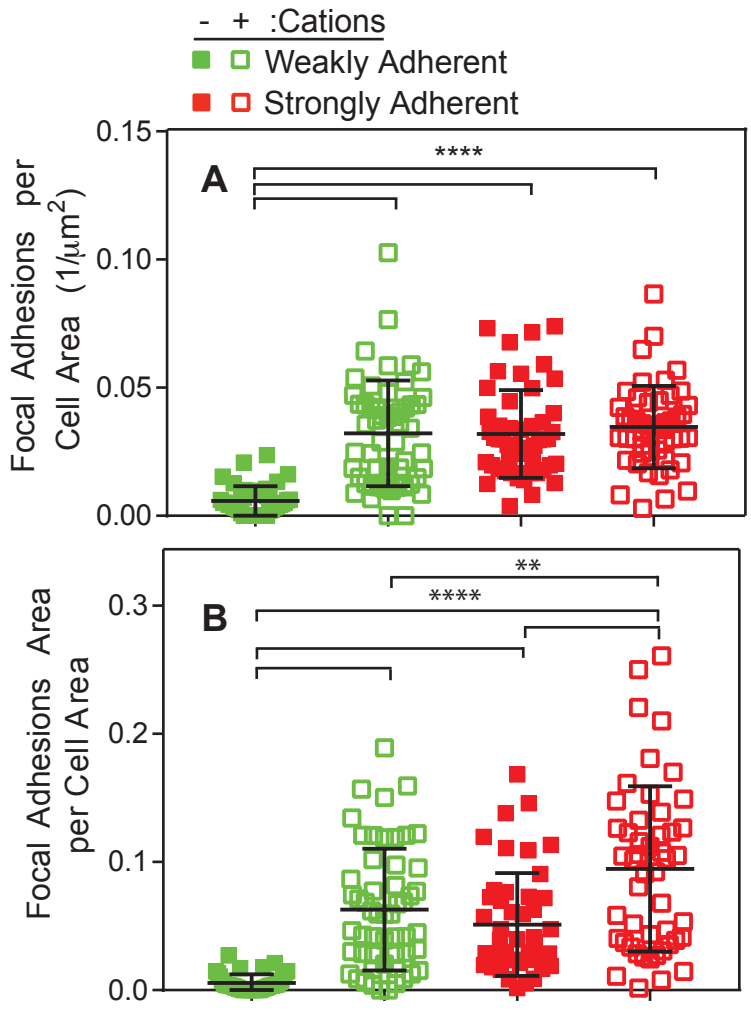

Supplementary Figure 3.7. Focal Adhesion Disassembly in Stromal Cation Conditions.
(A) Focal adhesion density and (B) total area per cell area is plotted for the indicated sorting and cation conditions for MDA-MB231 cells cultured on collagen. n=3 biological replicates and >50 cells/condition. One-way ANOVA with Tukey's multiple comparison test was performed for the indicated comparisons with **p<0.01, ***p<0.001, and ****p<0.0001.

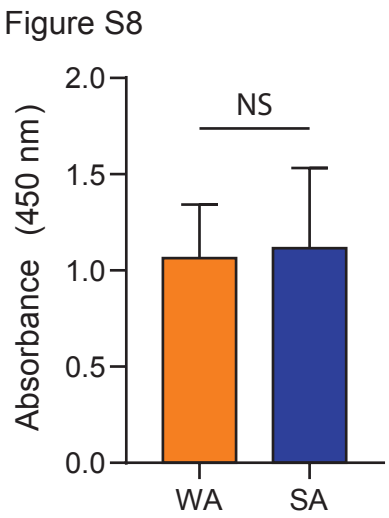

Supplementary Figure 3.8. Proliferation of Post-Sort Cells is not Different. BrdU absorbance is plotted for cells post sort.

Supplementary Table 3.9. qPCR Primers.
Primer sequences for real time PCR.

Target Gene	Forward	Reverse
GAS2L3	AGCCTGCAATTCAAGTATGGTT	TGGTCCGTGTCTGGGAGTC
DST	GATCTTACAGCTCTGCCAGTGTGT	AGTAGCTTCTTTGGCATCATTGAA
KIF14	TGGTGAAATGGCCTGTACAAGT	GGCAACCAGTTAACCCTTTGAG
SYNE2	ACCACCCTATGGAAAGCTACT	CATCTCCCATCTGTCGAAGGC
GAPDH	TCGACAGTCAGCCGCATCTTC	ACCAAATCCGTTGACTCCGAC
Fibronectin (Standard)	AGGCTTGAACCAACCTACGGA	GCCTAAGCACTGGCACAACAG

Supplementary Table 3.10. Genes linked to highlighted GO terms that were used for TCGA analysis.
List of all genes from the ontological terms in Figure 4 that were included in the TCGA analysis. Genes are shown in alphabetical order.

Gene Name	Gene Name	Gene Name	Gene Name
AHNAK	CEP350	KIF11	PEAK1
AKAP13	CEP97	KIF14	PLEKHH2
AKAP9	CKAP2	KIF18A	PLK2
ALMS1	CKAP5	KIF18B	PSRC1
APC	CNTRL	KIF20A	PTPN14
ASPM	DCLRE1B	KIF20B	RANBP2
ATM	DSP	KIF4A	RBBP6
BIRC6	DST	KNSTRN	RCSD1
BMF	DTL	KRT17	REEP4
BRCA2	DYNC1H1	KRT81	RIF1
BUB1B	DYNC2H1	MACF1	SAA1
CCDC88A	E2F1	MAP1B	SCLT1
CCNA1	ESPL1	MCM2	SETD2
CCNB1	FLG	MCM3	SH3PXD2A
CCNB2	FRMD6	MDN1	SLC7A11
CCNF	GAS2L3	MYH15	SPAG5
CDC25B	GEM	MYO5A	SPTBN1
CDC42BPA	GEN1	MYO9A	SYNE1
CDC42EP2	GPSM2	NAV1	SYNE2
CDC45	GTSE1	NDE1	TACC3
CDC6	HDAC4	NEK2	TOP2A
CENPE	HERC2	PAWR	TRIM59
CENPF	HMMR	PCNA	TTK
CENPJ	HTT	PCNT	UBR4
CEP192	KIAA0586	PDE4DIP	UTRN

3.7 Acknowledgements

The authors thank Drs. Jing Yang and Eugene Yeo (UCSD) as well as Cian O'Leary (RSCI) for helpful discussions and the UCSD Campus Research Machine Shop for assistance in device fabrication. The results shown here are in part based upon data generated by the TCGA Research Network: https://www.cancer.gov/tcga. A.J.E. acknowledges grant support from the National Institutes of Health (R01CA206880 and R21CA217735) and National Science Foundation (1763139). P.K. acknowledges grant support from the National Science Foundation (1763132) and the Army Research Office (W911NF-17-1-0413). S.I.F. acknowledges grant support from the Faculty Early Career Development Program (CAREER) Awards (1651855) and American Cancer Society Institutional Research Grant (15–172–45-IRG) provided through the Moores Cancer Center at the University of California San Diego. P.B., A.B., and A.K. were supported by the National Science Foundation GRFP. National Institutes of Health fellowship awards also supported A.K. (T32AR060712) and J.K.P (F32HL126406) as well as the ARCS/Roche Foundation Scholar Award Program in the Life Science (A.K.).

Chapter 3, in full, is a reprint of the material as it appears in Beri, P., Popravko, A., Yeoman, B., Kumar, A., Chen, K., Hodzic, E., Chiang, A., Banisadr, A., Placone, J.K., Carter, H., Fraley, S., Katira, P., and Engler, A.J. "Cell adhesiveness serves as a biophysical marker for metastatic potential" *Cancer Research*, 2020. 80(4): 901-911. The dissertation author was the primary author of this paper.

Chapter 4.

An *in vivo* demonstration of adhesion strength as a predictive marker of metastatic potential

4.1 Abstract

Despite a rise in early stage detection of certain cancers, particularly breast cancer, local or regional invasion can reduce the 5-year survival rate of patients. Due to heterogeneity within the tumor and across tumors from different patients, there are no universal biological markers that can predict disease outcome. Adhesion strength has emerged as potential biophysical marker, but its links to cancer cell aggression and metastatic potential have only been demonstrated *in vitro*. It is essential to show that weak cellular adhesion correlates with more aggressive cells in an *in vivo* setting to demonstrate the clinical relevance of adhesion strength as a prognostic marker. We have observed that, in a murine mammary tumor model, that invaded cells in the mammary stroma have lower cellular adhesion strength than cells that remain in the stiff tumor. These data suggest that adhesion strength can serve as a marker of metastatic potential and can be utilized in a prognostic fashion to screen patient samples.

4.2 Introduction

While breast cancer has high rates of early stage detection (ranging from 47% at ages 15-39 to 68% at ages 65+), metastasis of the primary tumor can reduce the patient's 5-year survival rate by 73% (*178*). Even regional invasion of the cancer can reduce 5-year survival rates by 14%; the recurrence rates are even worse for other solid tumors (*178*). It is therefore essential to determine the aggressiveness of the tumor when it is at the local or regional invasion stages in order to effectively predict the likelihood of recurrence. However, it is difficult to determine the aggressiveness of the tumor due to a lack of universal molecular prognostic markers(*122, 145*). Due to the similarities in the physical process of metastasis amongst epithelial cancers, biophysical attributes of cells, such as cellular deformability and cell-cell and cell-ECM interactions, have emerged as potential universal markers of aggressiveness(*80, 84-87, 147*). Current FDA-approved assays that utilize biophysical properties to detect cancer cells focus on circulating tumor cells, at which point the disease has already progressed too far for effective prognostic measures.

Prior evidence strongly supports weak cellular adhesion strength to the ECM as a biophysical marker of aggressive and/or metastatic cells, due to an increase in focal adhesion turnover and contractility that stems from intrinsic transcriptomic differences in proteins involved in the microtubule cytoskeleton and vesicular transport (*16, 90, 91, 120, 121, 126, 148, 179*). This transcriptomic profile, when present in triple negative breast cancer patients, correlated with shorter disease-free intervals (*179*). Despite the strong evidence, the assays were performed *in vitro* and thus cannot truly mimic the tumor microenvironment. Therefore, it is essential to demonstrate the link between decreased adhesion strength and increased invasive and metastatic behavior *in vivo*. Using a murine mammary tumor model, we have observed that cells that have locally invaded into the

stroma have a decreased adhesion strength in comparison to cells that have remained in the tumor bolus.

4.3 Results

4.3.1 MDA-MB 231 cellular adhesion strength and migratory differences were maintained post-viral transduction

In order to visualize tumor growth in vivo and sort cells of interest via FACS post-resection, MDA-MB231 cells were exposed to lentiviral vectors containing GFP and firefly luciferase and selected for both markers through puromycin treatment (luciferase) and FACS (GFP+) (Supplemental Figure 4.1A-B). To ensure that the transduced cells maintained the same adhesion strength heterogeneity and migratory differences that were observed previously, the cells were sheared using pre-determined shear stresses to isolate weakly and strongly adherent fractions and assess their migration on collagen gels over 24 hours(*179*). As expected, the weakly adherent cells had a greater cell speed and total cell displacement in comparison to the strongly adherent cells (Supplemental Figure 4.1C-D). These data indicate that the inherent heterogeneity of the cell population was unaffected by viral transduction.

4.3.2 Invaded cells have decreased adhesion strength compared to cells in the tumor bolus

Our previous findings have shown that metastatic cell lines have a lower adhesion strength and more labile focal adhesions than non-metastatic cell lines(*91*). Within metastatic cell lines, weakly adherent cells isolated using a microfluidic shear assay were

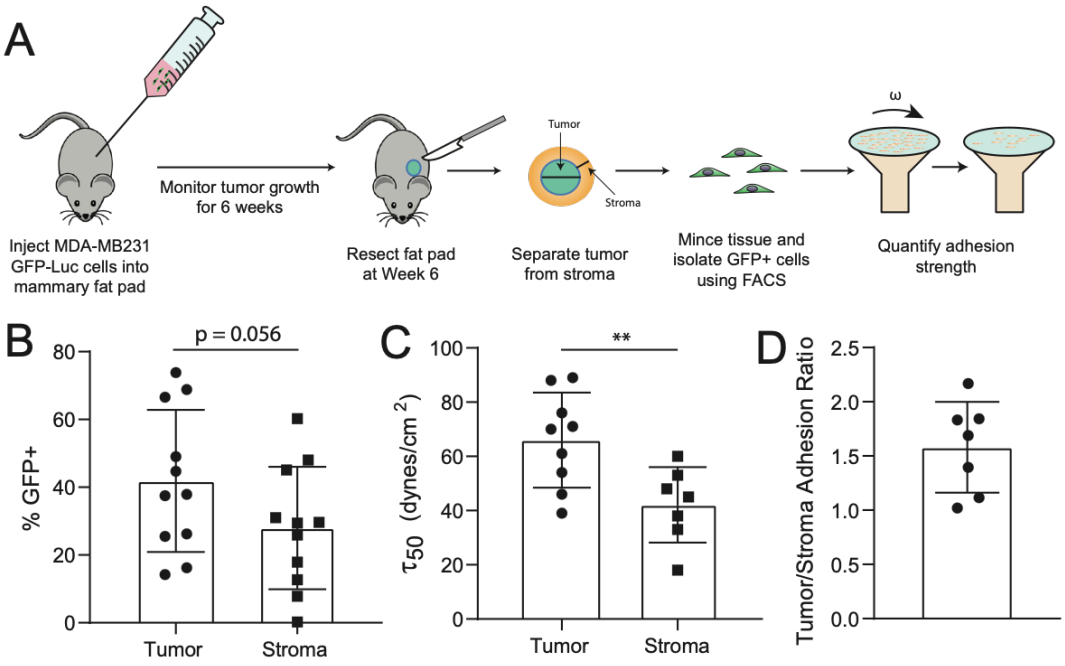

Figure 4.1. MDA-MB231 cells that have invaded into the stroma display decreased adhesion strength compared to cells in the stiff tumor.
(A) There are fewer GFP-positive cells present in the stroma versus the tumor. (B) Invaded MDA-MB231 cells have decreased adhesion strength compared to MDA-MB231 cells that remain in the tumor.

more migratory, more contractile, and had more labile focal adhesions than strongly adherent cells within the same population(*179*). Since decreased adhesion correlated with an increase in behaviors associated with more aggressive cancer cells, we wanted to investigate if these findings could be recapitulated *in vivo*. We injected MDA-MB231 cells that had stable expression of GFP and luciferase into the mammary fat pads of 11-week-old NOD/SCIDγ mice. Using IVIS, we monitored the growth of the tumors at 2-week intervals and resected the tumor at 6 weeks post injection (Supplemental Figure 4.2A-B). GFP+ cells were isolated from the tumor bolus and surrounding stroma, separated manually under an inverted fluorescence microscope and sorted using FACS (Figure 4.1A, Supplemental Figure 4.2C). The percentage of GFP+ cells present in the stroma appear to be less than those present in the tumor (Figure 4.1B). The adhesion strength of the cells

that had invaded into the stroma and the cells that remained in the tumor bolus was calculated using the spinning disk shear assay. We observed that the invaded cells in the surrounding stroma displayed a decreased adhesion strength compared to the cells that remained in the tumor bolus (Figure 4.1C). Calculation of the ratio of tumor to stromal adhesion strength, conducted for cells isolated from the tumoral and stromal regions of the same tumors, indicate that the tumoral cells, on average, have a higher adhesion strength compared to stromal cells from the same initial population (Figure 4.1D). This is consistent with our *in vitro* findings that link decreased adhesion to increased aggressiveness and metastatic potential.

4.4 Future Directions

The next portion of this paper would involve using patient-derived xenografts to assess the predictive capability of adhesion strength as a marker of metastatic potential. Patient tumor fragments will be grafted into the mammary fat pad of NOD/SCIDγ mice and tumor size can be assessed using calipers. Upon resection, the patient-derived xenografts (PDXs) can be dissociated into single cells using established protocols(*180*). A portion of the cells can be sequenced and compared to the previously described weakly adherent signature to obtain a correlation score. The rest of the cells can be seeded onto a glass plate and sheared at a pre-defined shear stress to determine the percent of cells that have detached. The percent of cells detached combined with the correlation score combined could result in a more accurate prediction of patient outcome. The mice will be monitored for recurrence to generate survival curves and determine the efficacy of adhesion as a predictor of outcome.

4.5 Methods

4.5.1 Cell Culture

MDA-MB231 were cultured in DMEM, 10% Fetal Bovine Serum (FBS), and 1% antibiotic/antimycotic. Products were purchased from Life Technologies. Cells were obtained from ATCC (authenticated by morphology, growth curve, and isoenzyme analysis), verified mycoplasma free via PCR, and were not used beyond passage 14.

4.5.2 Creating GFP and Luciferase-Expressing MDA-MB 231 cells and validating adhesion heterogeneity

To make lentivirus particles, HEK293T were seeded into a 20 cm dish in high glucose DMEM supplemented with 10% FBS and 1% antibiotic/antimycotic. Cells were allowed to grow until 70% confluence. At this time, 3 μg of pMD2.G (Addgene 12259) , 12 μg of pCMV deltaR8.2 (Addgene 12263), and 9 μg of either GFP or luciferase plasmid (generous gift of the Kun-Liang Guan lab) was added to 1.5 mL Opti-MEM. Separately, 36 μL of Lipofectectamine 2000 was added to 1.5 mL Opti-MEM. After incubating the solutions for 15 minutes, the solutions were mixed and allowed to incubate for an additional 30 minutes. The mixture was then added dropwise to HEK293T cells. After 48 hours, media was harvested and replaced. After an additional 24 hours, media was harvested again and all media was concentrated using an Amicon Ultra-15 ultrafilter (100,000 NMWL cutoff) to a final volume of 1 mL, which was aliquoted into 250 μL aliquots and frozen at -80C.

Media with packaged lentiviral particles was added to cultured MDA-MB231 cells along with 8 μg/mL of polybrene. After 24 hours, the media was aspirated and replaced

with normal culture media. Upon observation of GFP expression through fluorescence microscopy, the cultured cells were treated with 2 μg/mL of puromycin in culture media and cultured for two days. The remaining cells were sorted using FACS for presence of GFP. GFP expression was validated via fluorescence microscopy using a Nikon Eclipse Ti-S microscope at 10X magnification with FITC.

To validate that adhesion heterogeneity is maintained post-transduction, weakly and strongly adherent subpopulations were isolate by exposure to pre-determined low and high shear stresses, respectively, in a microfluidic flow chamber as previously described(*179*). Weakly and strongly adherent cell fractions were seeded onto 2.4 mg/mL Type I collagen gels (Corning) and imaged with a Nikon Eclipse Ti-S microscope equipped with a temperature- and CO2-controlled stage for 24 hours, after which their migration was tracked and analyzed using a custom MATLAB script. Cells that divided or did not remain in the frame for 24 hours were not tracked.

4.5.3 Isolation of MDA-MB 231 cells in tumor and surrounding stroma

All animal care and experiments were approved by the Institutional Animal Care and Use Committee of the University of California, San Diego. 1×10^6 MDA-MB 231 cells, expressing GFP and Luciferase, were suspended in 40 μL of Matrigel-PBS (1:1) mixture and were injected bilaterally into the inguinal mammary fat pads of 11-week-old female NOD/SCIDγ mice. Tumor growth was monitored at 2-week intervals and the mice were sacrificed at 6 weeks post-injection. Mice were dissected and the fat pads were surgically removed. Using an inverted fluorescent microscope, the stiffened tumor bolus was manually separated from the surrounding stroma. Both tumor and stroma were finely minced then treated with Accumax and placed on a shaker at room temperature for 2 hours.

Cells were then pipetted through a 70 μm cell strainer and neutralized with culture media, after which they were centrifuged and resuspended in FACS buffer (2% goat serum, 5 mM EDTA in PBS). GFP-positive cells in tumor and stroma sections were sorted via FACS.

4.5.4 Quantification of cellular adhesion strength

GFP-positive MDA-MB231 cells from tumor and stroma fractions were seeded onto 25 mm glass coverslips—coated with 2 μg/mL of fibronectin and blocked with 5% bovine serum albumin—and incubated overnight at 37°C. Cells were then exposed to shear stress at varying RPMs using the spinning disk shear assay as previously described(*91*). Cells were immediately fixed in 3.7% formaldehyde for 10 minutes, after which they were stained with 1:2000 Hoechst in DI water. Quantification of cellular adhesion strength was performed as previously described(*91*).

4.6 Acknowledgements

Chapter 4, in full, contains unpublished material as it appears in Beri, P., Tuler, J., and Engler, A.J. “An in vivo demonstration of adhesion strength as a predictive marker of metastatic potential.” The dissertation author is the primary author of this paper.

4.7 Supplementary Figures

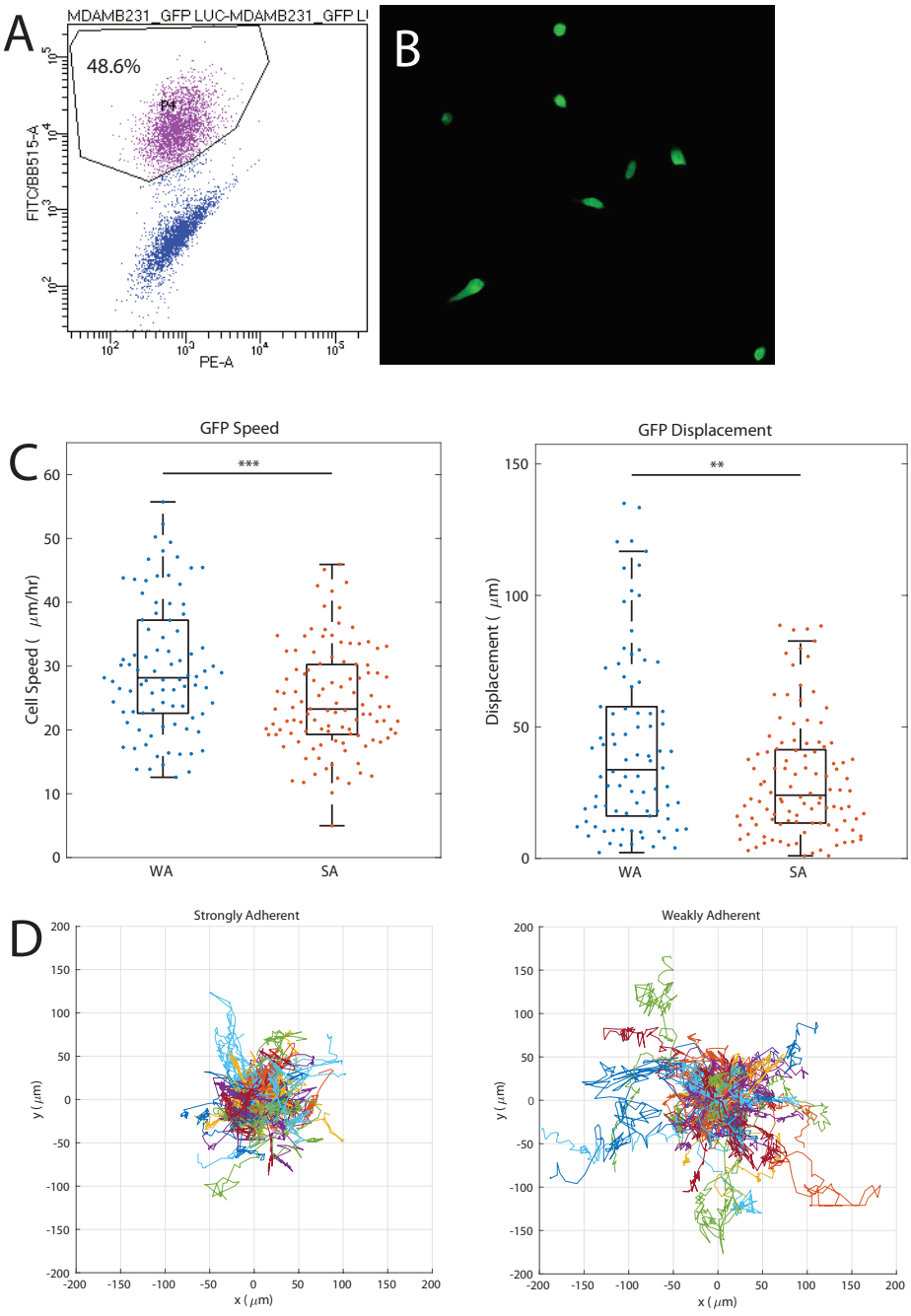

Supplementary Figure 4.1. GFP-Luciferase lentiviral transduction does not alter inherent heterogeneity of MDA-MB231 cells

(A) After treatment with puromycin to select for cells that expressed Luciferase, cells were sorted using FACS for GFP+ signal. (B) GFP expression was verified using fluorescence microscopy. (C),(D) Weakly adherent cells were more migratory than their strongly adherent counterparts, consistent with previous findings.

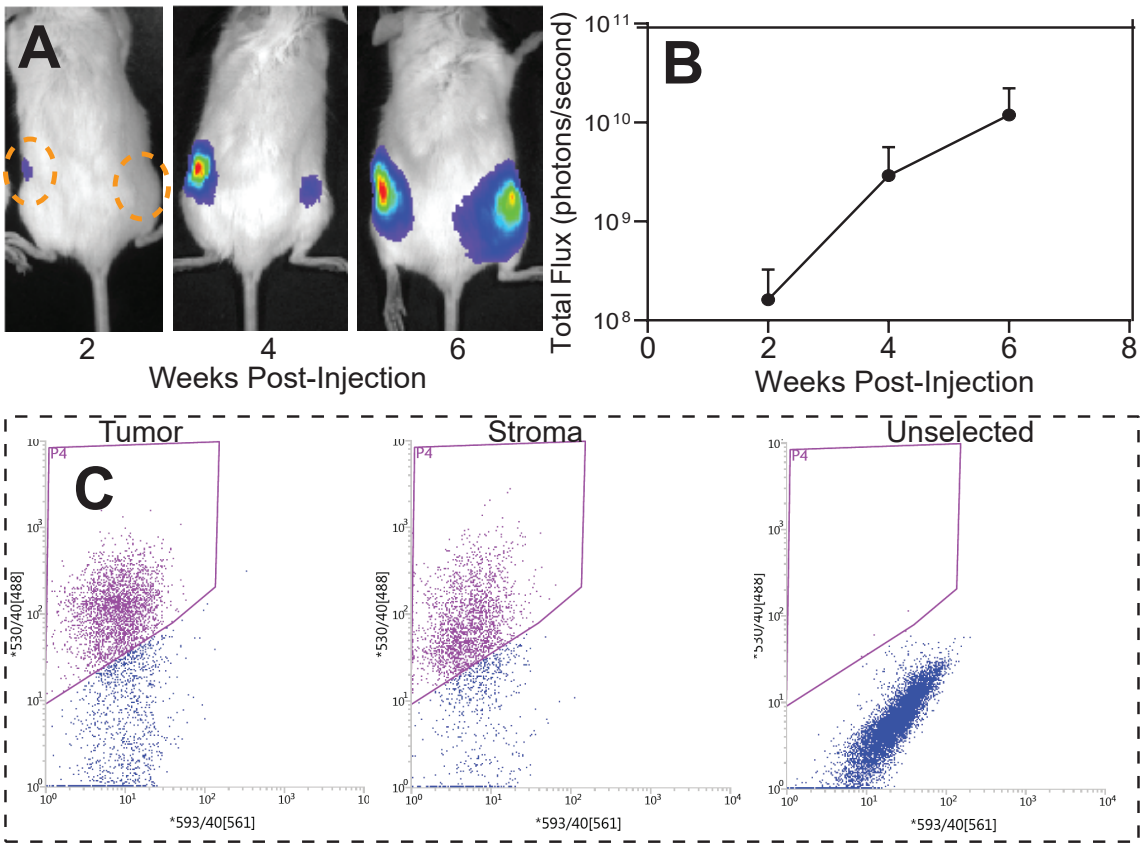

Supplementary Figure 4.2. Tumor growth was monitored using IVIS and GFP+ cells can be sorted from tumor and stroma.
(A) Tumor growth was monitored using IVIS at 2-week intervals using (B) total flux as a measurement. (C) After manual separation of the stiff tumor from the surrounding stroma and dissociation into single cells, GFP+ cells could be isolated from both tissue fractions using FACS.

Chapter 5.

Conclusions

5.1 Introduction

Cell-ECM interactions are an important factor in tumorigenesis and dissemination of cells from the primary tumor, as well as establishment of secondary sites. As detailed in Chapter 1, tumor microenvironments can be reconstructed *in vitro* using natural and synthetic materials, and engineered biomaterials can help identify the effects of specific ECM components on cancer progression. Cell-ECM interactions can also be exploited to detect and diagnose cancers both *in vivo* and *ex vivo*. In particular, the attachment of cancer cells to ECM, preference for specific ECM components, and the navigation of cancer cells through the ECM have enabled the development of *in vivo* and *ex vivo* technologies that can preferentially distinguish metastatic tumor fractions both within a tumor populations and across different populations. Cell-ECM interactions have brought to light innate biophysical properties that are shared between cancer cells of different epithelial origins and can be implemented in diagnostic assays to detect the most aggressive cancer cells.

5.2 Metastatic cancer cell populations display decreased adhesion strength and more labile focal adhesions compared to non-metastatic counterparts

Epithelial cancers demonstrate a remarkable heterogeneity in invasiveness and metastatic capabilities across patients. Recently, there has been a push to identify common signatures that distinguish more aggressive tumors not only with an epithelial cancer type, but also across cancers of different origin tissues. However, there are no universal biological markers that can distinguish more aggressive tumors from their less aggressive counterparts. As mentioned in Chapter 1, biophysical metrics that rely on specific interactions between cancer cells and the surrounding ECM have come into focus as potential universal biomarkers that identify tumoral invasive and metastatic capability based on observed mechanobiological differences. In Chapter 2, we focus on population adhesion strength as a biophysical metric to distinguish metastatic from non-metastatic breast cancer populations. We utilized a spinning-disk shear assay to quantify adhesion strength of cells with different metastatic potentials in the presence or absence of divalent cations (Mg^{2+} and Ca^{2+}). In the absence of cations—which mimics normal tissue—metastatic breast cancer cells displayed a reduced adhesion strength compared to their non-metastatic breast cancer and normal breast epithelial cell counterparts. We found that strongly adherent MDA-MB231 cells isolated at high shear stress showed decreased motility and processivity when compared to unselected cells in both 2D migration on collagen gels as well as in transwell migration assays. The decreased adhesion strength of MDA-MB231 cells in comparison to MCF10A cells can be attributed to faster focal adhesion disassembly in the absence of cations in the metastatic cell line. When MCF10A cells were exposed to RGD to functionally block integrins they experienced a decrease in adhesion strength as well as an increase in migration. These data suggest that focal adhesions in more metastatic cells are more labile and thus more sensitive to changes in

external cation concentrations in comparison to non-metastatic cells, which could drive differences in metastatic potential.

5.3 Weakly adherent cells within a heterogeneous population represent the most migratory and aggressive fraction

Similar to the heterogeneity in metastatic capability across patient tumors, there is an inherent heterogeneity within the population. As a result, certain cell fractions within a given population are more likely to disseminate from the primary tumor, denoting the most aggressive cells in the population. In Chapter 2, we discussed how metastatic cells have weaker population adhesion strength in comparison to non-metastatic cells. In Chapter 3, we investigated the increased migratory and metastatic potential of weakly adherent cells in comparison to strongly adherent cells within the metastatic MDA-MB231 breast cancer cell line. We utilized a microfluidic chamber to isolated weakly and strongly adherent cells by exposing an inherently heterogeneous cell population to low—to isolate weakly adherent—and high—to isolate strongly adherent—shear stresses. Isolated weakly adherent cells displayed increased migration in both 2D and 3D environments in comparison to strongly adherent cells. Similar to findings detailed in chapter 1, the decreased adhesion and increased motility of the weakly adherent cell fraction can be attributed to increased focal adhesion disassembly and sensitivity to external cation conditions as well as increased contractility. RNA sequencing and analyses of weakly and strongly adherent fractions revealed inherent transcriptomic differences in expression of

genes associated with the cytoskeleton, particularly microtubules, and motor proteins involved in vesicular transport and contraction. When the gene expression profile of weakly and strongly adherent cells were compared to triple negative breast cancer patient datasets obtained from The Cancer Genome Atlas, we found that patients with gene expression profiles that aligned closely with weakly adherent cells had decreased progression-free and disease-free intervals than patients that aligned closely with strongly adherent cells. When we treated weakly and strongly adherent cell fractions with nocodazole and paclitaxel, we observed a decrease in migration speed of weakly adherent cells but no change in the migration speed of strongly adherent cells. This study reveals the potential of using weak adhesion as a biophysical metric of metastatic capability.

5.4 Locally invaded cancer cells demonstrate decreased adhesion compare to cells within the tumor

In Chapter 3, we found that weak adhesion strength corresponds with increased migratory propensity due to more dynamic focal adhesions and increased contractility. However, the data was acquired in an *in vitro* setting and we wanted to investigate if weak adhesion corresponds to increased invasion *in vivo*. We injected GFP and Luciferase-expressing MDA-MB231 cells into the mammary fat pads of NOD/SCIDγ mice and monitored tumor growth at 2-week intervals. Upon resection of the tumor, we manually separated tumor from stroma and isolated GFP+ cells using FACS, after which their adhesion strength was assessed using a spinning disk shear device. We observed that the cells that have invaded into the stroma displayed a decreased adhesion strength compared to cells that remained in the tumor, indicating that adhesion strength is an indicator of more

aggressive cells. We will further validate this claim by implanting PDXs into murine mammary fat pads, resecting the tumor and dissociating into single cells, and both sequencing and shearing the cells. The percent of cells detached and how well the gene expression corresponds to the previously-defined weakly adherent cell signature will provide a prediction of recurrence. Simultaneously, the mice will be monitored for recurrence and the survival data will be compared to the prediction based on cellular adhesion.

5.5 Future directions

While this dissertation demonstrated the potential of adhesion strength as a biophysical marker of cancer cell aggressiveness, additional studies are required to further validate this link. The next step is to further investigate if the findings are recapitulated *in vivo*. We showed in Chapter 3 that the weakly adherent signature correlated with decreased disease-free interval in triple negative breast cancer patients. Firstly, we can expand upon this finding and refine the weakly adherent signature described in Chapter 3 by shear sorting weakly adherent cells from a wide range of breast cancer cell lines of varying metastatic potentials and performing RNA sequencing on the cell fraction to determine the similarities between weakly adherent cells and identify a unique weak adhesion signature. Narrowing down the most significant proteins that overlap between these sets can help identify proteins that are responsible for heterogeneity in metastatic potential across and within tumors. Using a tissue microarray with known patient outcomes, we can stain for the presence of these target proteins and confirm that their presence is heterogeneous both across and within tumors and can be correlated to difference in patient outcomes. We can

also compare this signature to the RNA sequencing results from the PDX cells outlined in the Future Directions section of Chapter 4 to obtain an improved correlation score. We can further use this refined signature by RNA sequencing patient biopsy samples and mapping their expression to our refined signature to predict the likelihood of recurrence and monitor the patient's disease progression to validate the predictions.

Secondly, since we found this link between adhesion strength and aggressive behavior across cell lines of different epithelial tissue origins (lung, breast, and prostate cancer), we can compare the weakly and strongly adherent cells of these three cancer cell lines through RNA sequencing to find proteins that are expressed across different cancers and can reveal universal protein targets.

References

1. S. Affo, L.-X. Yu, R. F. Schwabe, The Role of Cancer-Associated Fibroblasts and Fibrosis in Liver Cancer. *Annual Review of Pathology: Mechanisms of Disease* **12**, 153-186 (2017).

2. D. Pankova, Y. Chen, M. Terajima, M. J. Schliekelman, B. N. Baird, M. Fahrenholtz, L. Sun, B. J. Gill, T. J. Vadakkan, M. P. Kim, Y.-H. Ahn, J. D. Roybal, X. Liu, E. R. Parra Cuentas, J. Rodriguez, I. I. Wistuba, C. J. Creighton, D. L. Gibbons, J. M. Hicks, M. E. Dickinson, J. L. West, K. J. Grande-Allen, S. M. Hanash, M. Yamauchi, J. M. Kurie, Cancer-Associated Fibroblasts Induce a Collagen Cross-link Switch in Tumor Stroma. *Molecular Cancer Research* **14**, 287-295 (2016).

3. M. J. Paszek, N. Zahir, K. R. Johnson, J. N. Lakins, G. I. Rozenberg, A. Gefen, C. A. Reinhart-King, S. S. Margulies, M. Dembo, D. Boettiger, D. A. Hammer, V. M. Weaver, Tensional homeostasis and the malignant phenotype. *Cancer Cell* **8**, 241-254 (2005).

4. M. W. Pickup, J. K. Mouw, V. M. Weaver, The extracellular matrix modulates the hallmarks of cancer. *EMBO reports* **15**, 1243-1253 (2014).

5. K. R. Levental, H. Yu, L. Kass, J. N. Lakins, M. Egeblad, J. T. Erler, S. F. T. Fong, K. Csiszar, A. Giaccia, W. Weninger, M. Yamauchi, D. L. Gasser, V. M. Weaver, Matrix Crosslinking Forces Tumor Progression by Enhancing Integrin Signaling. *Cell* **139**, 891-906 (2009).

6. I. W. Mak, N. Evaniew, M. Ghert, Lost in translation: animal models and clinical trials in cancer treatment. *Am J Transl Res* **6**, 114-118 (2014).

7. M. J. Bissell, H. G. Hall, G. Parry, How does the extracellular matrix direct gene expression? *Journal of Theoretical Biology* **99**, 31-68 (1982).

8. C. M. Kraning-Rush, J. P. Califano, C. A. Reinhart-King, Cellular traction stresses increase with increasing metastatic potential. *PloS one* **7**, e32572-e32572 (2012).

9. J. L. Leight, M. A. Wozniak, S. Chen, M. L. Lynch, C. S. Chen, Matrix rigidity regulates a switch between TGF-β1–induced apoptosis and epithelial–mesenchymal transition. *Molecular Biology of the Cell* **23**, 781-791 (2012).

10. R. S. Stowers, S. C. Allen, L. J. Suggs, Dynamic phototuning of 3D hydrogel stiffness. *Proceedings of the National Academy of Sciences* **112**, 1953-1958 (2015).

11. S. C. Wei, L. Fattet, J. H. Tsai, Y. Guo, V. H. Pai, H. E. Majeski, A. C. Chen, R. L. Sah, S. S. Taylor, A. J. Engler, J. Yang, Matrix stiffness drives epithelial–mesenchymal transition and tumour metastasis through a TWIST1–G3BP2 mechanotransduction pathway. *Nature Cell Biology* **17**, 678 (2015).

12. J. Fenner, A. C. Stacer, F. Winterroth, T. D. Johnson, K. E. Luker, G. D. Luker, Macroscopic Stiffness of Breast Tumors Predicts Metastasis. *Sci Rep* **4**, 5512 (2014).

13. J. R. Tse, A. J. Engler, Preparation of Hydrogel Substrates with Tunable Mechanical Properties. *Current Protocols in Cell Biology* **47**, 10.16.11-10.16.16 (2010).

14. J. T. Emerman, D. R. Pitelka, Maintenance and induction of morphological differentiation in dissociated mammary epithelium on floating collagen membranes. *In Vitro* **13**, 316-328 (1977).

15. M. J. Bissell, in *International Review of Cytology,* G. H. Bourne, J. F. Danielli, K. W. Jeon, Eds. (Academic Press, 1981), vol. 70, pp. 27-100.

16. N. E. Reticker-Flynn, D. F. B. Malta, M. M. Winslow, J. M. Lamar, M. J. Xu, G. H. Underhill, R. O. Hynes, T. E. Jacks, S. N. Bhatia, A combinatorial extracellular matrix platform identifies cell-extracellular matrix interactions that correlate with metastasis. *Nat. Commun.* **3**, 1122 (2012).

17. Y. Maghdouri-White, L. W. Elmore, G. L. Bowlin, D. Dréau, Breast epithelial cell infiltration in enhanced electrospun silk scaffolds. *Journal of Tissue Engineering and Regenerative Medicine* **10**, E121-E131 (2016).

18. Z. Chen, Z. Chen, A. Zhang, J. Hu, X. Wang, Z. Yang, Electrospun nanofibers for cancer diagnosis and therapy. *Biomater. Sci.* **4**, 922-932 (2016).

19. K. Kushiro, T. Yaginuma, A. Ryo, M. Takai, Differences in Three-Dimensional Geometric Recognition by Non-Cancerous and Cancerous Epithelial Cells on Microgroove-Based Topography. *Sci Rep* **7**, 4244 (2017).

20. D. Ning, B. Duong, G. Thomas, Y. Qiao, L. Ma, Q. Wen, M. Su, Mechanical and Morphological Analysis of Cancer Cells on Nanostructured Substrates. *Langmuir* **32**, 2718-2723 (2016).

21. P. K. Chaudhuri, C. Q. Pan, B. C. Low, C. T. Lim, Topography induces differential sensitivity on cancer cell proliferation via Rho-ROCK-Myosin contractility. *Sci Rep* **6**, 19672-19672 (2016).

22. W. Q. Chen, S. N. Weng, F. Zhang, S. Allen, X. Li, L. W. Bao, R. H. W. Lam, J. A. Macoska, S. D. Merajver, J. P. Fu, Nanoroughened Surfaces for Efficient Capture of Circulating Tumor Cells without Using Capture Antibodies. *ACS Nano* **7**, 566-575 (2013).

23. W. Zhang, K. Zhao, C. E. Banks, Y. Zhang, Antibody-modified hydroxyapatite surfaces for the efficient capture of bladder cancer cells in a patient's urine without recourse to any sample pre-treatment. *J. Mat. Chem. B* **5**, 8125-8132 (2017).

24. H. W. Xu, B. Dong, Q. Q. Xiao, X. K. Sun, X. R. Zhang, J. K. Lyu, Y. D. Yang, L. Xu, X. Bai, S. Zhang, H. W. Song, Three-Dimensional Inverse Opal Photonic Crystal Substrates toward Efficient Capture of Circulating Tumor Cells. *ACS Appl. Mater. Interfaces* **9**, 30510-30518 (2017).

25. T. A. Ulrich, A. Jain, K. Tanner, J. L. MacKay, S. Kumar, Probing cellular mechanobiology in three-dimensional culture with collagen–agarose matrices. *Biomaterials* **31**, 1875-1884 (2010).

26. A. Pathak, S. Kumar, Independent regulation of tumor cell migration by matrix stiffness and confinement. *Proc. Natl. Acad. Sci. U. S. A.* **109**, 10334-10339 (2012).

27. M.-F. Pang, M. J. Siedlik, S. Han, M. Stallings-Mann, D. C. Radisky, C. M. Nelson, Tissue Stiffness and Hypoxia Modulate the Integrin-Linked Kinase ILK to Control Breast Cancer Stem-like Cells. *Cancer Res.* **76**, 5277-5287 (2016).

28. E. Jabbari, S. K. Sarvestani, L. Daneshian, S. Moeinzadeh, Optimum 3D Matrix Stiffness for Maintenance of Cancer Stem Cells Is Dependent on Tissue Origin of Cancer Cells. *PLOS ONE* **10**, e0132377 (2015).

29. X. Z. Shu, S. Ahmad, Y. Liu, G. D. Prestwich, Synthesis and evaluation of injectable, in situ crosslinkable synthetic extracellular matrices for tissue engineering. *Journal of Biomedical Materials Research Part A* **79A**, 902-912 (2006).

30. J. L. Young, A. J. Engler, Hydrogels with time-dependent material properties enhance cardiomyocyte differentiation in vitro. *Biomaterials* **32**, 1002-1009 (2011).

31. M. Guvendiren, J. A. Burdick, Stiffening hydrogels to probe short- and long-term cellular responses to dynamic mechanics. *Nat. Commun.* **3**, 792 (2012).

32. M. G. Ondeck, A. J. Engler, Mechanical Characterization of a Dynamic and Tunable Methacrylated Hyaluronic Acid Hydrogel. *Journal of Biomechanical Engineering* **138**, (2016).

33. R. S. Stowers, S. C. Allen, K. Sanchez, C. L. Davis, N. D. Ebelt, C. Van Den Berg, L. J. Suggs, Extracellular Matrix Stiffening Induces a Malignant Phenotypic Transition in Breast Epithelial Cells. *Cell. Mol. Bioeng.* **10**, 114-123 (2017).

34. A. M. Kloxin, A. M. Kasko, C. N. Salinas, K. S. Anseth, Photodegradable Hydrogels for Dynamic Tuning of Physical and Chemical Properties. *Science* **324**, 59-63 (2009).

35. C. M. Denais, R. M. Gilbert, P. Isermann, A. L. McGregor, M. te Lindert, B. Weigelin, P. M. Davidson, P. Friedl, K. Wolf, J. Lammerding, Nuclear envelope rupture and repair during cancer cell migration. *Science* **352**, 353-358 (2016).

36. Y. Attieh, D. M. Vignjevic, The hallmarks of CAFs in cancer invasion. *European Journal of Cell Biology* **95**, 493-502 (2016).

37. D. Hanahan, Robert A. Weinberg, Hallmarks of Cancer: The Next Generation. *Cell* **144**, 646-674 (2011).

38. C. Gaggioli, S. Hooper, C. Hidalgo-Carcedo, R. Grosse, J. F. Marshall, K. Harrington, E. Sahai, Fibroblast-led collective invasion of carcinoma cells with differing roles for RhoGTPases in leading and following cells. *Nat. Cell Biol.* **9**, 1392-1400 (2007).

39. Jacky G. Goetz, S. Minguet, I. Navarro-Lérida, Juan J. Lazcano, R. Samaniego, E. Calvo, M. Tello, T. Osteso-Ibáñez, T. Pellinen, A. Echarri, A. Cerezo, Andres J. P. Klein-Szanto, R. Garcia, Patricia J. Keely, P. Sánchez-Mateos, E. Cukierman, Miguel A. Del Pozo, Biomechanical Remodeling of the Microenvironment by Stromal Caveolin-1 Favors Tumor Invasion and Metastasis. *Cell* **146**, 148-163 (2011).

40. A. Glentis, P. Oertle, P. Mariani, A. Chikina, F. El Marjou, Y. Attieh, F. Zaccarini, M. Lae, D. Loew, F. Dingli, P. Sirven, M. Schoumacher, B. G. Gurchenkov, M. Plodinec, D. M. Vignjevic, Cancer-associated fibroblasts induce metalloprotease-independent cancer cell invasion of the basement membrane. *Nat. Commun.* **8**, 924 (2017).

41. K. Wang, R. C. Andresen Eguiluz, F. Wu, B. R. Seo, C. Fischbach, D. Gourdon, Stiffening and unfolding of early deposited-fibronectin increase proangiogenic factor secretion by breast cancer-associated stromal cells. *Biomaterials* **54**, 63-71 (2015).

42. A. Labernadie, T. Kato, A. Brugués, X. Serra-Picamal, S. Derzsi, E. Arwert, A. Weston, V. González-Tarragó, A. Elosegui-Artola, L. Albertazzi, J. Alcaraz, P. Roca-Cusachs, E. Sahai, X. Trepat, A mechanically active heterotypic E-cadherin/N-cadherin adhesion enables fibroblasts to drive cancer cell invasion. *Nat. Cell Biol.* **19**, 224-237 (2017).

43. F. Calvo, N. Ege, A. Grande-Garcia, S. Hooper, R. P. Jenkins, S. I. Chaudhry, K. Harrington, P. Williamson, E. Moeendarbary, G. Charras, E. Sahai, Mechanotransduction and YAP-dependent matrix remodelling is required for the generation and maintenance of cancer-associated fibroblasts. *Nat. Cell Biol.* **15**, 637-646 (2013).

44. M. B. Chen, J. A. Whisler, J. Fröse, C. Yu, Y. Shin, R. D. Kamm, On-chip human microvasculature assay for visualization and quantification of tumor cell extravasation dynamics. *Nat. Protoc.* **12**, 865-880 (2017).

45. H. Lee, W. Park, H. Ryu, N. L. Jeon, A microfluidic platform for quantitative analysis of cancer angiogenesis and intravasation. *Biomicrofluidics* **8**, 054102-054102 (2014).

46. I. K. Zervantonakis, S. K. Hughes-Alford, J. L. Charest, J. S. Condeelis, F. B. Gertler, R. D. Kamm, Three-dimensional microfluidic model for tumor cell intravasation and endothelial barrier function. *Proceedings of the National Academy of Sciences* **109**, 13515-13520 (2012).

47. M. B. Chen, J. A. Whisler, J. S. Jeon, R. D. Kamm, Mechanisms of tumor cell extravasation in an in vitro microvascular network platform. *Integr. Biol.* **5**, 1262-1271 (2013).

48. S. Bersini, J. S. Jeon, G. Dubini, C. Arrigoni, S. Chung, J. L. Charest, M. Moretti, R. D. Kamm, A microfluidic 3D in vitro model for specificity of breast cancer metastasis to bone. *Biomaterials* **35**, 2454-2461 (2014).

49. N. Saquib, J. Saquib, J. P. A. Ioannidis, Does screening for disease save lives in asymptomatic adults? Systematic review of meta-analyses and randomized trials. *International Journal of Epidemiology* **44**, 264-277 (2015).

50. Z. Zhang, H. Shiratsuchi, J. Lin, G. A. Chen, R. M. Reddy, E. Azizi, S. Fouladdel, A. C. Chang, L. Lin, H. Jiang, M. Waghray, G. Luker, D. M. Simeone, M. S. Wicha, D. G. Beer, N. Ramnath, S. Nagrath, Expansion of CTCs from early stage lung cancer patients using a microfluidic co-culture model. *Oncotarget* **5**, 12383-12397 (2014).

51. S. Mehta, A. Shelling, A. Muthukaruppan, A. Lasham, C. Blenkiron, G. Laking, C. Print, Predictive and prognostic molecular markers for cancer medicine. *Therapeutic Advances in Medical Oncology* **2**, 125-148 (2010).

52. W. Y. Qian, Y. Zhang, W. Q. Chen, Capturing Cancer: Emerging Microfluidic Technologies for the Capture and Characterization of Circulating Tumor Cells. *Small* **11**, 3850-3872 (2015).

53. G. S. Park, H. Kwon, D. W. Kwak, S. Y. Park, M. Kim, J. H. Lee, H. Han, S. Heo, X. S. Li, Y. H. Kim, J. G. Lee, W. Yang, H. Y. Cho, S. K. Kim, K. Kim, Full Surface Embedding of Gold Clusters on Silicon Nanowires for Efficient Capture and Photothermal Therapy of Circulating Tumor Cells (vol 12, pg 1638, 2012). *Nano Lett.* **12**, 2176-2176 (2012).

54. T. T. Zhai, D. K. Ye, Q. W. Zhang, Z. Q. Wu, X. H. Xia, Highly Efficient Capture and Electrochemical Release of Circulating Tumor Cells by Using Aptamers Modified Gold Nanowire Arrays. *ACS Appl. Mater. Interfaces* **9**, 34706-34714 (2017).

55. J. Zhang, L. Li, Y. Peng, Y. Chen, X. Lv, S. Li, X. Qin, H. Yang, C. Wu, Y. Liu, Surface chemistry induces mitochondria-mediated apoptosis of breast cancer cells via PTEN/PI3K/AKT signaling pathway. *Biochimica et Biophysica Acta (BBA) - Molecular Cell Research* **1865**, 172-185 (2018).

56. Y. J. Jan, J.-F. Chen, Y. Zhu, Y.-T. Lu, S. H. Chen, H. Chung, M. Smalley, Y.-W. Huang, J. Dong, L.-C. Chen, H.-H. Yu, J. S. Tomlinson, S. Hou, V. G. Agopian, E. M. Posadas, H.-R. Tseng, NanoVelcro rare-cell assays for detection and characterization of circulating tumor cells. *Adv. Drug Deliv. Rev.* **125**, 78-93 (2018).

57. L. X. Wang, W. Asghar, U. Demirci, Y. Wan, Nanostructured substrates for isolation of circulating tumor cells. *Nano Today* **8**, 374-387 (2013).

58. S. T. Wang, H. Wang, J. Jiao, K. J. Chen, G. E. Owens, K. I. Kamei, J. Sun, D. J. Sherman, C. P. Behrenbruch, H. Wu, H. R. Tseng, Three-Dimensional Nanostructured Substrates toward Efficient Capture of Circulating Tumor Cells. *Angew. Chem.-Int. Edit.* **48**, 8970-8973 (2009).

59. S. T. Wang, K. Liu, J. A. Liu, Z. T. F. Yu, X. W. Xu, L. B. Zhao, T. Lee, E. K. Lee, J. Reiss, Y. K. Lee, L. W. K. Chung, J. T. Huang, M. Rettig, D. Seligson, K. N. Duraiswamy, C. K. F. Shen, H. R. Tseng, Highly Efficient Capture of Circulating Tumor Cells by Using Nanostructured Silicon Substrates with Integrated Chaotic Micromixers. *Angew. Chem.-Int. Edit.* **50**, 3084-3088 (2011).

60. S. Guo, J. Q. Xu, M. Xie, W. Huang, E. F. Yuan, Y. Liu, L. P. Fan, S. B. Cheng, S. M. Liu, F. B. Wang, B. F. Yuan, W. G. Dong, X. L. Zhang, W. H. Huang, X. Zhou, Degradable Zinc-Phosphate-Based Hierarchical Nanosubstrates for Capture and Release of Circulating Tumor Cells. *ACS Appl. Mater. Interfaces* **8**, 15917-15925 (2016).

61. H. Y. Lou, W. T. Zhao, L. Hanson, C. N. Zeng, Y. Cui, B. X. Cui, Dual-Functional Lipid Coating for the Nanopillar-Based Capture of Circulating Tumor Cells with High Purity and Efficiency. *Langmuir* **33**, 1097-1104 (2017).

62. N. Sun, M. Liu, J. N. Wang, Z. L. Wang, X. P. Li, B. Jiang, R. J. Pei, Chitosan Nanofibers for Specific Capture and Nondestructive Release of CTCs Assisted by pCBMA Brushes. *Small* **12**, 5090-5097 (2016).

63. S. S. Rao, G. G. Bushnell, S. M. Azarin, G. Spicer, B. A. Aguado, J. R. Stoehr, E. J. Jiang, V. Backman, L. D. Shea, J. S. Jeruss, Enhanced Survival with Implantable Scaffolds That Capture Metastatic Breast Cancer Cells In Vivo. *Cancer Res.* **76**, 5209-5218 (2016).

64. S. M. Azarin, J. Yi, M. Gower, B. A. Aguado, M. E. Sullivan, A. G. Goodman, E. J. Jiang, S. S. Rao, Y. Y. Ren, S. L. Tucker, V. Backman, J. S. Jeruss, L. D. Shea, In vivo capture and label-free detection of early metastatic cells. *Nat. Commun.* **6**, 9 (2015).

65. S. Paget, The distribution of secondary growths in cancer of the breast. *The Lancet* **133**, 571-573 (1889).

66. B. A. Aguado, J. R. Gaffe, D. Nanavati, S. S. Rao, G. G. Bushnell, S. M. Azarin, L. D. Shea, Extracellular matrix mediators of metastatic cell colonization characterized using scaffold mimics of the pre-metastatic niche. *Acta Biomater.* **33**, 13-24 (2016).

67. B. Z. Qian, J. F. Li, H. Zhang, T. Kitamura, J. H. Zhang, L. R. Campion, E. A. Kaiser, L. A. Snyder, J. W. Pollard, CCL2 recruits inflammatory monocytes to facilitate breast-tumour metastasis. *Nature* **475**, 222-U129 (2011).

68. T. Kitamura, B. Z. Qian, J. W. Pollard, Immune cell promotion of metastasis. *Nat. Rev. Immunol.* **15**, 73-86 (2015).

69. S. Hiratsuka, A. Watanabe, H. Aburatani, Y. Maru, Tumour-mediated upregulation of chemoattractants and recruitment of myeloid cells predetermines lung metastasis. *Nat. Cell Biol.* **8**, 1369-U1331 (2006).

70. N. Mauro, C. Scialabba, G. Pitarresi, G. Giammona, Enhanced adhesion and in situ photothermal ablation of cancer cells in surface-functionalized electrospun microfiber scaffold with graphene oxide. *Int. J. Pharm.* **526**, 167-177 (2017).

71. H. S. Ma, C. A. Jiang, D. Zhai, Y. X. Luo, Y. Chen, F. Lv, Z. F. Yi, Y. Deng, J. W. Wang, J. Chang, C. T. Wu, A Bifunctional Biomaterial with Photothermal Effect forTumor Therapy and Bone Regeneration. *Adv. Funct. Mater.* **26**, 1197-1208 (2016).

72. B. A. Aguado, J. J. Wu, S. M. Azarin, D. Nanavati, S. S. Rao, G. G. Bushnell, C. B. Medicherla, L. D. Shea, Secretome identification of immune cell factors mediating metastatic cell homing. *Sci Rep* **5**, 13 (2015).

73. A. de la Fuente, L. Alonso-Alconada, C. Costa, J. Cueva, T. Garcia-Caballero, R. Lopez-Lopez, M. Abal, M-Trap: Exosome-Based Capture of Tumor Cells as a New Technology in Peritoneal Metastasis. *J Natl Cancer Inst* **107**, djv184 (2015).

74. F. P. Seib, J. E. Berry, Y. Shiozawa, R. S. Taichman, D. L. Kaplan, Tissue engineering a surrogate niche for metastatic cancer cells. *Biomaterials* **51**, 313-319 (2015).

75. B. A. Aguado, G. G. Bushnell, S. S. Rao, J. S. Jeruss, L. D. Shea, Engineering the pre-metastatic niche. *Nat. Biomed. Eng* **1**, 12 (2017).

76. K. L. Sodek, T. J. Brown, M. J. Ringuette, Collagen I but not Matrigel matrices provide an MMP-dependent barrier to ovarian cancer cell penetration. *BMC Cancer* **8**, 223 (2008).

77. P. M. Davidson, C. Denais, M. C. Bakshi, J. Lammerding, Nuclear Deformability Constitutes a Rate-Limiting Step During Cell Migration in 3-D Environments. *Cell. Mol. Bioeng.* **7**, 293-306 (2014).

78. N. Yao, Y.-J. Jan, S. Cheng, J.-F. Chen, L. W. Chung, H.-R. Tseng, E. M. Posadas, Structure and function analysis in circulating tumor cells: using nanotechnology to study nuclear size in prostate cancer. *American journal of clinical and experimental urology* **6**, 43-54 (2018).

79. J.-F. Chen, H. Ho, J. Lichterman, Y.-T. Lu, Y. Zhang, M. A. Garcia, S.-F. Chen, A.-J. Liang, E. Hodara, H. E. Zhau, S. Hou, R. S. Ahmed, D. J. Luthringer, J. Huang, K.-C. Li, L. W. K. Chung, Z. Ke, H.-R. Tseng, E. M. Posadas, Subclassification of prostate cancer circulating tumor cells by nuclear size reveals very small nuclear circulating tumor cells in patients with visceral metastases. *Cancer* **121**, 3240-3251 (2015).

80. C. Alibert, B. Goud, J. B. Manneville, Are cancer cells really softer than normal cells? *Biol. Cell* **109**, 167-189 (2017).

81. Q. Guo, S. Park, H. S. Ma, Microfluidic micropipette aspiration for measuring the deformability of single cells. *Lab Chip* **12**, 2687-2695 (2012).

82. M. Mak, D. Erickson, A serial micropipette microfluidic device with applications to cancer cell repeated deformation studies. *Integr. Biol.* **5**, 1374-1384 (2013).

83. M. Malboubi, A. Jayo, M. Parsons, G. Charras, An open access microfiuidic device for the study of the physical limits of cancer cell deformation during migration in confined environments. *Microelectron. Eng.* **144**, 42-45 (2015).

84. D. R. Gossett, H. T. K. Tse, S. A. Lee, Y. Ying, A. G. Lindgren, O. O. Yang, J. Y. Rao, A. T. Clark, D. Di Carlo, Hydrodynamic stretching of single cells for large population mechanical phenotyping. *Proc. Natl. Acad. Sci. U. S. A.* **109**, 7630-7635 (2012).

85. J. S. Dudani, D. R. Gossett, H. T. K. Tse, D. Di Carlo, Pinched-flow hydrodynamic stretching of single-cells. *Lab Chip* **13**, 3728-3734 (2013).

86. D. P. Qi, N. K. Gill, C. Santiskulvong, J. Sifuentes, O. Dorigo, J. Y. Rao, B. Taylor-Harding, W. R. Wiedemeyer, A. C. Rowat, Screening cell mechanotype by parallel microfiltration. *Sci Rep* **5**, (2015).

87. K. D. Nyberg, M. B. Scott, S. L. Bruce, A. B. Gopinath, D. Bikos, T. G. Mason, J. W. Kim, H. S. Choi, A. C. Rowat, The physical origins of transit time measurements for rapid, single cell mechanotyping. *Lab Chip* **16**, 3330-3339 (2016).

88. C. P. Palmer, M. E. Mycielska, H. Burcu, K. Osman, T. Collins, R. Beckerman, R. Perrett, H. Johnson, E. Aydar, M. B. A. Djamgoz, Single cell adhesion measuring apparatus (SCAMA): application to cancer cell lines of different metastatic potential and voltage-gated Na+ channel expression. *European Biophysics Journal* **37**, 359-368 (2008).

89. M. Veiseh, D. H. Kwon, A. D. Borowsky, C. Tolg, H. S. Leong, J. D. Lewis, E. A. Turley, M. J. Bissell, Cellular heterogeneity profiling by hyaluronan probes reveals an invasive but slow-growing breast tumor subset. *Proc. Natl. Acad. Sci. U. S. A.* **111**, E1731-E1739 (2014).

90. K. Bijian, C. Lougheed, J. Su, B. Xu, H. Yu, J. H. Wu, K. Riccio, M. A. Alaoui-Jamali, Targeting focal adhesion turnover in invasive breast cancer cells by the purine derivative reversine. *British Journal of Cancer* **109**, 2810-2818 (2013).

91. A. Fuhrmann, A. Banisadr, P. Beri, T. D. Tlsty, A. J. Engler, Metastatic State of Cancer Cells May Be Indicated by Adhesion Strength. *Biophys. J.* **112**, 736-745 (2017).

92. M. H. Seltzer, F. E. Rosato, M. J. Fletcher, SERUM AND TISSUE MAGNESIUM LEVELS IN HUMAN BREAST CARCINOMA. *Journal of Surgical Research* **10**, 159-& (1970).

93. M. H. Seltzer, F. E. Rosato, M. J. Fletcher, SERUM AND TISSUE CALCIUM IN HUMAN BREAST CARCINOMA. *Cancer Res.* **30**, 615-& (1970).

94. Z. X. Zhou, Z. R. Lu, Molecular imaging of the tumor microenvironment. *Adv. Drug Deliv. Rev.* **113**, 24-48 (2017).

95. L. Chaabane, L. Tei, L. Miragoli, L. Lattuada, M. von Wronski, F. Uggeri, V. Lorusso, S. Aime, In Vivo MR Imaging of Fibrin in a Neuroblastoma Tumor Model by Means of a Targeting Gd-Containing Peptide. *Mol. Imaging. Biol.* **17**, 819-828 (2015).

96. L. W. E. Starmans, T. van Mourik, R. Rossin, I. Verel, K. Nicolay, H. Grull, Noninvasive Visualization of Tumoral Fibrin Deposition Using a Peptidic Fibrin-Binding Single Photon Emission Computed Tomography Tracer. *Mol. Pharm.* **12**, 1921-1928 (2015).

97. T. Obonai, H. Fuchigami, F. Furuya, N. Kozuka, M. Yasunaga, Y. Matsumura, Tumour imaging by the detection of fibrin clots in tumour stroma using an anti-fibrin Fab fragment. *Sci Rep* **6**, 10 (2016).

98. T. van Mourik, M. Claesener, K. Nicolay, H. Grüll. (*J Label Compd Radiopharm* . 2017), vol. 60, pp. 286 – 293.

99. Z. X. Zhou, M. Qutaish, Z. Han, R. M. Schur, Y. Q. Liu, D. L. Wilson, Z. R. Lu, MRI detection of breast cancer micrometastases with a fibronectin-targeting contrast agent. *Nat. Commun.* **6**, 11 (2015).

100. C. L. Li, D. Yang, X. Cao, F. Wang, D. Y. Hong, J. Wang, X. C. Shen, Y. Chen, Fibronectin induces epithelial-mesenchymal transition in human breast cancer MCF-7 cells via activation of calpain. *Oncol. Lett.* **13**, 3889-3895 (2017).

101. Z. Han, Z. R. Lu, Targeting fibronectin for cancer imaging and therapy. *J. Mat. Chem. B* **5**, 639-654 (2017).

102. P. Heidari, S. A. Esfahani, N. S. Turker, G. Wong, T. C. Wang, A. K. Rustgi, U. Mahmood, Imaging of Secreted Extracellular Periostin, an Important Marker of Invasion in the Tumor Microenvironment in Esophageal Cancer. *J. Nucl. Med.* **56**, 1246-1251 (2015).

103. I. A. Khawar, J. H. Kim, H. J. Kuh, Improving drug delivery to solid tumors: Priming the tumor microenvironment. *J. Control. Release* **201**, 78-89 (2015).

104. M. Grossman, N. Ben-Chetrit, A. Zhuravlev, R. Afik, E. Bassat, I. Solomonov, Y. Yarden, I. Sagi, Tumor Cell Invasion Can Be Blocked by Modulators of Collagen Fibril Alignment That Control Assembly of the Extracellular Matrix. *Cancer Res.* **76**, 4249-4258 (2016).

105. A. D. Theocharis, S. S. Skandalis, C. Gialeli, N. K. Karamanos, Extracellular matrix structure. *Adv. Drug Deliv. Rev.* **97**, 4-27 (2016).

106. Paolo P. Provenzano, C. Cuevas, Amy E. Chang, Vikas K. Goel, Daniel D. Von Hoff, Sunil R. Hingorani, Enzymatic Targeting of the Stroma Ablates Physical Barriers to Treatment of Pancreatic Ductal Adenocarcinoma. *Cancer Cell* **21**, 418-429 (2012).

107. M. A. Jacobetz, D. S. Chan, A. Neesse, T. E. Bapiro, N. Cook, K. K. Frese, C. Feig, T. Nakagawa, M. E. Caldwell, H. I. Zecchini, M. P. Lolkema, P. Jiang, A. Kultti, C. B. Thompson, D. C. Maneval, D. I. Jodrell, G. I. Frost, H. M. Shepard, J. N. Skepper, D. A. Tuveson, Hyaluronan impairs vascular function and drug delivery in a mouse model of pancreatic cancer. *Gut* **62**, 112 (2013).

108. S. R. Hingorani, W. P. Harris, J. T. Beck, B. A. Berdov, S. A. Wagner, E. M. Pshevlotsky, S. A. Tjulandin, O. A. Gladkov, R. F. Holcombe, R. Korn, N. Raghunand, S. Dychter, P. Jiang, H. M. Shepard, C. E. Devoe, Phase Ib Study of PEGylated Recombinant Human Hyaluronidase and Gemcitabine in Patients with Advanced Pancreatic Cancer. *Clinical Cancer Research* **22**, 2848 (2016).

109. S. Lee, H. Han, H. Koo, J. H. Na, H. Y. Yoon, K. E. Lee, H. Lee, H. Kim, I. C. Kwon, K. Kim, Extracellular matrix remodeling in vivo for enhancing tumor-

targeting efficiency of nanoparticle drug carriers using the pulsed high intensity focused ultrasound. *J. Control. Release* **263**, 68-78 (2017).

110. G. Baronzio, G. Parmar, M. Baronzio, Overview of Methods for Overcoming Hindrance to Drug Delivery to Tumors, with Special Attention to Tumor Interstitial Fluid. *Front. Oncol.* **5**, 165 (2015).

111. J. Y. Yhee, S. Jeon, H. Y. Yoon, M. K. Shim, H. Ko, J. Min, J. H. Na, H. Chang, H. Han, J. H. Kim, M. Suh, H. Lee, J. H. Park, K. Kim, I. C. Kwon, Effects of tumor microenvironments on targeted delivery of glycol chitosan nanoparticles. *J. Control. Release* **267**, 223-231 (2017).

112. A. Nicolas-Boluda, A. K. A. Silva, S. Fournel, F. Gazeau, Physical oncology: New targets for nanomedicine. *Biomaterials* **150**, 87-99 (2018).

113. I. Marangon, A. A. K. Silva, T. Guilbert, J. Kolosnjaj-Tabi, C. Marchiol, S. Natkhunarajah, F. Chamming's, C. Menard-Moyon, A. Bianco, J. L. Gennisson, G. Renault, F. Gazeau, Tumor Stiffening, a Key Determinant of Tumor Progression, is Reversed by Nanomaterial-Induced Photothermal Therapy. *Theranostics* **7**, 329-343 (2017).

114. V. Raeesi, W. C. W. Chan, Improving nanoparticle diffusion through tumor collagen matrix by photo-thermal gold nanorods. *Nanoscale* **8**, 12524-12530 (2016).

115. J. C. L. Schuh, Trials, Tribulations, and Trends in Tumor Modeling in Mice. *Toxicologic Pathology* **32**, 53-66 (2004).

116. C.-P. Day, G. Merlino, T. Van Dyke, Preclinical Mouse Cancer Models: A Maze of Opportunities and Challenges. *Cell* **163**, 39-53 (2015).

117. E. Quintana, M. Shackleton, M. S. Sabel, D. R. Fullen, T. M. Johnson, S. J. Morrison, Efficient tumour formation by single human melanoma cells. *Nature* **456**, 593 (2008).

118. D. Wirtz, K. Konstantopoulos, P. C. Searson, The physics of cancer: the role of physical interactions and mechanical forces in metastasis. *Nat. Rev. Cancer* **11**, 512-522 (2011).

119. M. H. Zaman, L. M. Trapani, A. L. Sieminski, D. MacKellar, H. Gong, R. D. Kamm, A. Wells, D. A. Lauffenburger, P. Matsudaira, Migration of tumor cells in 3D matrices is governed by matrix stiffness along with cell-matrix adhesion and

proteolysis. *Proceedings of the National Academy of Sciences* **103**, 10889-10894 (2006).

120. A. J. Ridley, M. A. Schwartz, K. Burridge, R. A. Firtel, M. H. Ginsberg, G. Borisy, J. T. Parsons, A. R. Horwitz, Cell Migration: Integrating Signals from Front to Back. *Science* **302**, 1704 (2003).

121. I. Indra, V. Undyala, C. Kandow, U. Thirumurthi, M. Dembo, K. A. Beningo, An in vitro correlation of mechanical forces and metastatic capacity. *Physical Biology* **8**, (2011).

122. Y. Liu, R. Nenutil, M. V. Appleyard, K. Murray, M. Boylan, A. M. Thompson, P. J. Coates, Lack of correlation of stem cell markers in breast cancer stem cells. *British Journal Of Cancer* **110**, 2063 (2014).

123. D. Boettiger, Quantitative measurements of integrin-mediated adhesion to extracellular matrix. *Integrins* **426**, 1-+ (2007).

124. A. Fuhrmann, J. Li, S. Chien, A. J. Engler, Cation Type Specific Cell Remodeling Regulates Attachment Strength. *PLOS ONE* **9**, e102424 (2014).

125. N. D. Gallant, A. J. García, Model of integrin-mediated cell adhesion strengthening. *Journal of Biomechanics* **40**, 1301-1309 (2007).

126. C. M. Yates, H. M. McGettrick, G. B. Nash, G. E. Rainger, in *Metastasis Research Protocols,* M. Dwek, U. Schumacher, S. A. Brooks, Eds. (Springer New York, New York, NY, 2014), pp. 57-75.

127. E. G. Fischer, M. Riewald, H. Y. Huang, Y. Miyagi, Y. Kubota, B. M. Mueller, W. Ruf, Tumor cell adhesion and migration supported by interaction of a receptor-protease complex with its inhibitor. *The Journal of clinical investigation* **104**, 1213-1221 (1999).

128. Piyush B. Gupta, Christine M. Fillmore, G. Jiang, Sagi D. Shapira, K. Tao, C. Kuperwasser, Eric S. Lander, Stochastic State Transitions Give Rise to Phenotypic Equilibrium in Populations of Cancer Cells. *Cell* **146**, 633-644 (2011).

129. A. Nasulewicz, J. Wietrzyk, F. I. Wolf, S. Dzimira, J. Madej, J. A. M. Maier, Y. Rayssiguier, A. Mazur, A. Opolski, Magnesium deficiency inhibits primary tumor growth but favors metastasis in mice. *Biochimica et Biophysica Acta (BBA) - Molecular Basis of Disease* **1739**, 26-32 (2004).

130. Q. Dai, S. S. Motley, J. A. Smith, Jr., R. Concepcion, D. Barocas, S. Byerly, J. H. Fowke, Blood Magnesium, and the Interaction with Calcium, on the Risk of High-Grade Prostate Cancer. *PLOS ONE* **6**, e18237 (2011).

131. A. P. Mould, S. K. Akiyama, M. J. Humphries, Regulation of Integrin α5β1-Fibronectin Interactions by Divalent Cations: EVIDENCE FOR DISTINCT CLASSES OF BINDING SITES FOR Mn2+, Mg2+, AND Ca2+. **270**, 26270-26277 (1995).

132. B. Geiger, J. P. Spatz, A. D. Bershadsky, Environmental sensing through focal adhesions. *Nature Reviews Molecular Cell Biology* **10**, 21-33 (2009).

133. J. T. Parsons, A. R. Horwitz, M. A. Schwartz, Cell adhesion: integrating cytoskeletal dynamics and cellular tension. *Nature Reviews Molecular Cell Biology* **11**, 633-643 (2010).

134. H. G. H., W. S. R., MCF-10AT: A Model for Human Breast Cancer Development. *The Breast Journal* **5**, 122-129 (1999).

135. A. Fuhrmann, A. J. Engler, Acute shear stress direction dictates adherent cell remodeling and verifies shear profile of spinning disk assays. *Physical Biology* **12**, 016011 (2015).

136. L. J. van 't Veer, H. Dai, M. J. van de Vijver, Y. D. He, A. A. M. Hart, M. Mao, H. L. Peterse, K. van der Kooy, M. J. Marton, A. T. Witteveen, G. J. Schreiber, R. M. Kerkhoven, C. Roberts, P. S. Linsley, R. Bernards, S. H. Friend, Gene expression profiling predicts clinical outcome of breast cancer. *Nature* **415**, 530-536 (2002).

137. S. Paik, S. Shak, G. Tang, C. Kim, J. Baker, M. Cronin, F. L. Baehner, M. G. Walker, D. Watson, T. Park, W. Hiller, E. R. Fisher, D. L. Wickerham, J. Bryant, N. Wolmark, A Multigene Assay to Predict Recurrence of Tamoxifen-Treated, Node-Negative Breast Cancer. *New England Journal of Medicine* **351**, 2817-2826 (2004).

138. D. S. Subramaniam, C. Isaacs, Utilizing prognostic and predictive factors in breast cancer. *Current Treatment Options in Oncology* **6**, 147-159 (2005).

139. S. Valastyan, Robert A. Weinberg, Tumor Metastasis: Molecular Insights and Evolving Paradigms. *Cell* **147**, 275-292 (2011).

140. S. I. Fraley, Y. Feng, R. Krishnamurthy, D.-H. Kim, A. Celedon, G. D. Longmore, D. Wirtz, A distinctive role for focal adhesion proteins in three-dimensional cell motility. *Nat. Cell Biol.* **12**, 598-604 (2010).

141. Y. Mao, J. E. Schwarzbauer, Stimulatory effects of a three-dimensional microenvironment on cell-mediated fibronectin fibrillogenesis. *Journal of Cell Science* **118**, 4427-4436 (2005).

142. J. Huth, M. Buchholz, J. M. Kraus, K. Mølhave, C. Gradinaru, G. v. Wichert, T. M. Gress, H. Neumann, H. A. Kestler, TimeLapseAnalyzer: Multi-target analysis for live-cell imaging and time-lapse microscopy. *Computer Methods and Programs in Biomedicine* **104**, 227-234 (2011).

143. P. S. Steeg, Targeting metastasis. *Nat. Rev. Cancer* **16**, 201-218 (2016).

144. S. R. L., M. K. D., J. Ahmedin, Cancer statistics, 2018. *CA: A Cancer Journal for Clinicians* **68**, 7-30 (2018).

145. K. Polyak, Heterogeneity in breast cancer. *The Journal of Clinical Investigation* **121**, 3786-3788 (2011).

146. X.-x. Sun, Q. Yu, Intra-tumor heterogeneity of cancer cells and its implications for cancer treatment. *Acta Pharmacologica Sinica* **36**, 1219 (2015).

147. P. Beri, B. F. Matte, L. Fattet, D. Kim, J. Yang, A. J. Engler, Biomaterials to model and measure epithelial cancers. *Nature Reviews Materials*, (2018).

148. P. DiMilla, J. Stone, J. Quinn, S. Albelda, D. Lauffenburger, Maximal migration of human smooth muscle cells on fibronectin and type IV collagen occurs at an intermediate attachment strength. *The Journal of Cell Biology* **122**, 729-737 (1993).

149. A. J. Garcia, N. D. Gallant, Stick and grip. *Cell Biochemistry and Biophysics* **39**, 61-73 (2003).

150. M. Veiseh, D. H. Kwon, A. D. Borowsky, C. Tolg, H. S. Leong, J. D. Lewis, E. A. Turley, M. J. Bissell, Cellular heterogeneity profiling by hyaluronan probes reveals an invasive but slow-growing breast tumor subset. *Proceedings of the National Academy of Sciences* **111**, E1731-E1739 (2014).

151. M. H. Seltzer, F. E. Rosato, M. J. Fletcher, Serum and tissue magnesium levels in human breast carcinoma. *J Surg Res* **10**, 159-162 (1970).

152. M. H. Seltzer, F. E. Rosato, M. J. Fletcher, Serum and tissue calcium in human breast carcinoma. *Cancer Res* **30**, 615-616 (1970).

153. C. T. Mierke, P. Kollmannsberger, D. P. Zitterbart, G. Diez, T. M. Koch, S. Marg, W. H. Ziegler, W. H. Goldmann, B. Fabry, Vinculin facilitates cell invasion into three-dimensional collagen matrices. *The Journal of biological chemistry* **285**, 13121-13130 (2010).

154. M. J. Stroud, R. A. Kammerer, C. Ballestrem, Characterization of G2L3 (GAS2-like 3), a new microtubule- and actin-binding protein related to spectraplakins. *The Journal of biological chemistry* **286**, 24987-24995 (2011).

155. P. Friedl, K. Wolf, J. Lammerding, Nuclear mechanics during cell migration. *Current Opinion in Cell Biology* **23**, 55-64 (2011).

156. A. Jayo, M. Malboubi, S. Antoku, W. Chang, E. Ortiz-Zapater, C. Groen, K. Pfisterer, T. Tootle, G. Charras, Gregg G. Gundersen, M. Parsons, Fascin Regulates Nuclear Movement and Deformation in Migrating Cells. *Developmental Cell* **38**, 371-383 (2016).

157. N. Kumar, S. Gupta, S. Dabral, S. Singh, S. Sehrawat, Role of exchange protein directly activated by cAMP (EPAC1) in breast cancer cell migration and apoptosis. *Molecular and Cellular Biochemistry* **430**, 115-125 (2017).

158. M.-H. Yang, Z.-Y. Hu, C. Xu, L.-Y. Xie, X.-Y. Wang, S.-Y. Chen, Z.-G. Li, MALAT1 promotes colorectal cancer cell proliferation/migration/invasion via PRKA kinase anchor protein 9. *Biochimica et Biophysica Acta (BBA) - Molecular Basis of Disease* **1852**, 166-174 (2015).

159. S. M. Ahmed, B. L. Thériault, M. Uppalapati, C. W. N. Chiu, B. L. Gallie, S. S. Sidhu, S. Angers, KIF14 negatively regulates Rap1a–Radil signaling during breast cancer progression. *The Journal of Cell Biology* **199**, 951-967 (2012).

160. B. L. Thériault, H. D. Basavarajappa, H. Lim, S. Pajovic, B. L. Gallie, T. W. Corson, Transcriptional and Epigenetic Regulation of KIF14 Overexpression in Ovarian Cancer. *PLOS ONE* **9**, e91540 (2014).

161. L. Mi, F. Zhu, X. Yang, J. Lu, Y. Zheng, Q. Zhao, X. Wen, A. Lu, M. Wang, M. Zheng, J. Ji, J. Sun, The metastatic suppressor NDRG1 inhibits EMT, migration and invasion through interaction and promotion of caveolin-1 ubiquitylation in human colorectal cancer cells. *Oncogene* **36**, 4323 (2017).

162. J. Hu, A. S. Verkman, Increased migration and metastatic potential of tumor cells expressing aquaporin water channels. *The FASEB Journal* **20**, 1892-1894 (2006).

163. J. K. Slack, R. B. Adams, J. D. Rovin, E. A. Bissonette, C. E. Stoker, J. T. Parsons, Alterations in the focal adhesion kinase/Src signal transduction pathway correlate with increased migratory capacity of prostate carcinoma cells. *Oncogene* **20**, 1152 (2001).

164. M. C. Frame, V. J. Fincham, N. O. Carragher, J. A. Wyke, v-SRC'S hold over actin and cell adhesions. *Nature Reviews Molecular Cell Biology* **3**, 233 (2002).

165. G. W. McLean, N. O. Carragher, E. Avizienyte, J. Evans, V. G. Brunton, M. C. Frame, The role of focal-adhesion kinase in cancer — a new therapeutic opportunity. *Nat. Rev. Cancer* **5**, 505 (2005).

166. R. Feng, S. Li, C. Lu, C. Andreas, D. B. Stolz, M. Y. Mapara, S. Lentzsch, Targeting the Microtubular Network as a New Antimyeloma Strategy. *Molecular Cancer Therapeutics* **10**, 1886-1896 (2011).

167. V. Lo Sardo, P. Chubukov, W. Ferguson, A. Kumar, E. L. Teng, M. Duran, L. Zhang, G. Cost, A. J. Engler, F. Urnov, E. J. Topol, A. Torkamani, K. K. Baldwin, Unveiling the Role of the Most Impactful Cardiovascular Risk Locus through Haplotype Editing. *Cell* **175**, 1796-1810.e1720 (2018).

168. A. Kumar, S. K. Thomas, K. C. Wong, V. Lo Sardo, D. S. Cheah, Y.-H. Hou, J. K. Placone, K. P. Tenerelli, W. C. Ferguson, A. Torkamani, E. J. Topol, K. K. Baldwin, A. J. Engler, Mechanical activation of noncoding-RNA-mediated regulation of disease-associated phenotypes in human cardiomyocytes. *Nat. Biomed. Eng* **3**, 137-146 (2019).

169. M. Martin, Cutadapt removes adapter sequences from high-throughput sequencing reads. *2011* **17**, 3 (2011).

170. S. Andrews. (2010). FAST QC: A quality control tool for high throughput sequence data. http://www.bioinformatics.babraham.ac.uk/projects/fastqc/.

171. A. Dobin, C. A. Davis, F. Schlesinger, J. Drenkow, C. Zaleski, S. Jha, P. Batut, M. Chaisson, T. R. Gingeras, STAR: ultrafast universal RNA-seq aligner. *Bioinformatics* **29**, 15-21 (2012).

172. S. Anders, P. T. Pyl, W. Huber, HTSeq—a Python framework to work with high-throughput sequencing data. *Bioinformatics* **31**, 166-169 (2014).

173. M. I. Love, W. Huber, S. Anders, Moderated estimation of fold change and dispersion for RNA-seq data with DESeq2. *Genome Biology* **15**, 550 (2014).

174. L. Wang, S. Wang, W. Li, RSeQC: quality control of RNA-seq experiments. *Bioinformatics* **28**, 2184-2185 (2012).

175. C. Hennig. Cran package fpc. http://cran.r-project.org/web/packages/fpc/

176. S. Heinz, C. Benner, N. Spann, E. Bertolino, Y. C. Lin, P. Laslo, J. X. Cheng, C. Murre, H. Singh, C. K. Glass, Simple Combinations of Lineage-Determining Transcription Factors Prime cis-Regulatory Elements Required for Macrophage and B Cell Identities. *Molecular Cell* **38**, 576-589 (2010).

177. J. Liu, T. Lichtenberg, K. A. Hoadley, L. M. Poisson, A. J. Lazar, A. D. Cherniack, A. J. Kovatich, C. C. Benz, D. A. Levine, A. V. Lee, L. Omberg, D. M. Wolf, C. D. Shriver, V. Thorsson, S. J. Caesar-Johnson, J. A. Demchok, I. Felau, M. Kasapi, M. L. Ferguson, C. M. Hutter, H. J. Sofia, R. Tarnuzzer, Z. Wang, L. Yang, J. C. Zenklusen, J. Zhang, S. Chudamani, J. Liu, L. Lolla, R. Naresh, T. Pihl, Q. Sun, Y. Wan, Y. Wu, J. Cho, T. DeFreitas, S. Frazer, N. Gehlenborg, G. Getz, D. I. Heiman, J. Kim, M. S. Lawrence, P. Lin, S. Meier, M. S. Noble, G. Saksena, D. Voet, H. Zhang, B. Bernard, N. Chambwe, V. Dhankani, T. Knijnenburg, R. Kramer, K. Leinonen, Y. Liu, M. Miller, S. Reynolds, I. Shmulevich, W. Zhang, R. Akbani, B. M. Broom, A. M. Hegde, Z. Ju, R. S. Kanchi, A. Korkut, J. Li, H. Liang, S. Ling, W. Liu, Y. Lu, G. B. Mills, K.-S. Ng, A. Rao, M. Ryan, J. Wang, J. N. Weinstein, J. Zhang, A. Abeshouse, J. Armenia, D. Chakravarty, W. K. Chatila, I. de Bruijn, J. Gao, B. E. Gross, Z. J. Heins, R. Kundra, K. La, M. Ladanyi, A. Luna, M. G. Nissan, A. Ochoa, S. M. Phillips, E. Reznik, F. Sanchez-Vega, C. Sander, N. Schultz, R. Sheridan, S. O. Sumer, Y. Sun, B. S. Taylor, J. Wang, H. Zhang, P. Anur, M. Peto, P. Spellman, C. Benz, J. M. Stuart, C. K. Wong, C. Yau, D. N. Hayes, J. S. Parker, M. D. Wilkerson, A. Ally, M. Balasundaram, R. Bowlby, D. Brooks, R. Carlsen, E. Chuah, N. Dhalla, R. Holt, S. J. M. Jones, K. Kasaian, D. Lee, Y. Ma, M. A. Marra, M. Mayo, R. A. Moore, A. J. Mungall, K. Mungall, A. G. Robertson, S. Sadeghi, J. E. Schein, P. Sipahimalani, A. Tam, N. Thiessen, K. Tse, T. Wong, A. C. Berger, R. Beroukhim, C. Cibulskis, S. B. Gabriel, G. F. Gao, G. Ha, M. Meyerson, S. E. Schumacher, J. Shih, M. H. Kucherlapati, R. S. Kucherlapati, S. Baylin, L. Cope, L. Danilova, M. S. Bootwalla, P. H. Lai, D. T. Maglinte, D. J. Van Den Berg, D. J. Weisenberger, J. T. Auman, S. Balu, T. Bodenheimer, C. Fan, A. P. Hoyle, S. R. Jefferys, C. D. Jones, S. Meng, P. A. Mieczkowski, L. E. Mose, A. H. Perou, C. M. Perou, J. Roach, Y. Shi, J. V. Simons, T. Skelly, M. G. Soloway, D. Tan, U. Veluvolu, H. Fan, T. Hinoue, P. W. Laird, H. Shen, W. Zhou, M. Bellair, K. Chang, K. Covington, C. J. Creighton, H. Dinh, H. Doddapaneni, L. A. Donehower, J. Drummond, R. A. Gibbs, R. Glenn, W. Hale, Y. Han, J. Hu, V. Korchina, S. Lee, L. Lewis, W. Li, X. Liu, M. Morgan, D. Morton, D. Muzny, J. Santibanez, M. Sheth, E. Shinbro, L. Wang, M. Wang, D. A. Wheeler, L. Xi, F. Zhao, J. Hess, E. L. Appelbaum, M. Bailey, M. G. Cordes, L. Ding, C. C. Fronick, L. A. Fulton, R. S. Fulton, C. Kandoth, E. R. Mardis, M. D. McLellan, C. A. Miller, H. K. Schmidt, R. K. Wilson, D. Crain, E. Curley, J. Gardner, K. Lau, D. Mallery, S. Morris, J. Paulauskis, R. Penny, C. Shelton, T. Shelton, M. Sherman,

E. Thompson, P. Yena, J. Bowen, J. M. Gastier-Foster, M. Gerken, K. M. Leraas, T. M. Lichtenberg, N. C. Ramirez, L. Wise, E. Zmuda, N. Corcoran, T. Costello, C. Hovens, A. L. Carvalho, A. C. de Carvalho, J. H. Fregnani, A. Longatto-Filho, R. M. Reis, C. Scapulatempo-Neto, H. C. S. Silveira, D. O. Vidal, A. Burnette, J. Eschbacher, B. Hermes, A. Noss, R. Singh, M. L. Anderson, P. D. Castro, M. Ittmann, D. Huntsman, B. Kohl, X. Le, R. Thorp, C. Andry, E. R. Duffy, V. Lyadov, O. Paklina, G. Setdikova, A. Shabunin, M. Tavobilov, C. McPherson, R. Warnick, R. Berkowitz, D. Cramer, C. Feltmate, N. Horowitz, A. Kibel, M. Muto, C. P. Raut, A. Malykh, J. S. Barnholtz-Sloan, W. Barrett, K. Devine, J. Fulop, Q. T. Ostrom, K. Shimmel, Y. Wolinsky, A. E. Sloan, A. De Rose, F. Giuliante, M. Goodman, B. Y. Karlan, C. H. Hagedorn, J. Eckman, J. Harr, J. Myers, K. Tucker, L. A. Zach, B. Deyarmin, H. Hu, L. Kvecher, C. Larson, R. J. Mural, S. Somiari, A. Vicha, T. Zelinka, J. Bennett, M. Iacocca, B. Rabeno, P. Swanson, M. Latour, L. Lacombe, B. Têtu, A. Bergeron, M. McGraw, S. M. Staugaitis, J. Chabot, H. Hibshoosh, A. Sepulveda, T. Su, T. Wang, O. Potapova, O. Voronina, L. Desjardins, O. Mariani, S. Roman-Roman, X. Sastre, M.-H. Stern, F. Cheng, S. Signoretti, A. Berchuck, D. Bigner, E. Lipp, J. Marks, S. McCall, R. McLendon, A. Secord, A. Sharp, M. Behera, D. J. Brat, A. Chen, K. Delman, S. Force, F. Khuri, K. Magliocca, S. Maithel, J. J. Olson, T. Owonikoko, A. Pickens, S. Ramalingam, D. M. Shin, G. Sica, E. G. Van Meir, H. Zhang, W. Eijckenboom, A. Gillis, E. Korpershoek, L. Looijenga, W. Oosterhuis, H. Stoop, K. E. van Kessel, E. C. Zwarthoff, C. Calatozzolo, L. Cuppini, S. Cuzzubbo, F. DiMeco, G. Finocchiaro, L. Mattei, A. Perin, B. Pollo, C. Chen, J. Houck, P. Lohavanichbutr, A. Hartmann, C. Stoehr, R. Stoehr, H. Taubert, S. Wach, B. Wullich, W. Kycler, D. Murawa, M. Wiznerowicz, K. Chung, W. J. Edenfield, J. Martin, E. Baudin, G. Bubley, R. Bueno, A. De Rienzo, W. G. Richards, S. Kalkanis, T. Mikkelsen, H. Noushmehr, L. Scarpace, N. Girard, M. Aymerich, E. Campo, E. Giné, A. L. Guillermo, N. Van Bang, P. T. Hanh, B. D. Phu, Y. Tang, H. Colman, K. Evason, P. R. Dottino, J. A. Martignetti, H. Gabra, H. Juhl, T. Akeredolu, S. Stepa, D. Hoon, K. Ahn, K. J. Kang, F. Beuschlein, A. Breggia, M. Birrer, D. Bell, M. Borad, A. H. Bryce, E. Castle, V. Chandan, J. Cheville, J. A. Copland, M. Farnell, T. Flotte, N. Giama, T. Ho, M. Kendrick, J.-P. Kocher, K. Kopp, C. Moser, D. Nagorney, D. O'Brien, B. P. O'Neill, T. Patel, G. Petersen, F. Que, M. Rivera, L. Roberts, R. Smallridge, T. Smyrk, M. Stanton, R. H. Thompson, M. Torbenson, J. D. Yang, L. Zhang, F. Brimo, J. A. Ajani, A. M. Angulo Gonzalez, C. Behrens, J. Bondaruk, R. Broaddus, B. Czerniak, B. Esmaeli, J. Fujimoto, J. Gershenwald, C. Guo, C. Logothetis, F. Meric-Bernstam, C. Moran, L. Ramondetta, D. Rice, A. Sood, P. Tamboli, T. Thompson, P. Troncoso, A. Tsao, I. Wistuba, C. Carter, L. Haydu, P. Hersey, V. Jakrot, H. Kakavand, R. Kefford, K. Lee, G. Long, G. Mann, M. Quinn, R. Saw, R. Scolyer, K. Shannon, A. Spillane, J. Stretch, M. Synott, J. Thompson, J. Wilmott, H. Al-Ahmadie, T. A. Chan, R. Ghossein, A. Gopalan, V. Reuter, S. Singer, B. Singh, N. V. Tien, T. Broudy, C. Mirsaidi, P. Nair, P. Drwiega, J. Miller, J. Smith, H. Zaren, J.-W. Park, N. P. Hung, E. Kebebew, W. M. Linehan, A. R. Metwalli, K. Pacak, P. A. Pinto, M. Schiffman, L. S. Schmidt, C. D. Vocke, N. Wentzensen, R. Worrell, H. Yang, M. Moncrieff, C. Goparaju, J. Melamed, H. Pass, N. Botnariuc, I. Caraman, M. Cernat, I. Chemencedji, A. Clipca, S. Doruc, G. Gorincioi, S. Mura,

M. Pirtac, I. Stancul, D. Tcaciuc, M. Albert, I. Alexopoulou, A. Arnaout, J. Bartlett, J. Engel, S. Gilbert, J. Parfitt, H. Sekhon, G. Thomas, D. M. Rassl, R. C. Rintoul, C. Bifulco, R. Tamakawa, W. Urba, N. Hayward, H. Timmers, A. Antenucci, F. Facciolo, G. Grazi, M. Marino, R. Merola, R. de Krijger, A.-P. Gimenez-Roqueplo, A. Piché, S. Chevalier, G. McKercher, K. Birsoy, G. Barnett, C. Brewer, C. Farver, T. Naska, N. A. Pennell, D. Raymond, C. Schilero, K. Smolenski, F. Williams, C. Morrison, J. A. Borgia, M. J. Liptay, M. Pool, C. W. Seder, K. Junker, M. Dinkin, G. Manikhas, D. Alvaro, M. C. Bragazzi, V. Cardinale, G. Carpino, E. Gaudio, D. Chesla, S. Cottingham, M. Dubina, F. Moiseenko, R. Dhanasekaran, K.-F. Becker, K.-P. Janssen, J. Slotta-Huspenina, M. H. Abdel-Rahman, D. Aziz, S. Bell, C. M. Cebulla, A. Davis, R. Duell, J. B. Elder, J. Hilty, B. Kumar, J. Lang, N. L. Lehman, R. Mandt, P. Nguyen, R. Pilarski, K. Rai, L. Schoenfield, K. Senecal, P. Wakely, P. Hansen, R. Lechan, J. Powers, A. Tischler, W. E. Grizzle, K. C. Sexton, A. Kastl, J. Henderson, S. Porten, J. Waldmann, M. Fassnacht, S. L. Asa, D. Schadendorf, M. Couce, M. Graefen, H. Huland, G. Sauter, T. Schlomm, R. Simon, P. Tennstedt, O. Olabode, M. Nelson, O. Bathe, P. R. Carroll, J. M. Chan, P. Disaia, P. Glenn, R. K. Kelley, C. N. Landen, J. Phillips, M. Prados, J. Simko, K. Smith-McCune, S. VandenBerg, K. Roggin, A. Fehrenbach, A. Kendler, S. Sifri, R. Steele, A. Jimeno, F. Carey, I. Forgie, M. Mannelli, M. Carney, B. Hernandez, B. Campos, C. Herold-Mende, C. Jungk, A. Unterberg, A. von Deimling, A. Bossler, J. Galbraith, L. Jacobus, M. Knudson, T. Knutson, D. Ma, M. Milhem, R. Sigmund, A. K. Godwin, R. Madan, H. G. Rosenthal, C. Adebamowo, S. N. Adebamowo, A. Boussioutas, D. Beer, T. Giordano, A.-M. Mes-Masson, F. Saad, T. Bocklage, L. Landrum, R. Mannel, K. Moore, K. Moxley, R. Postier, J. Walker, R. Zuna, M. Feldman, F. Valdivieso, R. Dhir, J. Luketich, E. M. Mora Pinero, M. Quintero-Aguilo, J. C. G. Carlotti, J. S. Dos Santos, R. Kemp, A. Sankarankuty, D. Tirapelli, J. Catto, K. Agnew, E. Swisher, J. Creaney, B. Robinson, C. S. Shelley, E. M. Godwin, S. Kendall, C. Shipman, C. Bradford, T. Carey, A. Haddad, J. Moyer, L. Peterson, M. Prince, L. Rozek, G. Wolf, R. Bowman, K. M. Fong, I. Yang, R. Korst, W. K. Rathmell, J. L. Fantacone-Campbell, J. A. Hooke, J. DiPersio, B. Drake, R. Govindan, S. Heath, T. Ley, B. Van Tine, P. Westervelt, M. A. Rubin, J. I. Lee, N. D. Aredes, A. Mariamidze, An Integrated TCGA Pan-Cancer Clinical Data Resource to Drive High-Quality Survival Outcome Analytics. *Cell* **173**, 400-416.e411 (2018).

178. A. C. Society, Cancer Facts & Figures 2020. **2020**, (2020).

179. P. Beri, A. Popravko, B. Yeoman, A. Kumar, K. Chen, E. Hodzic, A. Chiang, A. Banisadr, J. K. Placone, H. Carter, S. I. Fraley, P. Katira, A. J. Engler, Cell Adhesiveness Serves as a Biophysical Marker for Metastatic Potential. *Cancer Res.* **80**, 901-911 (2020).

180. Y. S. DeRose, K. M. Gligorich, G. Wang, A. Georgelas, P. Bowman, S. J. Courdy, A. L. Welm, B. E. Welm, Patient-Derived Models of Human Breast Cancer:

Protocols for In Vitro and In Vivo Applications in Tumor Biology and Translational Medicine. *Current Protocols in Pharmacology* **60**, 14.23.11-14.23.43 (2013).